Acoustic and elastic FWI of marine dual-sensor streamer data in the presence of salt

Zur Erlangung des akademischen Grades eines

Doktors der Naturwissenschaften (Dr. rer. nat.)

der KIT-Fakultät für Physik des

Karlsruher Instituts für Technologie (KIT)

genehmigte

Dissertation

von

Niklas Thiel, M. Sc.

Abstract

Subsurface areas containing salt bodies proved to be successful sites for hydrocarbon exploration. However, the generation of a subsurface model from seismic data acquired over such regions is extremely challenging due to the complex wavefields. These complex wavefields are produced by interfaces with high-impedance contrasts and strong topography, for example, of salt bodies in sediments. Over the last few years, the application of full-waveform inversion (FWI) has been tested in such regions. This method allows, to obtain highly-detailed information about subsurface parameters. Although the earth is clearly elastic, in the industry FWI is typically used with an acoustic wave equation to reduce the large computational cost. In this work, I apply FWI on a 2D marine streamer field data set using both the elastic and acoustic approaches in order to compare their advantages and disadvantages. The data was acquired by Petroleum Geo-Services (PGS) in deep water offshore Angola, West Africa, where large salt structures are present in the subsurface.

A crucial prerequisite for a successful FWI is the generation of a sufficiently accurate starting model. Usually, the starting model is obtained by means of traveltime tomography and further enhanced by migration velocity analysis. Considerable time and effort are spend on these approaches. In this work, I tested the creation of initial models from field data using solely FWI, without any further tools. Models are constructed by combining a flooding approach, a few iterations of FWI and manual picking of the most important interfaces from shallower to deeper parts of the model. It turned out that this approach works well on synthetic data and, for simple field data. However, for field data sets involving a complex geological setting above the salt some a priori knowledge or additional information has to be incorporated into the workflow in order to resolve the location of the interfaces with sufficient accuracy.

Acoustic FWI, although computationally less expensive than elastic FWI, has one obvious disadvantage: by trying to explain elastic effects in the data which actually cannot be handled using the acoustic wave equation, nonphysical updates and artefacts can be created in the parameter models. Artefacts often cover realistic updates and the clear distinction of both is difficult. For pressure data acquired with a marine streamer geometry, elastic effects have often been considered to be negligible, making the acoustic approach the tool of choice. In this work, I present the impact of the elastic effects on the FWI results for regions with complex salt structures. Here, only the elastic FWI was able to deliver parameter models with detailed structures. These structures could be confirmed by a prestack migration and are consistent with geological interpretations of the region. The structural image of the migration

could even be enhanced. Non-contiguous layers can be identified in the reflectivity model, caused by a lack in the illumination produced by the acquisition geometry. These layers are contiguously visible in the elastic FWI models. The results of the acoustic FWI suffer from significant artefacts, most prominent in the inverted density model. In my inversions, elastic FWI did not only improve the P-wave velocity model but in particular the density model. This makes the density model more reliable and allows its direct use as auxiliary information for a geological interpretation.

Although elastic FWI has a much larger computational overhead compared to the acoustic approach in terms of CPU time and memory requirements, my work revealed that even for a conventional marine 2D streamer pressure data set an elastic approach should be considered, especially in regions with a complex geological subsurface leading to complex wavefields. Consequently, this work implies that there is also great potential in obtaining more detailed information about the subsurface through an elastic FWI reprocessing of legacy data sets, which were only conventionally processed.

Contents

Chapter 1

Introduction

1.1 General overview

At the present time, hydrocarbons are the most used energy source in the world. Energy companies are constantly looking for new oil and gas reservoirs but the discovery of new hydrocarbons becomes increasingly challenging (Leveille et al., 2011). Most of the shallow reservoirs are already in production or exploited. In the past, salt basins proved to be successful sites for the search. The migrated oil and gas is trapped at the bottom of salt layers or at the flanks of salt domes. The Gulf of Mexico (GoM) is probably the most well known site. But also other areas such as offshore Brazil are known as promising sites proved by some significant pre-salt discoveries (Zdraveva et al., 2012). Since offshore Angola and Gabon are geologically very similar, these regions become more and more interesting (Leveille et al., 2011). Brognon and Verrier already reported in 1966 about the oil occurrence in the complex geology offshore Angola, West Africa (Brognon and Verrier, 1966). The field data set used in this work was acquired in this region.

Classical imaging techniques using ray-based imaging methods often have problems picturing salt bodies. The successful imaging heavily depends on a good velocity model. But for salt regions, one of the major challenges is the definition of the salt structure in the velocity model. A well defined salt structure gives a high-quality velocity model resulting in good images. The top of salt (TOS) as strong reflector can usually be imaged fairly well. But if the salt surface is rough, resulting in a complex wavefield, even the TOS cannot be imaged easily. Subsalt regions are particularly challenging (e.g., Ravaut et al., 2008; Etgen et al., 2009). Another reason for the problems is the complex shape of most salt bodies and salt layers. The evaporite was deposited millions of years ago and other sediments deposited on top. The lower density of salt in comparison to the surrounding sediments and the high load allowed the salt to move upwards and form canopies. This often led to a strong topography of the salt structure. In addition to the shape, the allochthonous salt layers often contain trapped sediments and have a rugose surface (Leveille et al., 2011). The intricate shapes and surfaces of salt bodies result in a very complex wave propagation. Regions of poor illumination are often present, especially

below the salt. Additionally, the energy coming up from subsalt regions is weak due to high reflection coefficients at the sediment-salt interface. Most of the energy is reflected at the top-salt surface and only little energy at low impedance contrasts of subsalt structures.

As possible geological misinterpretations of measured geophysical data are very expensive, reliable processing methods must be developed. Standard techniques for velocity model building such as traveltime tomography struggle in salt environments with limited illumination of changing quality. One reason for the poor illumination is that often only narrow-azimuth (NAZ) data are available. In the NAZ acquisition technique, the complex topography is only illuminated from one direction. For smaller salt bodies methods like undershooting and the use of longer offsets and wide-azimuths lead to good results (e.g. Corcoran et al., 2007; Vigh et al., 2011). However, for integrated salt layers even these techniques are not applicable. A promising solution for the problem of imaging the salt and its environment is the application of full-waveform inversion (Tarantola, 1984). Unlike conventional techniques, not only the kinematic information of the events is used, but the entire waveform in phase and amplitude. Synthetic data are modelled by using a starting model of the subsurface beneath the acquisition area. The same acquisition geometry as for the field data is used to allow a direct comparison of the synthetic data and the field data. In order to match the synthetic data to the field data the starting model is updated. After the model update, synthetic data are modelled again using the new model and compared with the field data. Through this process, the model is updated iteratively. By using the full information content of the acquired wavefield FWI can improve the subsurface image considerably and can provide high-resolution velocity and density models. In comparison to the conventional techniques such as Kirchhoff migration, where only a reflectivity model is obtained by using a very smooth velocity model (e.g., obtained by traveltime tomography), the very detailed parameter models produced by FWI can be used for an improvement of the migration image, or they can even be directly used for interpretation (Williamson et al., 2016).

The main disadvantage of FWI is the high computational effort due to the necessary multiple simulations of the full wavefield. Therefore, in this work I was limited to small model spaces as access to large high-performance computers was limited. Over the last years, computers have become more and more powerful and the forward modelling codes more efficient. Therefore, FWI has become also applicable for large-scale models as used in the exploration industry. Successful inversion results including salt bodies in the subsurface were presented using the BP2004 data set or the Chevron 2014 blind test data, both for the synthetic case (e.g., Brenders and Pratt, 2007). But for field data sets some issues remain. For the problem of (sub)salt imaging several different, often very complex workflows were developed (e.g., Lewis et al., 2012; Wang et al., 2015; Esser et al., 2015). Therefore, my goal is to develop a simple workflow using available technologies and techniques. In a first attempt, I focused on acoustic FWI, already available in several companies and applicable for large field data sets. In addition, elastic inversions were performed and will also be presented in the following chapters.

In this work, I present the imaging of a salt structure and its surrounding sediments. Before

starting with the inversion, a sufficiently accurate starting model must be determined, including the salt layer with its complex topography, to avoid cycle skipping during the inversion. The lack of low frequencies is always an issue for FWI. Especially for high-velocity contrasts such as salt bodies in sediment environments, low frequencies are crucial for a successful inversion, but usually not available. With longer offsets the amount of low-frequencies in the data can be increased, but unfortunately also the non-linearities increase (Sirgue, 2006). Therefore, I use a flooding technique similar to the one described in Boonyasiriwat et al. (2010) for the construction of the salt model. It is a multi-stage inversion strategy ideal for models with high parameter contrasts as given in sediments including salt bodies. No prior information about the salt body and no very low frequencies are required. In contrast to the method of Boonyasiriwat et al. (2010), my method needs considerably fewer iterations before picking the top and bottom of salt. In addition, I flood the sediments with a more realistic gradient velocity and not a constant velocity. This supports the FWI process due to a more accurate starting model. The modified flooding technique was tested successfully in the synthetic case in Thiel (2013) and is now applied to field data.

1.2 Previous studies

Due to the increase of computational power available, FWI has become applicable in the last years, not only for synthetic data, but also for acquired field data. Most of these field data applications focus on the acoustic approximation of FWI to invert only P-wave velocity (v_P) due to the computational costs. In order to enhance the FWI results, special acquisition geometries became popular (see figure 1.1). Vigh et al. (2010) showed for example the application of acoustic FWI to a wide-azimuth (WAZ) streamer data set. Recently, Xiao et al. (2016) presented the application of acoustic FWI to a 2D line offshore Gabon and Peng et al. (2018) showed a field data application of acoustic FWI to WAZ and full-azimuth (FAZ) data from the GoM region.
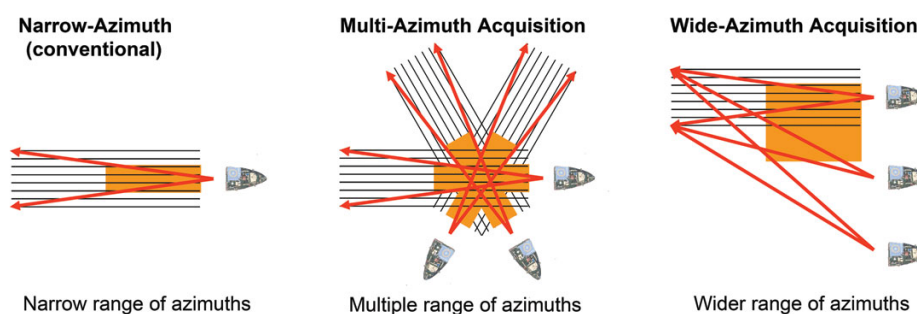
Figure 1.1: Comparison of different streamer acquisition geometries. Source: Rekdal and Long (2006).

Not only streamer data, but also ocean bottom surveys were used to demonstrate the applicability of FWI to field data: Warner et al. (2013) described the application of acoustic FWI to a 3D 4-component ocean-bottom survey data set. Recently, Shen et al. (2018) showed the application of acoustic FWI to a 4D ocean-bottom node (OBN) data set from the GoM

region. Despite available FAZ data, very long offsets of up to 20 km, several well-logs in the region and a very accurate starting model, some issues remained. This shows the demand of further investigations before FWI can be used by default for data interpretation.

Beside the use of complex acquisition geometries, also a better description of the wave physics can lead to much better results. The literature shows some successful results of elastic FWI applied to ocean-bottom cable (OBC) or OBN field data (e.g., Sears et al., 2010), also in 3D (e.g., Vigh et al., 2014).

Whereas the elastic velocity models (P- and S-wave) can be estimated well from seismic data, the density parameter is still difficult to recover (Choi et al., 2008; Virieux and Operto, 2009), even for the synthetic case. Therefore, the density parameter is treated commonly only as passive parameter to enhance the velocity models (e.g., Przebindowska et al., 2012; Bai and Yingst, 2014) or even kept constant during the inversion (Brossier et al., 2009) and not used for interpretation. Despite the highlighting of the importance of density (e.g. Plessix et al., 2013), only very few authors were able to show a successful density inversion even in the synthetic case (Jeong et al., 2012). In the acoustic case, Bai and Yingst (2014) introduced a hierarchical strategy for density inversion and Qin and Lambare (2016) proposed a decoupled joint inversion.

Only very few papers are available showing the elastic inversion of streamer data. Köhn et al. (2012) showed a synthetic study using the Marmousi-II model in a marine environment, but with velocity receivers. In this controlled environment, the density could be reconstructed successfully. Shipp and Singh (2002) presented an elastic inversion strategy for wide-aperture streamer data, but only concentrated on the v_P result. In a third paper, Lu et al. (2013) show a promising synthetic case study for an elastic FWI of marine pressure data, but no field data application. So far, no publications could be found on the elastic inversion of a conventional 2D streamer field data set in a complex salt environment including deep water, especially not for the utilised data set.

1.3   Objectives of this work

FWI is often used to generate good velocity models for enhancing the migration result. However, a successful FWI is also able to generate highly detailed parameter models, which can be directly interpreted by geologists, as already shown by, e.g., Sirgue et al. (2010). The directly interpretable parameter models are one aim of this work.

Elastic inversion of streamer data was up to now only treated as wasted effort. Warner et al. (2012) state that the positive effect on the FWI results for moving from 2D to 3D is larger than for using the elastic approach instead the acoustic in 2D FWI. Despite the various new complex acquisition geometries and the acquisition of 3D data, most of the existing data are conventional 2D legacy data sets where I still see great potential for an enhancement in the data evaluation. Therefore, this work explores the potential of a standard elastic FWI applied to existing conventional streamer data sets.

In detail, this work covers the following main objectives:

- Is the acoustic approximation in FWI sufficient for marine streamer data and what are the advantages of elastic FWI?

- Relevance of density parameter for the inversion of marine streamer data.

- Is the flooding technique in FWI applicable to this field data set?

In order to answer these questions, several synthetic and field data inversions were conducted using a large marine field data set provided by Petroleum Geo-Services (PGS). One big challenge for FWI of this data set is the very large profile size, since FWI is still a computationally expensive method. The second challenge is the deep water of up to 3 km, increasing the model and, therefore, the computational time and memory requirements significantly. In addition, I use only a standard 2D marine streamer data set, no WAZ data, no OBN/OBC data, no 3D data and only pressure data are available.

1.4 Outline of thesis

After the introduction in this chapter, the basic principles of FWI are described in chapter 2. The main engine of the inversion, the forward modelling, is introduced. As part of the complete workflow I present the calculation of the gradient in the adjoint formulation up to the point of the model update, including the step length calculation. The third part of the theory chapter (section 2.4) deals with some practical issues, such as the estimation of the source wavelets and the role of density. As the used field data set was recorded with a dual-sensor streamer and subsequently the receiver ghost was removed by using the technique of wavefield separation, section 2.4.2 focuses on this topic.

Chapter 3 describes the model and data in more detail. After an introduction to the geology of the area where the survey took place, the parameter models used for FWI are presented. The following section deals with the field data including a description of the frequency content and occurring wave types. The next section informs about the few necessary preprocessing steps, before starting with the inversion.

Synthetic tests play an important role for a successful inversion to adjust the data- and model-dependent parameters for FWI. The tests and results are explained in chapter 4. I describe the modelling and inversion parameters, followed by a resolution test, the testing of the flooding technique and an examination of the picking accuracy of the salt boundaries.

After the synthetic tests the focus lies on the field data inversion (chapter 5) in several test applications. I analyse the influence of several factors on the inversion process, such as time windowing of the data, frequency filtering and the use of acoustic or elastic approaches. These tests help to become familiar with the data set and to further calibrate the parameters for the field data inversion.

Chapter 6 is divided into two parts. The first part in section 6.1 presents the starting model generation including the subsequent acoustic and elastic FWI results. The second part in section 6.2 shows the acoustic and elastic inversion results using a starting model provided by PGS.

In chapter 7 the FWI results are discussed and a geological interpretation is given. The last chapter gives an overall summary and provides some conclusions.

Chapter 2

Theory & Implementation

For this study the full-waveform inversion code IFOS2D was used. It is based on a 2D finite-difference (FD) scheme in the time domain (e.g., Tarantola, 1984; Gauthier et al., 1986; Crase et al., 1990). The forward modelling code was originally developed by Bohlen (1998, 2002). The propagation of elastic waves is modelled on a standard staggered grid (e.g., Virieux, 1986; Levander, 1988) in the stress-velocity formulation.

The following chapter gives an overview of the most important parts of the theory upon which the code is based. The chapter is divided into four sections, starting with the forward simulation of the wavefield (section 2.1). Using this as a basis, the next section describes the full-waveform inversion process itself (section 2.2). In section 2.4 some practical issues important for FWI are explained. This involves a brief description of the source time function inversion, as well as the role of density in FWI and a detailed explanation of the wavefield separation.

The equations in this chapter use the Einstein notation. If not declared otherwise, this convention implies a summation over repeated indices.

2.1 Forward simulation

The forward simulation of the wavefield is the basis of the inversion process. Most of the total computation time of FWI is consumed for wavefield simulations. For every iteration inside the inversion cycle, at least two modelling steps are necessary: the forward simulation of the wavefield and the backward propagation of the residual wavefield (adjoint state method). If the source time function inversion is used, one extra forward simulation is added per source location and frequency step. Also for the step length calculation, several additional forward calculations are needed.

This section contains three subsections. The first one explains the wave equation upon which the wavefield simulation is based (section 2.1.1), followed by a description of the criteria for

spatial and temporal sampling (section 2.1.2), and subsection 2.1.3 explains the boundary conditions, including the free surface.

2.1.1 Wave equation

The FWI workflow is based on a forward solver which calculates the wave propagation in an elastic medium. For an infinitesimally small deformation of an elastic medium the resulting deformation and the measurable displacement can be described by the equation of motion (Lay and Wallace, 1995)

$$\rho \frac{\partial^2 u_i}{\partial t^2} = f_i + \frac{\partial \sigma_{ij}}{\partial x_j} \,, \tag{2.1}$$

where ρ denotes the density of the medium, u_i the displacement of the particles in the medium, t the time, σ_{ij} the stress tensor and x_j the spatial dimensions. This equation relates the density-weighted acceleration on the left side to the body force density f_i on the medium and the stress gradient on the right side.

A stress applied on a body results in a strain of the body. By assuming a linear relation between the stress σ and the strain ϵ (valid for small deformations) Hooke's law can be applied and the stress tensor can be written as follows:

$$\sigma_{ij} = C_{ijkl} \epsilon_{kl} \tag{2.2}$$

The fourth-order tensor C_{ijkl}, called stiffness tensor, contains the elastic moduli which define the material properties. With its 81 elements the tensor relates the nine elements of stress with the nine elements of strain. Symmetry relations reduce the tensor to 21 independent components. Further reduction is possible by assuming an isotropic medium, which means that the stress-strain behaviour is independent of the direction in space. In this case, we have only two independent elastic moduli left, the Lamé parameters μ and λ. The first parameter μ is called shear modulus and relates the strain to shear stress. The second parameter λ has no physical meaning and is often replaced by the so called bulk modulus $\kappa = \lambda + \frac{2}{3}\mu$, relating the strain to pressure p (Fichtner, 2011). The stiffness tensor can then be written as

$$C_{ijkl} = \lambda \delta_{ij}\delta_{kl} + \mu(\delta_{ik}\delta_{jl} + \delta_{il}\delta_{jk}) \tag{2.3}$$

with the Kronecker delta

$$\delta_{ij} = \begin{cases} 1 & \text{for } i = j \\ 0 & \text{for } i \neq j \end{cases} . \tag{2.4}$$

The stress tensor has now the following form:

$$\sigma_{ij} = \lambda \Theta \delta_{ij} + 2\mu \epsilon_{ij} \,, \tag{2.5}$$

where Θ is the trace of ϵ_{ij} ($\Theta = \epsilon_{11} + \epsilon_{22} + \epsilon_{33}$) and the strain-displacement relationship is

given by

$$\epsilon_{ij} = \frac{1}{2} \left(\frac{\partial u_i}{\partial x_j} + \frac{\partial u_j}{\partial x_i} \right) . \tag{2.6}$$

The stress-displacement formulation of equations 2.1, 2.5 and 2.6 can also be written in the stress-velocity formulation, as used in the IFOS2D code:

$$\begin{aligned}
\rho \frac{\partial v_i}{\partial t} &= f_i + \frac{\partial \sigma_{ij}}{\partial x_j} \\
\frac{\partial \sigma_{ij}}{\partial t} &= \lambda \frac{\partial \Theta}{\partial t} \delta_{ij} + 2\mu \frac{\partial \epsilon_{ij}}{\partial t} \\
\frac{\partial \epsilon_{ij}}{\partial t} &= \frac{1}{2} \left(\frac{\partial^2 u_i}{\partial t \partial x_j} + \frac{\partial^2 u_j}{\partial t \partial x_i} \right) = \frac{1}{2} \left(\frac{\partial v_i}{\partial x_j} + \frac{\partial v_j}{\partial x_i} \right) .
\end{aligned} \tag{2.7}$$

This system of first-order partial differential equations describes the propagation of seismic waves in an elastic medium. It will be solved by using the finite-difference (FD) method (e.g., Alford et al., 1974). In the FD method, the partial derivatives in time and space are replaced by finite differences. Now, waves can be modelled on a rectangular grid in a Cartesian coordinate system. As the code uses higher-order finite-difference spatial operators, the standard staggered grid (SSG) scheme is used to ensure a stable and accurate forward modelling. In this SSG scheme, the material properties and wavefield variables are not located at the same grid point, but shifted by the distance of half a grid point (e.g., Levander, 1988; Virieux, 1986).

The relation between the Lamé parameters, density and the compressional and shear wave velocity (v_P and v_S) is given by (Fichtner, 2011)

$$v_P = \sqrt{\frac{\lambda + 2\mu}{\rho}} = \sqrt{\frac{\kappa + \frac{4}{3}\mu}{\rho}} \tag{2.8}$$

$$v_S = \sqrt{\frac{\mu}{\rho}} . \tag{2.9}$$

The scalar pressure can be calculated by a sum over the diagonal components of the stress tensor.

2.1.2 Grid dispersion and Courant criterion

In order to sample the wavefield sufficiently well on the SSG, the distance between grid points need to be defined carefully. The grid size has a major impact on the computational effort. On the one hand, as few grid points as possible are desired, on the other hand, a minimum number of grid points per minimum wavelength is required to avoid numerical artefacts caused by grid dispersion. The term *grid dispersion* describes the phenomenon of numerical dispersion due to the usage of a low number of grid points per wavelength λ, whereby the calculated wavefield seems to be dispersive. Following the Nyquist-Shannon sampling theorem (Shannon, 1949) it is necessary to sample the wavefield with $dh \leq \frac{\lambda}{2}$. The variable dh describes the spatial distance of two horizontally or vertically adjacent grid points. However, as I use a finite-

difference operator as approximation, the sampling needs to be increased, depending on the order of the operator (Köhn, 2011)

$$dh \leq \frac{\lambda_{min}}{n} = \frac{v_{min}}{n f_{max}}. \tag{2.10}$$

The variable n describes the number of grid points per wavelength. The minimum wavelength λ_{min} can be calculated by using the minimum of the P- and S-wave velocity of the model, v_{min}, and the maximum frequency, f_{max}. For the Nyquist-Shannon sampling theorem, $n \geq 2$ would be sufficient. For the FD modelling, n must be set to a larger number. The order of the operator describes the truncation error of the Taylor series of the FD operator. With increasing order the accuracy of the operator also increases. Therefore, a lower FD order requires a higher number of grid points n per minimum wavelength λ_{min}. In this work, I use an 8th-order FD operator in space in the acoustic case, which requires at least $n = 5$ samples per minimum wavelength. When using second order in the elastic case, n already increases to 12.

The second sampling criterion that needs to be considered is related to the time sampling dt. The time sampling has a huge influence on the stability of the simulation. I use the Courant-Friederichs-Lewy criterion (Courant et al., 1928, 1967) to ensure stability:

$$dt \leq \frac{dh}{h\sqrt{2}v_{max}} \tag{2.11}$$

with v_{max} as maximum of the P- and S-wave velocity and the additional factor h representing the Taylor operator. The value of h is calculated by summing up all Taylor (weighting) coefficients of the forward (or backward) operator. For second order $h = 1$, for 8th order it increases to $h = 2161/1680$.

2.1.3   Boundary conditions

To avoid reflections at the edges of the model used for the wavefield simulation, boundary conditions need to be introduced. The easiest way is to add several grid points in all dimensions and apply a damping factor in this area (Cerjan et al., 1985). All waves travelling into the boundary are damped to zero (absorbing boundary). For a better performance, perfectly matched layers (PML) were developed, where a complex damping function is applied within the boundary area (Collino and Tsogka, 2001). As this method still needs dozens of grid points, Komatitsch and Martin (2007) and Martin and Komatitsch (2009) enhanced the PML, which leads to the convolutional perfectly matched layer (C-PML). The C-PML needs only 10-20 grid points to avoid reflections at the boundary. For the optimal definition of the damping function, the dominant frequency needs to be specified.

For the surface, the free surface condition is applied, where the surface acts as a mirror and sends all arriving waves back into the model. In contrast to the implicit definition, where a layer of air is added on top of the surface, the model ends abruptly at the surface. This

leads to less computational time and less required memory due to a lower number of grid points. The disadvantage of this method is that the free surface implementation in the code does not allow any topography, only a horizontal surface. As my data were acquired offshore in a marine environment, a water surface with no topography can be assumed. Therefore, I can use the imaging method proposed by Levander (1988) and Robertsson et al. (1995). This mirroring technique is applied for all experiments.

2.1.4 Wavefield visualisation

The code allows to write out snapshots of the wavefield during the forward modelling at discrete times. By saving the pressure wavefield (diagonal component of the stress tensor) the propagation can be monitored.

To study the elastic properties of the wavefield, snapshots of the spatial divergence and the magnitude of the curl of the particle velocity wavefield are written out (Bohlen, 1998). After Morse and Feshbach (1953) and Dougherty and Stephen (1988), the divergence is related to the compressional energy (E_P) and the curl to the shear energy (E_S). They are defined as

$$E_P = (\lambda + 2\mu)(\nabla \cdot \vec{v})^2 \ , \tag{2.12}$$

$$E_S = \mu(-\nabla \times \vec{v})^2 \, . \tag{2.13}$$

2.2 Full-waveform inversion

The forward simulation described in the previous chapter is the core of the full-waveform inversion workflow. The main advantage of the FWI approach is the utilisation of the full information content of the data. Not only the first arrivals of the main events are used for model building but also smaller events and, most importantly, the waveforms themselves in amplitude and phase. Taking this additional information into account can lead to a model including structures of sub-wavelength size (Virieux and Operto, 2009). In figure 2.1 the FWI workflow is displayed. It always starts with a forward simulation of the wave propagation with a given acquisition geometry in a starting model. The simulated synthetic data and the field data can then be compared. With the help of an objective function the residual energy is calculated (in case of the most common $L2$-norm, see section 2.2.2). The residual energy describes the energy not explained by the simulation in the starting model. Now, the residual data are propagated backwards in time from the receiver positions through the same model. The residuals focus in the parts of the model where the starting model could not describe the data very well.

To go back into the model space, the cross-correlation of the forward-propagated wavefield and the back-propagated residual wavefield is calculated. The solution represents the model gradient for a single source. The method to calculate the gradient is known as the adjoint approach (see also section 2.2.1). Now we can sum up the gradients over all shots. After

computing a scaling of the update (section 2.2.6) and applying possible modifications to the gradient, e.g., a suppression of the update in certain areas (section 2.2.5), the starting model is updated and the forward simulation is starting again. This process is iterated until a stop criterion is reached. This stop criterion can be a given maximum number of iterations or the decrease of the misfit value below a given threshold.

As described in the introduction, wavefield-separated data were used for this work. Therefore, the wavefield separation was implemented after the forward modelling, in addition to the normal workflow described above. In figure 2.1 the wavefield separation is marked with a red box and further described in section 2.4.2. The code IFOS2D is available under the terms of the GNU General Public License (`http://www.gpi.kit.edu/Software.php`). For more details about the code I refer to Köhn (2011) and Groos (2013).
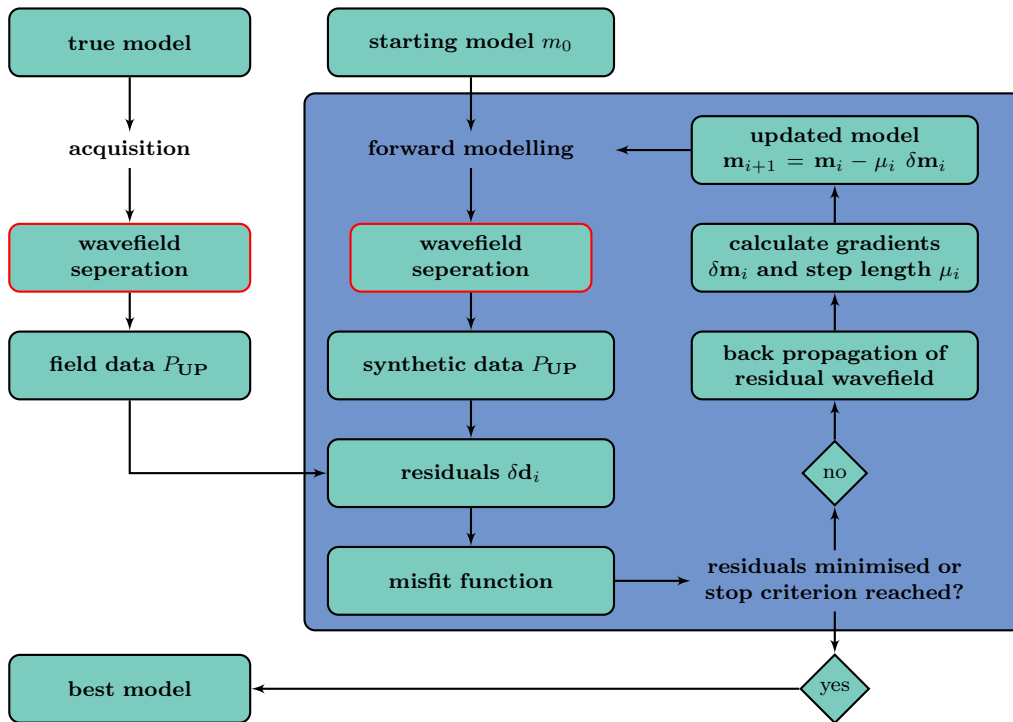

Figure 2.1: Workflow of the FWI process. The blue box indicates the loop over the iteration steps.

2.2.1   Inverse problem

The goal of seismic inversion is to minimise the misfit between observed data $\mathbf{d}_{obs}$ and synthetic data $\mathbf{d}_{syn}$, forward modelled in a given model. A starting model $\mathbf{m}_0$, which describes the subsurface below the measured profile as best as possible, is then updated iteratively. How the model is altered after each iteration is described by the gradient. The gradient depends on the data misfit

$$\delta\mathbf{d} = \mathbf{d}_{syn} - \mathbf{d}_{obs}\,. \tag{2.14}$$

In order to minimise the misfit an objective function must be chosen. The most common one is the L_2-norm:

$$E(\mathbf{m}) = \frac{1}{2}\delta\mathbf{d}^T\delta\mathbf{d} \tag{2.15}$$

where the superscript T denotes the transpose. By summing the residuals over the number of time samples, the number of sources and the number of receivers, $E(\mathbf{m})$ describes the elastic energy of the data not described by the model. The lower the residual energy, the better the model explains the data. Therefore, the improvement of the model is achieved by minimising the data misfit.

It needs to be mentioned that the results of FWI are highly ambiguous. As in all inversion methods, different models can explain the data with a similar misfit. Therefore, the choice of the objective function, controlling the update, is crucial.

To linearise the problem we assume only small changes in the model and data. Thus, we can apply the Born approximation. The model $\mathbf{m}$ can be described by a reference model $\mathbf{m}_0$ and the small perturbation $\delta\mathbf{m}$:

$$\mathbf{m} = \mathbf{m}_0 + \delta\mathbf{m} \tag{2.16}$$

The residual energy in equation 2.15 is now expanded in a Taylor series around $\mathbf{m}_0$:

$$E(\mathbf{m}) = E(\mathbf{m}_0 + \delta\mathbf{m}) = E(\mathbf{m}_0) + \delta\mathbf{m}\frac{\partial E(\mathbf{m}_0)}{\partial\mathbf{m}} + \mathcal{O}(\mathbf{m}^2) \tag{2.17}$$

In the following, we will neglect the higher-order terms. In order to minimise the residual energy the partial derivative of $E(\mathbf{m})$ with respect to the model $\mathbf{m}$ must be zero:

$$\frac{\partial E(\mathbf{m})}{\partial\mathbf{m}} = \frac{\partial E(\mathbf{m}_0)}{\partial\mathbf{m}} + \delta\mathbf{m}\frac{\partial^2 E(\mathbf{m}_0)}{\partial\mathbf{m}^2} = 0 \tag{2.18}$$

The perturbation model can now be written as

$$\delta\mathbf{m} = -\left(\frac{\partial^2 E(\mathbf{m}_0)}{\partial\mathbf{m}^2}\right)^{-1}\frac{\partial E(\mathbf{m}_0)}{\partial\mathbf{m}}. \tag{2.19}$$

Let us take a closer look at the two parts of this equation. The first partial derivative of the objective function describes the steepest-descent direction

$$\frac{\partial E(\mathbf{m}_0)}{\partial\mathbf{m}} = \frac{\partial\mathbf{d}_{syn}(\mathbf{m}_0)}{\partial\mathbf{m}}^T(\mathbf{d}_{syn}(\mathbf{m}_0) - \mathbf{d}_{obs}) = \mathbf{J}_0^T\delta\mathbf{d}\,, \tag{2.20}$$

where the Fréchet derivative matrix, also called Jacobian matrix, is denoted by $\mathbf{J}$.

The second derivative of $E(\mathbf{m})$ is called Hessian Matrix $\mathbf{H}$ and is composed of two Fréchet matrices and the first derivative of the Fréchet matrix multiplied by the data misfit:

$$\frac{\partial^2 E(\mathbf{m}_0)}{\partial\mathbf{m}^2} = \mathbf{J}_0^T\mathbf{J}_0 + \left(\frac{\partial\mathbf{J}_0}{\partial\mathbf{m}}\right)^T\delta\mathbf{d} = \mathbf{H}_0 \tag{2.21}$$

By using equation 2.20 and 2.21 we can write 2.19 as

$$\delta\mathbf{m} = -\mathbf{H}_0^{-1}\mathbf{J}_0^T\delta\mathbf{d}\,.$$

(2.22)

Following equation 2.16, we can finally update the model iteratively by using the Newton method (Tarantola, 2005):

$$\mathbf{m}_{n+1} = \mathbf{m}_n - \mathbf{H}_n^{-1}\left(\frac{\partial E}{\partial\mathbf{m}}\right)_n$$

(2.23)

As the computation of the inverse Hessian matrix is very costly, a common method is the approximation of the Hessian matrix by neglecting the second order derivative, also called Gauss-Newton method (Pratt et al., 1998):

$$\mathbf{H}_0 \approx \mathbf{H}_a = \mathbf{J}_0^T\mathbf{J}_0$$

(2.24)

The model can now be updated in the following way:

$$\mathbf{m}_{n+1} = \mathbf{m}_n - \mathbf{H}_{a,n}^{-1}\left(\frac{\partial E}{\partial\mathbf{m}}\right)_n$$

(2.25)

The most simple update method for FWI is the steepest descent method. In this method, the Hessian is replaced by a step length μ, scaling the gradient:

$$\mathbf{m}_{n+1} = \mathbf{m}_n - \mu_n\left(\frac{\partial E}{\partial\mathbf{m}}\right)_n\,.$$

(2.26)

The step length has to be chosen carefully to allow a fast enough convergence but not to miss the minimum. A preconditioning operator $\mathbf{P}$ can also be used in addition to the step length to control the behaviour of the gradient, as described in subsection 2.2.5.

In my FWI workflow, the conjugate gradient approach is used. This method is similar to the steepest descent method, but it can increase the convergence speed. The conjugate gradient direction is calculated from the current preconditioned steepest descent direction and the weighted gradient from the previous iteration.

2.2.2　　Objective function

The aim of the full-waveform inversion process is to obtain a model describing the data as best as possible. In order to measure the quality of the model, the field data and synthetic modelled data are used to calculate an objective value, the match of the data. The most common objective function is the least-squares norm, or L_2-norm:

$$E_{L2} = \frac{1}{2}\sum_s\sum_r\int_T(\mathbf{d}_{syn} - \mathbf{d}_{obs})^2\,dt\,.$$

(2.27)

The squared data residuals are summed over the number of receivers, number of sources and number of time steps.

A modified version of the L_2-norm uses normalised seismograms (Choi and Alkhalifah, 2012). As the normalisation proved to be more robust (Przebindowska, 2013), this version of the objective function is used:

$$E_{L2,norm} = \frac{1}{2} \sum_s \sum_r \int_T \left(\frac{\mathbf{d}_{syn}}{||\mathbf{d}_{syn}||} - \frac{\mathbf{d}_{obs}}{||\mathbf{d}_{obs}||} \right)^2 dt \,. \tag{2.28}$$

The normalisation reduces the influence of geometrical spreading effects on the amplitude. Therefore, near and far offsets contribute equally to the misfit.

2.2.3   Adjoint approach

The numerical calculation of the Fréchet derivatives requires a number of forward calculations equal to the number of model parameters. By using the adjoint approach (Tarantola, 1984; Mora, 1987; Tromp et al., 2005; Plessix, 2006) the necessary forward calculations are reduced to two.

To improve the clarity of the following chapter I switch to the frequency domain. For a small perturbation in the model the wavefield for one source-receiver-pair for one reflection point can now be described as the multiplication of the Green's function (impulse response) for the path between the source position and the reflection point $G(\mathbf{x}, \mathbf{x}_s, \omega)$, the model perturbation $\delta \mathbf{m}(\mathbf{x})$ and the Green's function of the path between the reflection point and the receiver position $G(\mathbf{x}_r, \mathbf{x}, \omega)$. By integrating the multiplication over the full model volume the full wavefield for a single scatterer is derived:

$$\delta d(\mathbf{x}_r, \mathbf{x}_s, \omega) = \omega^2 f(\omega) \int_V \delta m(\mathbf{x}) \, G(\mathbf{x}, \mathbf{x}_s, \omega) \, G(\mathbf{x}_r, \mathbf{x}, \omega) \, dV \tag{2.29}$$

Now we have derived the wavefield for one source-receiver pair for a small perturbation in the model and source term f. In reality, we do not have the perturbation of the model $\delta \mathbf{m}$ but the difference of the observed data and the modelled data, which is $\delta \mathbf{d}$. In order to modify the starting model $\mathbf{m}_0$ such that it can describe the reality we need to minimise the difference of the two wavefields. Therefore, a misfit function is used, e.g. the L_2-norm, in order to quantify the energy not described by the starting model (for details see chapter 2.2.2):

$$E = \frac{1}{2} \int_\omega \sum_s \sum_r |\delta d(\mathbf{x}_r, \mathbf{x}_s, \omega)|^2 \, d\omega \tag{2.30}$$

with $\delta d(\mathbf{x}_r, \mathbf{x}_s, \omega) = d_{syn}(\mathbf{x}_r, \mathbf{x}_s, \omega) - d_{obs}(\mathbf{x}_r, \mathbf{x}_s, \omega)$.

Now the gradient can be calculated as derivative of the misfit function with respect to the model parameters:

$$\boldsymbol{\gamma}(\mathbf{x}) = \frac{\partial E}{\partial \mathbf{m}} \tag{2.31}$$

By inserting the misfit function into equation 2.31 and splitting $\delta\mathbf{d}$ into imaginary and real part $|\delta\mathbf{d}|^2 = \delta\mathbf{d}_r^2 + \delta\mathbf{d}_i^2$, the above equation can be written as (Pratt et al., 1998)

$$\frac{\partial E}{\partial m(\mathbf{x})} = \frac{1}{2} \int\limits_{\omega} \sum_s \sum_r \frac{\partial}{\partial\mathbf{m}} |\delta d(\mathbf{x}_r, \mathbf{x}_s, \omega)|^2 \, d\omega \tag{2.32}$$

$$= \frac{1}{2} \int\limits_{\omega} \sum_s \sum_r \left(2\,\delta\mathbf{d}_r \frac{\partial\mathbf{d}_r}{\partial\mathbf{m}} + 2\,\delta\mathbf{d}_i \frac{\partial\mathbf{d}_i}{\partial\mathbf{m}} \right) d\omega \tag{2.33}$$

$$= \int\limits_{\omega} \sum_s \sum_r \Re \left[\frac{\partial d(\mathbf{x}_r, \mathbf{x}_s, \omega)}{\partial\mathbf{m}} \delta d^*(\mathbf{x}_r, \mathbf{x}_s, \omega) \right] d\omega \,, \tag{2.34}$$

with $\delta d^*(\mathbf{x}_r, \mathbf{x}_s, \omega)$ as complex conjugate of $\delta d(\mathbf{x}_r, \mathbf{x}_s, \omega)$. The symbol $\Re$ denotes the real part.

By using the Born approximation for a single scattered wavefield (equation 2.29) the Fréchet derivatives in equation 2.34 can be written as

$$\frac{\partial d(\mathbf{x}_r, \mathbf{x}_s, \omega)}{\partial\mathbf{m}} = \omega^2 \, f(\omega) \, G(\mathbf{x}, \mathbf{x}_s, \omega) \, G(\mathbf{x}_r, \mathbf{x}, \omega) \,. \tag{2.35}$$

Now, the gradient has the form

$$\boldsymbol{\gamma}(\mathbf{x}) = \int\limits_{\omega} \sum_s \sum_r \Re \left[\omega^2 \, f(\omega) \, \delta d^*(\mathbf{x}_r, \mathbf{x}_s, \boldsymbol{\omega}) \, G(\mathbf{x}, \mathbf{x}_s, \omega) \, G(\mathbf{x}_r, \mathbf{x}, \omega) \right] d\omega \tag{2.36}$$

or

$$\boldsymbol{\gamma}(\mathbf{x}) = \int\limits_{\omega} \sum_s \sum_r \Re \left[\omega^2 \underbrace{f(\omega) \, G(\mathbf{x}, \mathbf{x}_s, \boldsymbol{\omega})}_{\text{forward wavefield}} \underbrace{\delta d^*(\mathbf{x}_r, \mathbf{x}_s, \omega) \, G(\mathbf{x}_r, \mathbf{x}, \omega)}_{\text{backward wavefield}} \right] d\omega \,. \tag{2.37}$$

The complex conjugate function $\delta\mathbf{d}^*$ represents a time reversal in the time domain.

Switching back to the time domain, equation 2.36 for the gradient corresponds to a zero-lag cross-correlation between the forward propagated wavefield and the wavefield of the backward propagated residuals. The total gradient is a sum over the gradients of all shots.

The update of the model can now be performed in the following way:

$$\mathbf{m}_{n+1} = \mathbf{m}_n + \mu_n \boldsymbol{\gamma}_n \tag{2.38}$$

with μ as step length.

2.2.4   Gradients

In IFOS2D the calculation of the gradients can be performed for different parametrisations: density and Lamé parameters, or density and v_P and v_S velocity. Köhn et al. (2012) studied the differences of both parametrisations and recommend the usage of density, v_P and v_S velocity. Therefore, this parametrisation is used in this work for all inversions. By using the relations after Köhn et al. (2012), the gradients for all three parameters can be expressed as

follows:

$$\frac{\partial E}{\partial v_P} = 2\,\rho\,v_P \frac{\partial E}{\partial \lambda} \tag{2.39}$$

$$\frac{\partial E}{\partial v_S} = -4\,\rho\,v_S \frac{\partial E}{\partial \lambda} + 2\,\rho\,v_S \frac{\partial E}{\partial \mu} \tag{2.40}$$

$$\frac{\partial E}{\partial \rho} = (v_P^2 - v_S^2)\frac{\partial E}{\partial \lambda} + v_S^2 \frac{\partial E}{\partial \mu} + \frac{\partial E}{\partial \rho} \tag{2.41}$$

with

$$\lambda = \rho(v_P^2 - 2v_S^2)\,, \tag{2.42}$$

$$\mu = \rho\,v_S^2\,. \tag{2.43}$$

2.2.5 Preconditioning of the gradient

The preconditioning of the gradient allows to enhance or suppress updates in certain areas of the model. After summation of the gradients for all shots a weighting matrix $\mathbf{P}$ with values between zero and one is multiplied with the gradient. The weighting matrix has the same size as the model and the gradient. The areas in the gradient matrix where the corresponding values in the weighting matrix are zero do not contribute to the model update. In marine environments it is common practise to suppress updates in the water column as this area is mostly homogeneous and well known (Kurzmann, 2012). Equation 2.26 changes to

$$\mathbf{m}_{n+1} = \mathbf{m}_n - \mu_n \mathbf{P}_n \left(\frac{\partial E}{\partial \mathbf{m}}\right)_n. \tag{2.44}$$

2.2.6 Step length estimation

The scaling of the gradient is a crucial part in the FWI workflow. The step length controls the impact of the update on the model. In the beginning, when the errors are large, large step lengths can be applied to ensure a fast convergence. In the vicinity of the minimum, the step length has to be reduced in order to avoid missing the minimum in the misfit. In IFOS2D a parabolic line search method is implemented as proposed by Nocedal and Wright (1999). The model is updated for three different step lengths and a forward simulation performed for a subset of shots. By calculating the misfit values for all three step lengths, the optimal step length can be approximated by using a parabolic fit through all three misfit values and determining the minimum of the parabola.

By using only a subset of shots for calculating the step length and forcing the inversion to iterate for a given minimum number of iterations per frequency, it is possible that the misfit value increases locally. Overall, the misfit should decrease continually, though.

2.2.7   Multiscale approach and filter

One big issue in the process of FWI is the ambiguity and the risk of cycle-skipping. Cycle-skipping describes the adaptation of an event in the synthetic data to a wrong event in the field data during the FWI workflow. The wrong adaptation happens when in the starting model a structure is not placed accurately enough and, therefore, the corresponding events in the modelled and field data are shifted by more than half a wavelength. Especially for models with high velocity contrasts, e.g. models including salt bodies, small location errors of these interfaces can already produce cycle-skipping and consequently artefacts in the model. To mitigate this effect, frequency filtering is applied (Bunks et al., 1995). The inversion starts with low frequency content, which reduces the risk for cycle-skipping and leads to a more linear misfit function. After the inversion converged for a given frequency range, the upper corner of the frequency filter is moved stepwise to higher frequencies. The minimum and maximum frequencies of each step are defined in the input file of IFOS2D.

The filtering of the modelled and observed data is done by using a 4th order Butterworth filter. To see how the filter works and behaves, the filtered averaged frequency content of one exemplary shot gather is plotted in figure 2.2. The filled black area represents the frequency content of the filtered shot gather. For comparison, the frequency content of a non-filtered shot gather is plotted as black dashed line. The title shows the cut-off frequency of the 4th order low-pass filter. The frequency plot shows that the filtered shot gather contains frequency parts up to the double of the specified low-pass filter frequency in decreasing proportion. The flat slope is necessary to avoid filter artefacts. On the other hand, the flanks of the filter should be as steep as possible to avoid dispersion artefacts due to an insufficient spatial sampling. Therefore, I chose a compromise by using a 4th order filter. In this work, I always specify the filter frequencies and not the actual frequency content of the data.
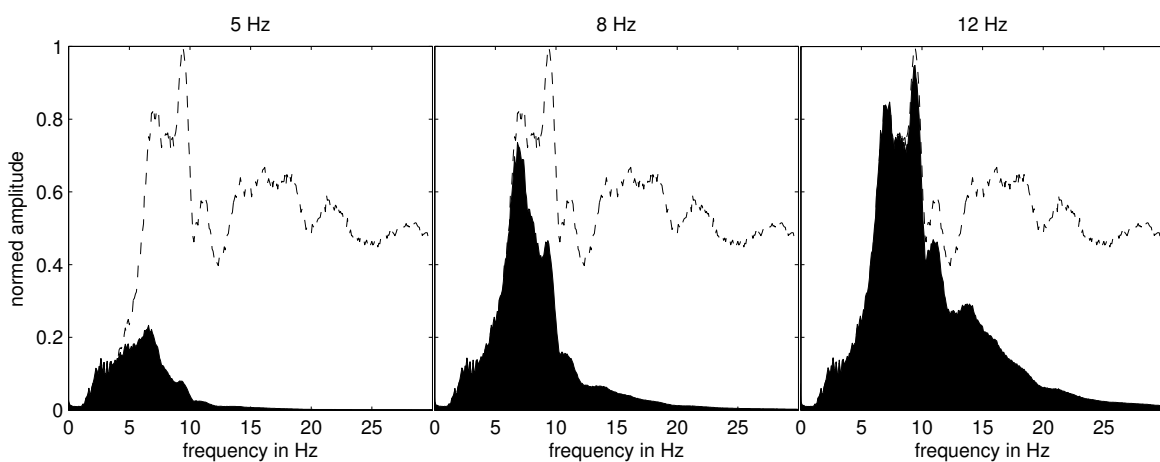
Figure 2.2: Averaged frequency content of an exemplary shot gather filtered by a low-pass Butterworth filter for selected cut-off frequencies (black areas). For comparison, the averaged frequency content of a non-filtered shot gather is plotted (dashed black line).

In Sirgue and Pratt (2004), a formula is presented to calculate the bandwidth for the next frequency step. The formula ensures a coverage of all wavenumbers and a small number of

frequency steps simultaneously, in order to make the inversion run as fast as possible. For synthetic tests, large frequency steps work well. However, field data include a lot of effects that the inversion cannot take into account, such as noise or 3D-effects. Therefore, small frequency steps proved to stabilise the inversion and support the convergence. I increase the frequency bandwidth in steps of 1 Hz for field-data inversions.

The usable frequency bandwidth depends on the acquisition (depth of streamer towing, noise, etc.). Usually, the lowest usable frequencies are between 2-5 Hz in marine acquisition. As explained above, the lower the usable frequency content, the better for full-waveform inversion.

2.3   Source time function inversion

The source wavelet is usually not known, at least not exactly. But as we compare the field data with synthetic shot gathers, the source wavelet can play a major role in FWI. A wrong wavelet can have a big influence on the result of FWI. Therefore, we need to determine the source wavelet s of the field data as best as possible. This is done by using a source time function (STF) inversion. Pratt (1999) proposed an iterative, linear least-squares optimisation inversion. The method is based on a deconvolution of the field data and synthetic data, implemented in the frequency domain:

$$s(\omega) = \frac{\mathbf{d}_{syn}^T \mathbf{d}_{obs}^*}{\mathbf{d}_{syn}^T \mathbf{d}_{syn}^*} \tag{2.45}$$

A stabilised version of this least-squares inversion is implemented in IFOS2D. For more information I refer to Groos (2013). The method needs an initial wavelet and a model including all important structures in order to produce synthetic data comparable to the field data. Thus, the STF inversion needs to be monitored carefully. Especially for marine measurements the source wavelets should be similar for all shots. If this is not the case the used model is not good enough for the source wavelet inversion, or other parameters or assumptions are incorrect (e.g., acoustic approximation in an elastic medium). In the beginning of each frequency step, the STF inversion is calculated to ensure the usage of the best model. Even for marine data, for which the source wavelet is usually well known, an STF inversion is useful to compensate insufficiencies in the model or modelling (e.g., elastic effects in the acoustic approximation).

After the STF inversion a taper can be applied to the wavelet. I use a cosine taper window with the four corners 0 s, 0 s, 0.4 s and 1 s (see figure 2.3). The first two values describe the start value and end value of the first slope, increasing from zero to one. The second two values of the taper describe start value and end value of the second slope, decreasing from one to zero. As the first two values are zero, only the second slope exists. The taper ensures a compact wavelet and removes later parts resulting from an insufficient model. The taper is long enough that it does not have to be enlarged for low frequencies and can be kept constant for the whole inversion.

If not declared otherwise, I used a $\sin^3$ wavelet as starting wavelet for the SFT inversion or for test modellings and inversions. The wavelet is generated by calculating $\sin^3$ between zero and π. This wavelet was chosen as starting wavelet because it has the lowest content of higher frequencies above the centre frequency of all built-in source wavelets in IFOS2D in order to avoid dispersion artefacts during modelling.
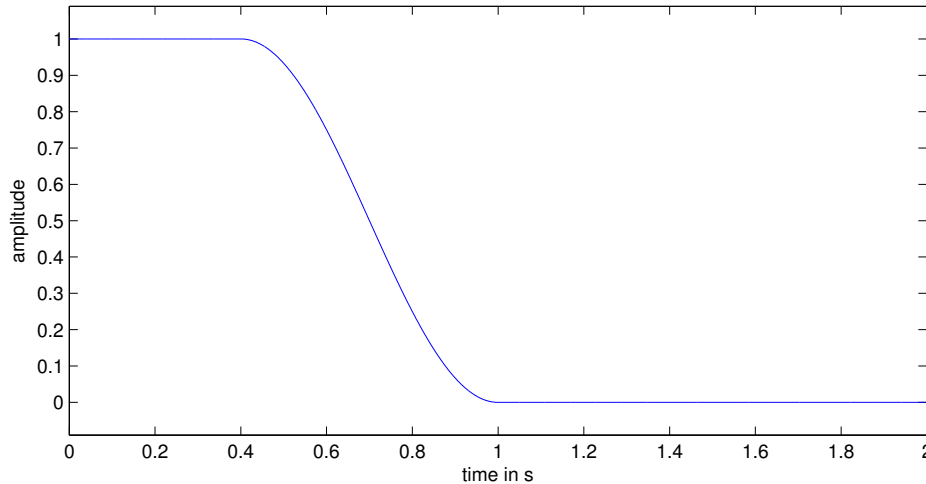

Figure 2.3: Cosine taper for an inverted source wavelet with the corner frequencies 0 s, 0 s, 0.4 s and 1 s.

2.4   Practical issues

2.4.1   Density in FWI

If using FWI for generating velocity models to enhance a conventional migration result, only the v_P model is necessary. Therefore, the density parameter is commonly only used as passive parameter to collect artefacts from non-physical modelling in order to enhance the inversion result of the velocity models (e.g., Przebindowska et al., 2012; Bai and Yingst, 2014). Other authors keep the density model constant (e.g., Brossier et al., 2009), or update the density model by an empirical relation from the velocity model.

Recently, the parameter models of FWI have become more and more interesting for a direct interpretation (e.g., Sirgue et al., 2010). In this case, the density parameter is very important to interpret the parameter models geologically. In addition, the density contrasts mainly affect the amplitudes of reflected waves (Qin and Lambare, 2016). As the data used in this work was acquired in deep water, it mainly consists of reflection data and no diving waves and only few refracted waves. This makes the density important for a successful FWI.

2.4.2   Wavefield separation

In standard marine acquisition, streamers with pressure sensors are generally used. The receiver ghost is a common effect which can be observed as notches in the frequency spectrum

of the data. The notches in the frequency spectrum can be considerable and limit the frequency bandwidth. To understand how the receiver ghost is generated, we take a look at one wave path of an event in the marine acquisition geometry: The wave is moving upwards from the subsurface and arrives at the streamer, where it is recorded. After passing the streamer, the wave is back-reflected downwards at the sea surface. The reflected downgoing wave passes the streamer shortly after the first recording again, like an echo, but with switched polarity. As the pressure sensors are not sensitive to the direction, the waves are recorded with reverse polarity. This has the effect of cancellation of amplitudes in some places in the wavefield, which introduces notches in the frequency spectrum (see figure 2.6a). The location of the notches depends on the angle of the arriving wave, the frequency and the depth of the streamer. Vertical velocity sensors have the advantage of sensitivity to the direction of the wave. As the reflected wave travelling downwards passes the streamer from the opposite direction compared to the first upgoing wave, the polarity is switched again. Thus, the effect of cancellation also appears, but at different locations and, therefore, for different frequencies (see figure 2.6b). By using a streamer with pressure and vertical velocity sensors (figure 2.4), both recorded data sets can be combined in order to remove the notches to make the data more broadband. More broadband data leads also to a better resolution of the imaging result, independent of the method. One additional advantage is the possibility to tow the streamer deeper. This increases the low-frequency content of the data. Also the weather independency during the acquisition can be increased (Carlson et al., 2007). With a deeper tow in bad weather conditions the noise level remains the same as in good weather conditions using a shallower tow. When towing a conventional streamer deeper, even more notches appear in the important low-frequency band.
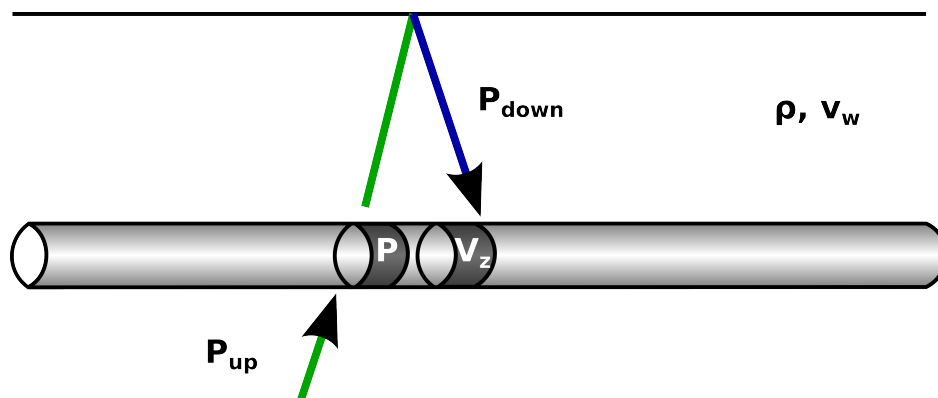
Figure 2.4: Dual-sensor streamer: the upgoing wavefield is plotted in green, the downgoing wavefield in blue, reflected at the water surface. The reflection coefficient of the water-air interface is assumed as $R \approx -1$.

In figure 2.5 an exemplary shot gather is displayed of a synthetic modelling using the model shown in figure 4.1b, recorded with pressure sensors and vertical velocity receivers. The comparison of the shot gathers reveals a similar appearance. The same number of events in the same places are visible, only the amplitude of the direct wave appears to decay very fast with increasing time and offset in the v_z shot gather. A comparison of the clipping of the colour scale shows also a very different overall amplitude level. This difference appears

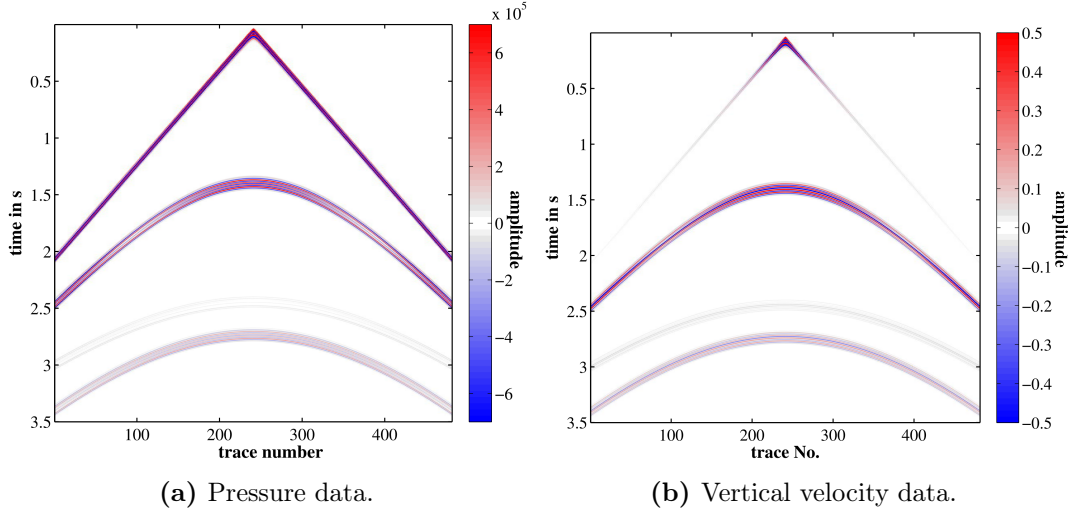**(a)** Pressure data.

(b) Vertical velocity data.

Figure 2.5: Exemplary shot gather of both modelled data sets, using the model shown in figure 4.1b.

also when both shot gathers are transformed to the frequency-wavenumber (FK) domain (figure 2.6a-2.6b). For this reason the velocity data need to be raised to a similar level as the pressure data by using a filter F before combining the two data sets in the FK domain. The filter F is shown in figure 2.6c. Starting with the equation of motion a relation between the pressure wavefield P and the wavefield of the vertical velocity v_z can be derived (Amundsen, 1993):

$$\frac{\partial V_z}{\partial t} = \frac{1}{\rho}\frac{\partial P}{\partial z} \tag{2.46}$$

A transformation to the frequency and wavenumber domain gives us

$$i\omega V_z = -\frac{1}{\rho}ik_z P$$
$$\Leftrightarrow P = -\frac{\rho\omega}{k_z}V_z = -F \cdot V_z \tag{2.47}$$

with ω as angular frequency, k as wavenumber and the filter

$$F(\omega, k_z) = \frac{\rho\omega}{k_z}, \tag{2.48}$$

shown in figure 2.6c. Only the vertical part is considered in the last equation. This can be justified by the fact that I have deep water of about 3 km and only 10 km of streamer. Waves travelling in horizontal direction such as the direct waves are destroyed during the wavefield separation and cannot be used for FWI.

In a streamer acquisition geometry we have only wavenumbers in the horizontal direction. Therefore, we need to calculate the vector of the vertical angular wavenumbers k_z with the

(a) Pressure data

(b) Vertical velocity data

(c) Filter

(d) P_{up} data
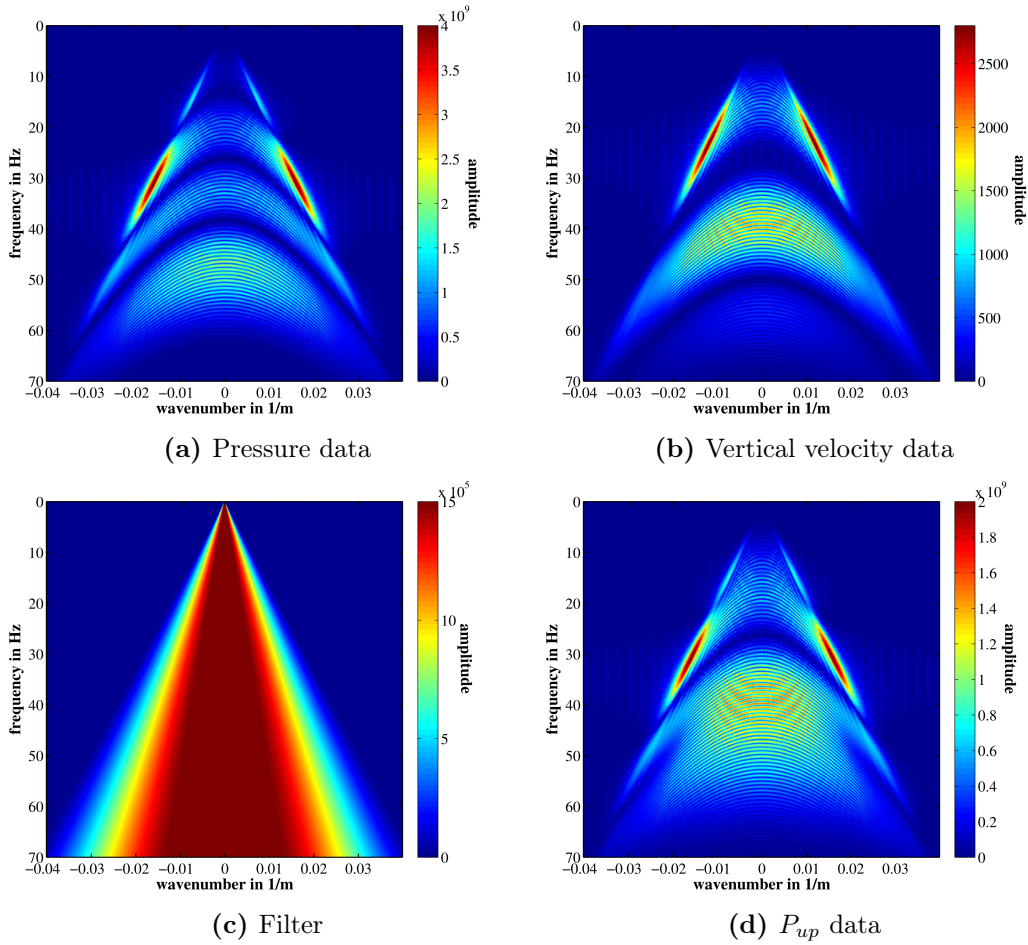
Figure 2.6: Wavefield separation in the FK domain. The used model is a two-layer model with the source at 15 m and the receivers at 30 m depth. After a transformation to the FK domain, the data can be combined with the help of a filter in order to get only the upgoing part of the shot gather (P_{up}).

help of the dispersion relation (here shown in 2D):

$$\left(\frac{\omega}{v_w}\right)^2 = k_x^2 + k_z^2 \tag{2.49}$$

$$\Leftrightarrow k_z = \sqrt{\left(\frac{\omega}{v_w}\right)^2 - k_x^2} \tag{2.50}$$

where v_w denotes the velocity in water.

By utilising the directional information in the sign of the k_z vector the pressure data can now be divided into an upgoing wavefield P_{up} and a downgoing wavefield P_{down} (Klüver, 2008):

$$P_{up} = \frac{1}{2}(P - FV_z) \qquad (2.51)$$

$$P_{down} = \frac{1}{2}(P + FV_z) \qquad (2.52)$$

$$\text{with} \qquad P = P_{up} + P_{down} \qquad (2.53)$$

The notches in the FK spectrum appear as hyperbolic shadows with very low amplitudes. In the FK spectrum of the pressure wavefield in figure 2.6a, five notches can be identified. The apexes are located at $k = 0 \ \frac{1}{\mathrm{m}}$ and the frequencies 0 Hz, 12 Hz, 25 Hz, 40 Hz and about 65 Hz. The FK spectrum of the V_z wavefield only contains two notches at about 25 Hz and 50 Hz. The upgoing pressure wavefield P_{up} in the frequency domain is displayed in figure 2.6d. Three of four visible notches of the pressure wavefield could be removed. The remaining notch existed in the FK spectrum of both the velocity and pressure wavefields at the same location (at about 25 Hz for this acquisition geometry) and could, therefore, not be removed.

In figure 2.7 the effect of the wavefield separation is shown in the time domain for an exemplary reflection, including a receiver ghost. The upper plot shows the total wavefield and the lower two plots the separated wavefield into the upgoing and downgoing part. The total wavefield was separated almost perfectly into the upgoing and downgoing part.

In summary, the wavefield separation has not only advantages for conventional processing methods, but also for FWI. More broadband data is achieved resulting in a better signal-to-noise ratio. Also, the deeper towing leads to more energy at lower frequencies, one of the most important requirements for a successful FWI.
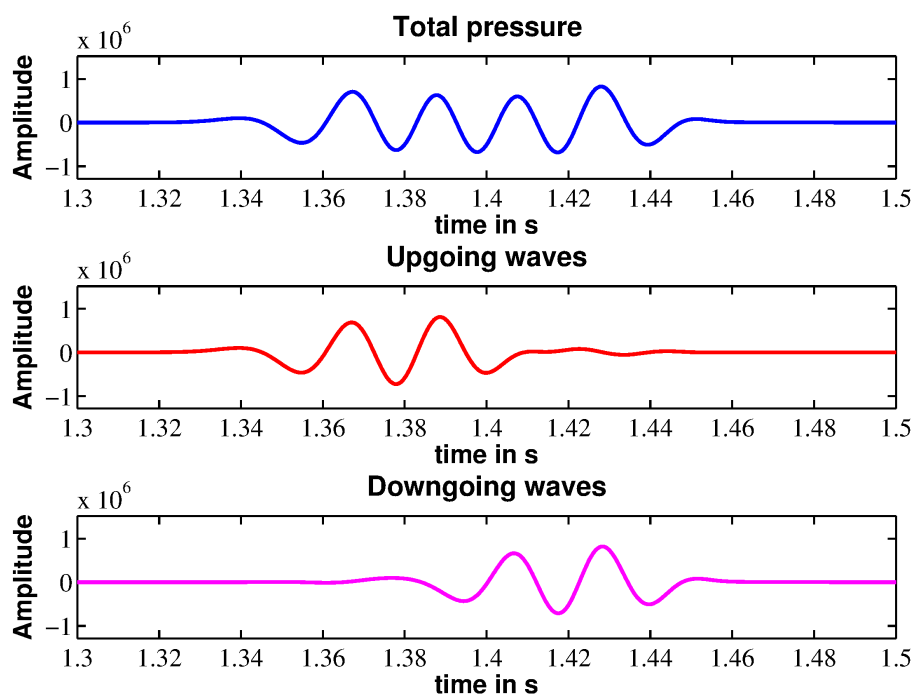
Figure 2.7: Exemplary trace before and after wavefield separation. Displayed is the first modelled reflection of the interface of trace 240 using the model shown in figure 4.1b.

Chapter 3

Data & Model

In this chapter all ingredients and preparations needed for FWI are explained. This includes a detailed description of the field data used in this work (section 3.3). The area where the data set was acquired and the associated geological environment are described in section 3.1. Before the data could be used for FWI, several preprocessing steps were applied. A description of all preprocessing steps can be found in section 3.4. The company Petroleum Geo-Services (PGS) provided me not only with the data set but also with a velocity model, which is shown and described in section 3.2. The provided model was used as true model for the synthetic tests, and as reference or starting model for the field data inversion.

3.1   Geology of the acquisition area

The data were recorded offshore Angola, south-west Africa, in the Kwanza Basin (figure 3.1). In the north, the Kwanza Basin is connected with the lower Congo Basin and in the south with the Namibe Basin. As the area is part of the Aptian Salt Basin, it is characterised by very complex geology (Valle et al., 2001), created by raft tectonics (e.g., Duval et al., 1992; Lundin, 1992). The model of raft tectonics describes rift tectonics active above salt layers, where undeformed blocks of sediments (rafts) are separated by deformation (rifting).

During the evolution of the Kwanza Basin, the layers were tilted in the direction of the Atlantic ridge. The heavy load of the layered sediments and the tilt of the sediments resulted in high strain rates, acting on the overburden. Due to the presence of salt layers, representing a potential gliding layer, the sediment layers above the salt started to move down the slope. This gravity-driven process is also called gravity gliding (Duval et al., 1992). As a result of active rifting processes, the overburden was stretched and separated by normal faulting into several blocks (see figure 3.2). The movement of the blocks relative to each other formed valleys at the surface, which were filled up with younger sediments. During the ongoing process of stretching, the load of the sediments in the valleys could increase the separation of the blocks. This process is called gravity spreading (Valle et al., 2001). When the blocks are no longer in mutual contact, they are called rafts. The stretching of the overburden can be
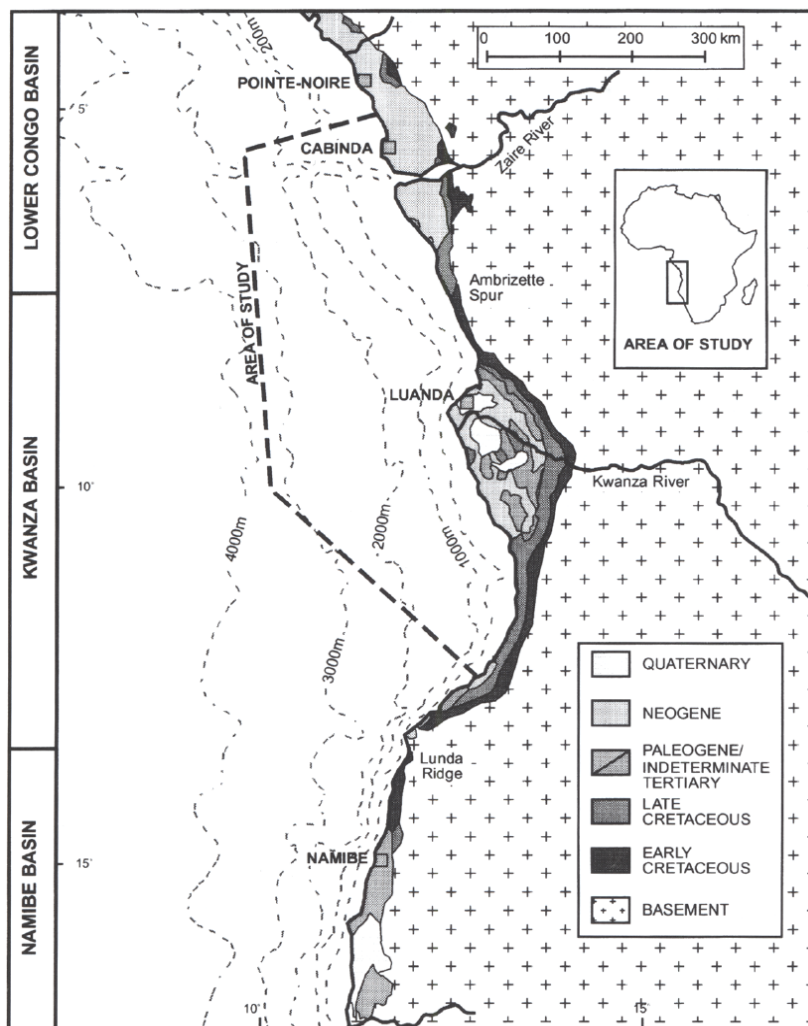
Figure 3.1: Geological map of acquisition area, including onshore geology and the main rivers. Source: Spathopoulos (1996).

separated into two (Duval et al., 1992) to three periods (Valle et al., 2001). The first period started in the Early Cretaceous, the Aptian, 110 Ma (million years) ago. The last period is still active.

During the stretching process, the salt could rise at fault locations and formed diapirs. This resulted in a combination of rafts, sediments of different age and thickness and, additionally, salt layers with high raised diapirs. The structures below the salt are generally unrelated to the rafting process as the salt acts as a decoupling horizon for the tectonic stresses. Oil has been found in almost all stratigraphic units (Brognon and Verrier, 1966).

In figure 3.3, an interpreted cross-section of the lower Kwanza Basin is shown. It sketches the complex geology with its many faults in the region, also described by Valle et al. (2001). The cross-section represents only an example and vary laterally due to the complex tectonic setting. Thus, the subsurface may be different below the profile utilised in this work. The total stratigraphy of the Kwanza Basin contains sediment layers of up to several 100 m thickness. Above the basement, the subsurface is composed of fluvial and lacustrine rocks followed by
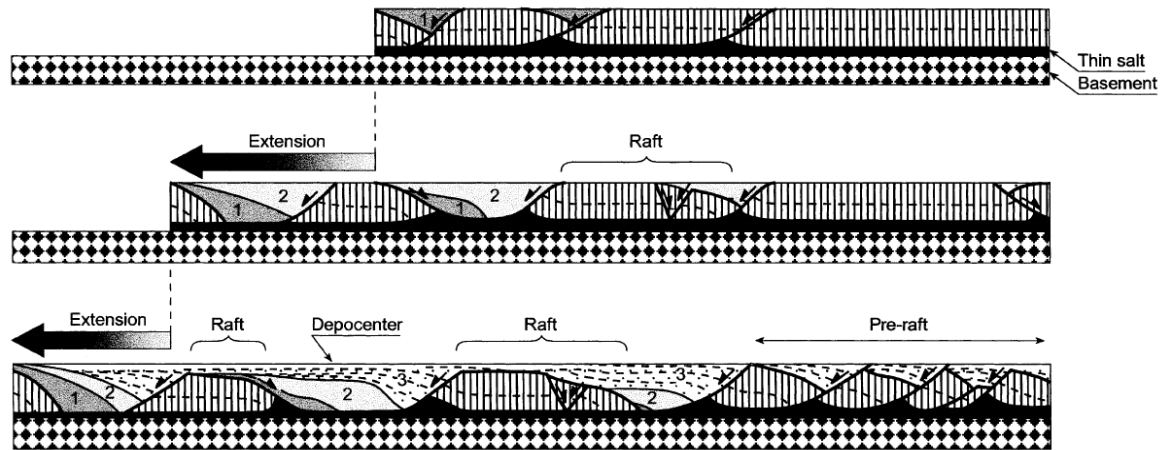
Figure 3.2: During the process of raft tectonics the sediments are extended and faults occur which are refilled. The salt layer acts as a decoupling horizon: the basement is undisturbed. The salt can rise at faults and form diapirs. Source: Duval et al. (1992).

the deposition of Aptian salt. During the Aptian, the deposits of salt stopped and changed to the deposition of carbonates due to marine ingression. The Carbonates were interpreted as dolomite and limestone. The Aptian is overlain by Late Cretaceous and Tertiary siliciclastics (Jiang et al., 2014). Spathopoulos (1996) showed that those sediments mainly consist of shales with intercalated sandstone layers. The stratigraphic column of the Kwanza Basin is shown in figure 3.4.

In table 3.1 the elastic parameters of the formations are given that are expected in the sediment layers above the salt. It can be observed that some formations have very similar elastic parameters, such as dolomite and limestone. Also the salt has very similar v_P and v_S values compared to limestone and dolomite and differs only in its density from the carbonate rocks. This already shows the importance of a full elastic inversion in order to be able to interpret the resulting parameter models directly.

Table 3.1: Elastic parameters of the formations expected in the sediment layers above the salt. Source: Bourbié et al. (1987)

formation	v_P in $\frac{m}{s}$	v_S in $\frac{m}{s}$	density in $\frac{kg}{m^3}$
Saturated shales and clays	1500-2200	500-750	2100-2400
Porous and saturated sandstones	2000-3500	800-1800	2100-2400
Limestone	3500-6000	2000-3300	2400-2700
Dolomite	3500-6500	1900-3600	2500-2900
Salt	4500-5500	2500-3100	2100-2300

For the used data set, a migration result was determined by PGS using a Kirchhoff depth migration, shown in figure 3.5a. The purple events indicate high impedance contrasts and high reflectivity in the subsurface. The white zone with no events in the shallow part of the model represents the water column. For the depth migration, the v_P velocity model displayed in figure 3.5c was used. The most prominent feature is the salt body, coloured in yellow ($v_P = 4500 \frac{m}{s}$). The salt body is heavily structured with several diapirs and strong topography.
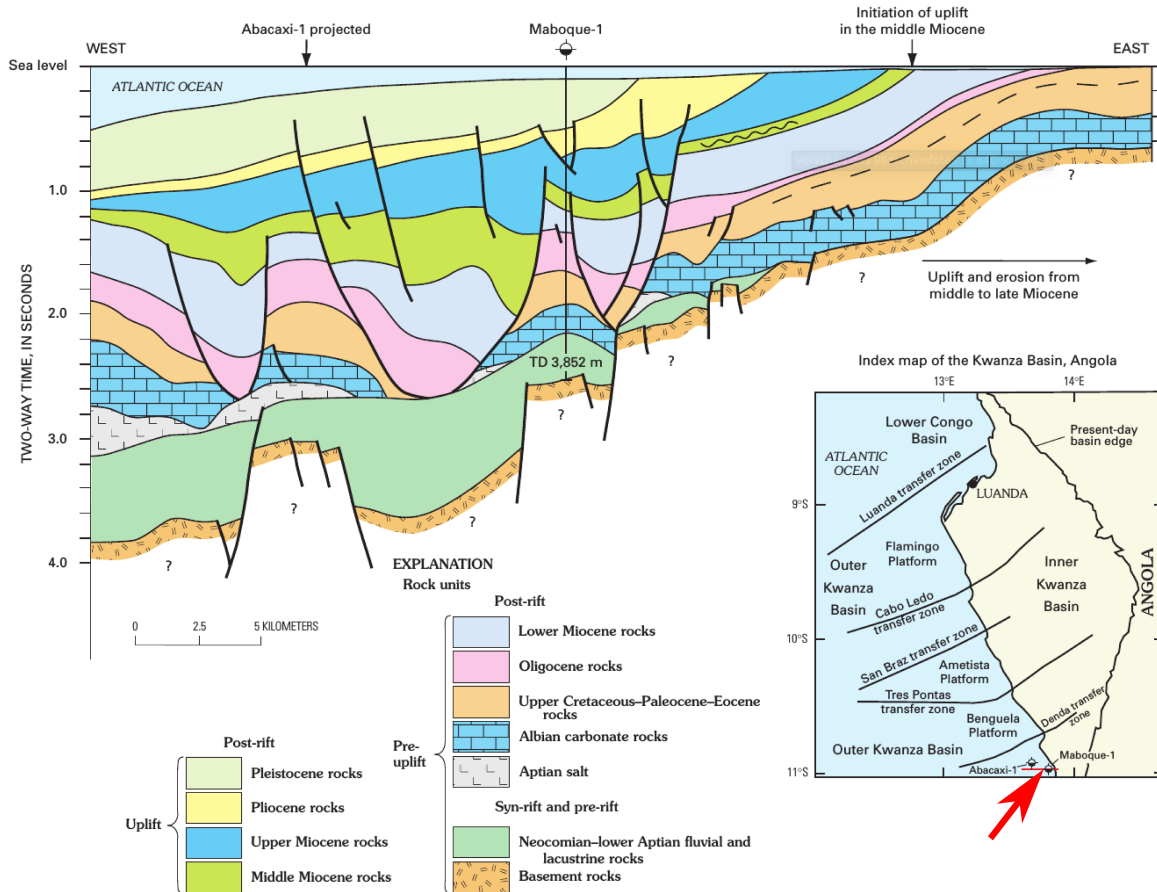
Figure 3.3: Schematic cross-section of the lower Kwanza Basin. The red arrow indicates the location of the cross-section (red line). Source: Brownfield and Charpentier (2006).

The sediments above the top of salt (TOS) show up as constant depth-dependent gradient in the velocity model. The migration shows several layered structures in the sediments above the TOS, not included in the velocity model. For instance, a thin layer with high reflectivity is visible in the zoom of figure 3.5a. Below the salt layer, no clear structures are visible in both models.

3.2   Parameter models

PGS provided me with a 2D P-wave velocity model, obtained from migration velocity analysis (MVA). This model was used for several synthetic tests, for quality control of the starting models created by the flooding technique and as starting model for FWI tests.

The model was provided in SEG-Y format. The model format was changed to SU format by using the SU program *segyread*. The model includes the sea floor, the salt layer and a sediment gradient as background (figure 3.5c). It has a size of 265 km in length (x-direction) and 15 km in depth. The water has a depth of a few hundred metres up to more than three kilometres. The salt layer consists of a thin layer on the left from model coordinate 0-170 km in a depth of about 3 km below sea floor. Additionally, the salt formed canopies rising up to
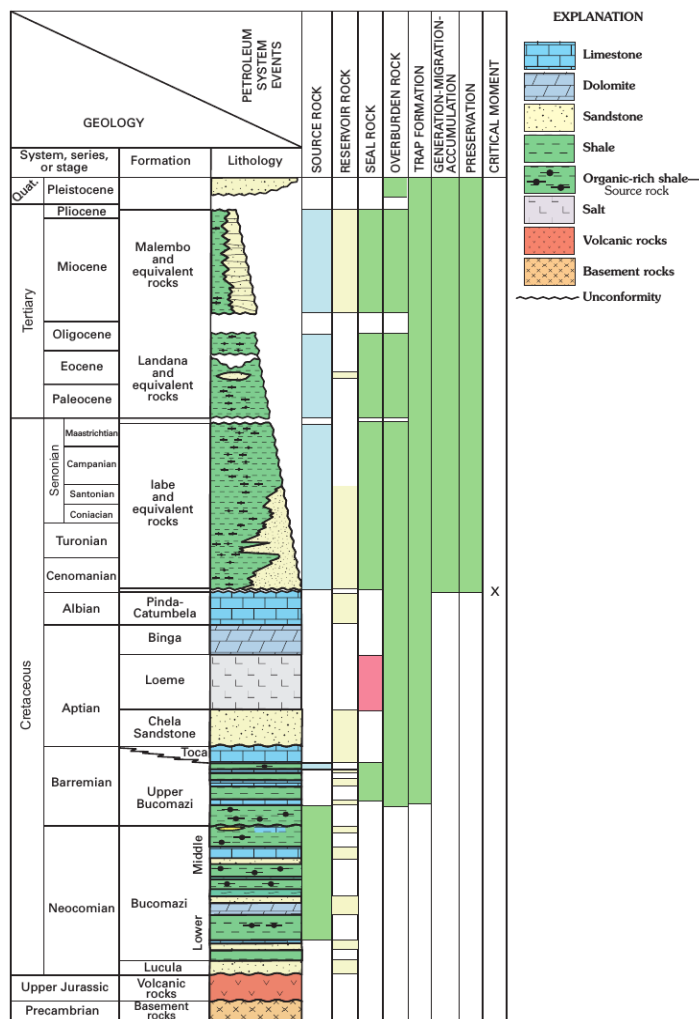
Figure 3.4: Stratigraphy of the Kwanza Basin. Source: Brownfield and Charpentier (2006).

the water bottom. On the right side of the model the thickness of the salt layer increases up to over 5 km. Also, in this area the salt body is located only a few hundred metres below the sea floor.

For the inversion, the provided velocity model was modified slightly as described in the next paragraph. In deep water environments the water velocity has to be considered carefully. The deeper the water column, the larger the influence of a wrong water velocity on the kinematics of the wavefield. A brief calculation shows that a velocity error of only 10 $\frac{m}{s}$ in the water column leads to a location error of the sea bottom of 20 m. Due to the acquisition geometry, especially vertical location errors influence the data and inversion. To avoid a location error of the seabed due to a wrong assumed water velocity, forward modellings were performed with different water velocities and compared to the field data. The tests yielded a water velocity of 1490 $\frac{m}{s}$, which was used for the model. This value matches well with the velocities in the PGS model and also with literature (Leroy et al., 2008). The P-wave velocity of the sediments increase from water velocity up to 7000 $\frac{m}{s}$. The velocity of the salt was set to 4500 $\frac{m}{s}$ as given in the PGS model.

As the profile is rather long, this work focuses on the last 88.5 km in x-direction and only 12 km in depth for FWI. The used part of the model is shown as green box in figure 3.5c and is called model 2 in the following. For testing purpose the even smaller model indicated by the red box in figure 3.5c was used (see also section 5). This subarea is 20 km in length and 8 km in depth and is called model 3.

The original grid spacing of the model is 50 m in horizontal direction and 10 m in vertical direction. For the modelling and inversion the grid of the model was changed to an equidistant grid with a spatial sampling interval of 12.5 m in both directions. This distance correlates with the receiver distance (section 3.3.1). Therefore, the receivers are located exactly on the grid and as few grid points as possible are needed in order to optimize the computational cost.

Table 3.2: Properties of model 2.

Property	Value
Model size (length × depth)	88.5×12 km
Minimum v_P	$1490 \; \frac{\text{m}}{\text{s}}$
Maximum v_P	$5700 \; \frac{\text{m}}{\text{s}}$
Minimum density	$1020 \; \frac{\text{kg}}{\text{m}^3}$
Maximum density	$2700 \; \frac{\text{kg}}{\text{m}^3}$
Minimum v_S	$1 \; \frac{\text{m}}{\text{s}}$
Maximum v_S	$3300 \; \frac{\text{m}}{\text{s}}$
Water layer depth	$\sim 2.5\text{-}3.7$ km

The density model and the shear wave velocity model were calculated from the v_P model. For the density model, the Gardner relation was used (Gardner et al., 1974) in the following form:

$$\rho = 230 \cdot (k \cdot v_P)^{0.25}, \tag{3.1}$$

where $k = \frac{1}{0.3048}$ is the factor to convert the formula from feet to metre. For the density in water, a value of $1020 \; \frac{\text{kg}}{\text{m}^3}$ was used.

The v_P-v_S ratio is given by

$$\frac{v_P}{v_S} = \sqrt{\frac{1 - \sigma}{0.5 - \sigma}} \tag{3.2}$$

with σ as Poisson's ratio (Reynolds, 1997). For salt, the Poisson's ratio varies between 0.2 and 0.3 (Liang et al., 2007). By assuming an average Poisson's ratio of 0.25, a v_P-v_S ratio of $\sqrt{3}$ results. This value was used to compute the shear wave velocity from the v_P model for v_P velocities higher than $4000 \; \frac{\text{m}}{\text{s}}$. For sediments lower than $4000 \; \frac{\text{m}}{\text{s}}$, a v_P-v_S ratio of 4 was used, following the literature (Bourbié et al., 1987). In fluids the shear modulus is zero and, therefore, also v_S. As zero in the models can cause mathematical problems during divisions, the v_S value was set to the very low value of one in the water column. All parameter models for model 2 are displayed in figure 3.6.
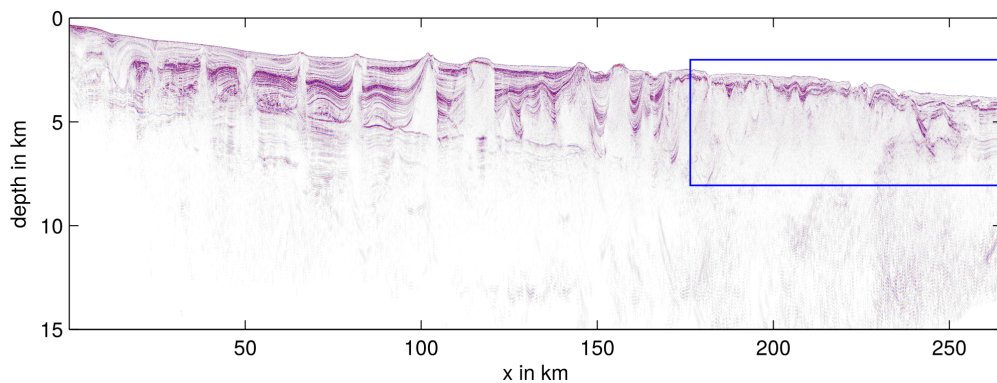
(a) Migration result based on the full model shown in figure 3.5c). The blue box indicates area of the zoom shown in figure 3.5b.
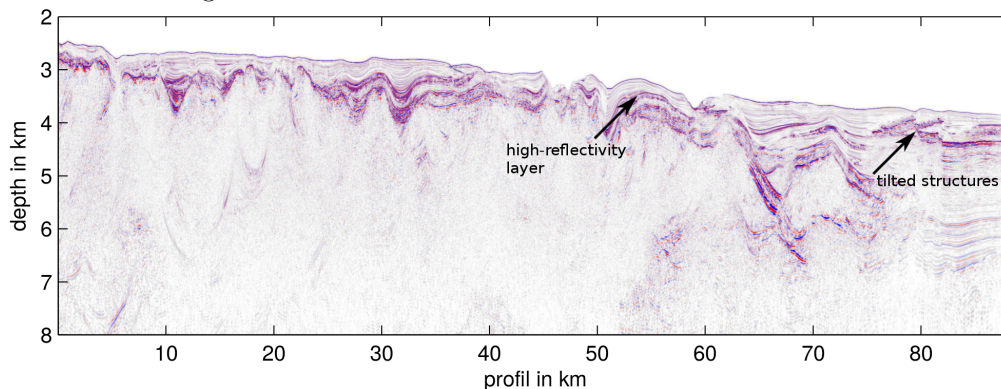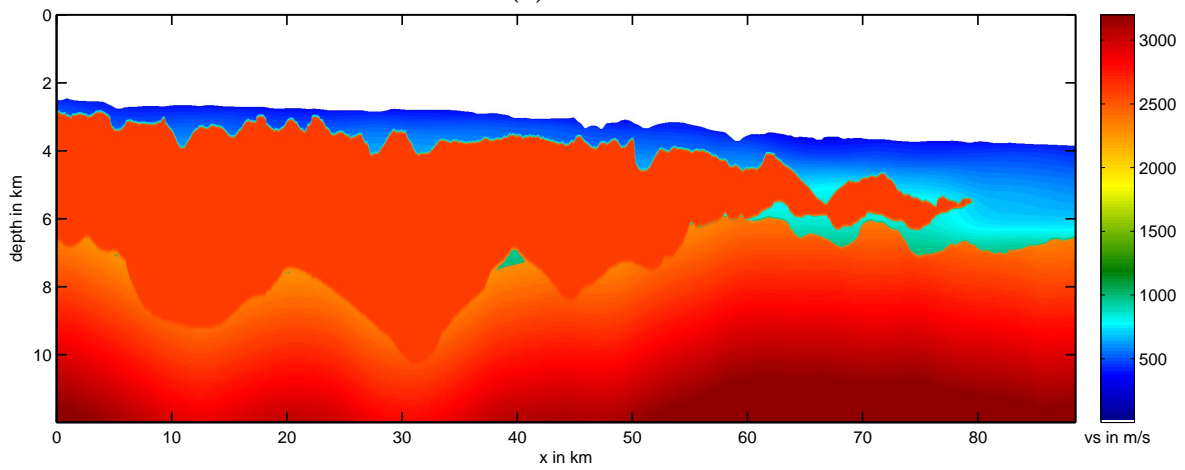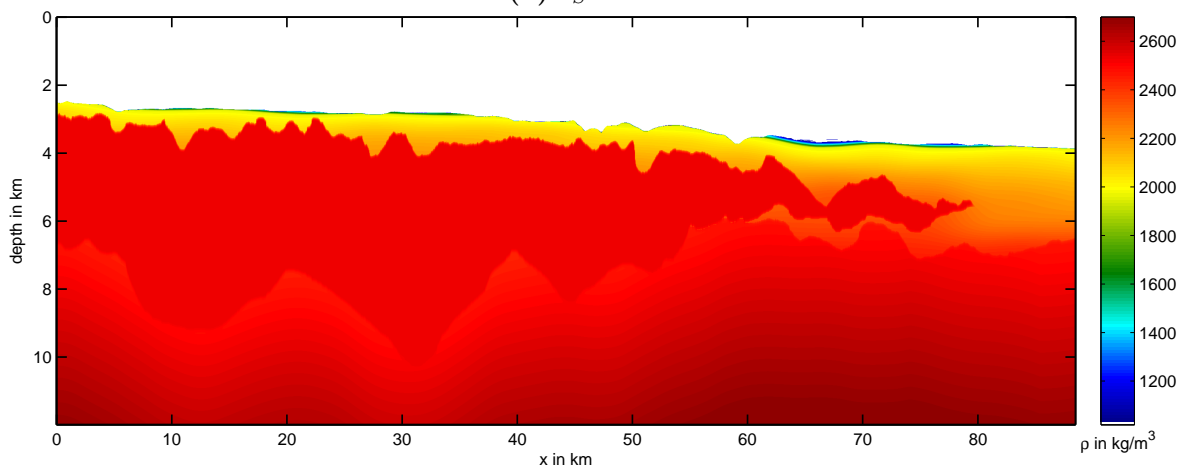

(b) Zoom of the migration result shown in the blue box in figure 3.5a).
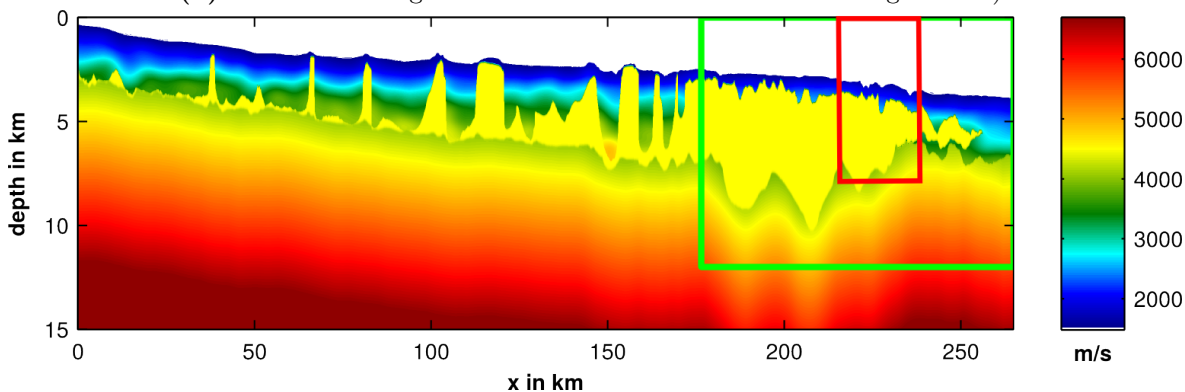
(c) Provided P-wave velocity model. The green box indicates the subarea of the model used for FWI (model 2). The smaller red box indicates the subarea used for testing (model 3). The white areas indicate water velocity (1490 $\frac{m}{s}$).

Figure 3.5: Migration result and v_P model provided by PGS.
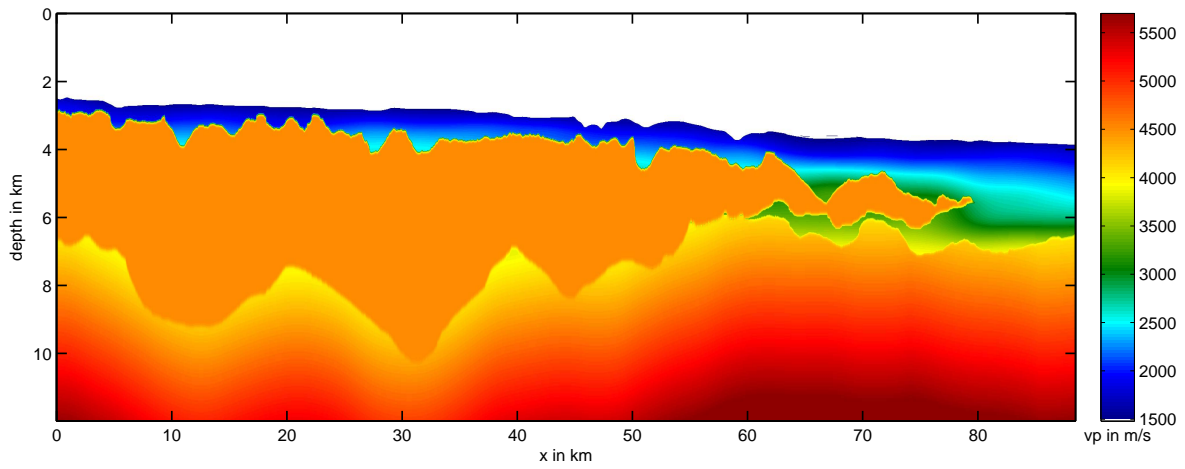
(a) v_P model.

(b) v_S model.

(c) Density model.

Figure 3.6: P-wave, S-wave and density parameter for model 2.

3.3   Field data

The provided data are marine streamer data of one line from a major project recorded offshore Angola, West Africa (see figure 3.7a). In figure 3.7b, a zoom of the area is shown where the data were acquired, including the survey lines. One of the lines perpendicular to the coastline was used in this work. A detailed description of the exact profile location cannot be given due to confidentiality reasons. I refer to Lesley Auchterlonie (PGS, London) for more information.

The data were acquired 2011 with a dual-sensor streamer. Thus, every receiver consists of a pressure sensor and a co-located vertical velocity sensor, leading to two data sets for every shot. Both data sets were combined to perform the wavefield separation (see section 2.4.2). In this work, only the upgoing part of the recorded wavefield was available and used.

For the description of wavepaths, the abstraction of rays will be used. This approximation simplifies the understanding and explanations of wavepaths and is widely used in geometrical optics.

3.3.1   Acquisition geometry

The acquisition geometry is a standard 2D towed streamer geometry. The air gun source was towed behind the vessel in 8 m depth below the sea surface. The streamer was located in 20 m depth (see figure 3.8). The first receiver was located 100 m behind the source. The streamer included 804 receiver groups separated by 12.5 m, resulting in a maximum offset of 10 137.5 m. Shots were triggered every 50 m. A summary is shown in table 3.3.

Table 3.3: Acquisition geometry assuming a still-water geometry and a group spacing of 12.5 m.

number of shots	number of receivers per shot	shot interval	minimum offset	maximum offset	depth of source	depth of streamer
5305	804	50 m	100 m	10 137.5 m	8 m	20 m

The depth of the streamer was deeper than usual towing depth of conventional streamers of about 10 m. For streamers with only pressure sensors, the towing depth is dictated by the receiver ghost, introducing notches in the spectrum of the data. For streamers towed deep, the notches caused by receiver ghost move into the part of the seismic frequency bandwidth used for processing. For a streamer in 20 m depth, the first three notches in the frequency spectrum resulting from the receiver ghost are located at about 0 Hz, 37.5 Hz and 75 Hz. The notch at 37.5 Hz is right in the middle of the seismic frequency range and does not occur in a towing depth of 10 m. The usage of the dual-sensor technology (see section 2.4.2) allows to tow a streamer in 20 m depth and remove several notches after the acquisition. The deeper towing has several advantages, such as an increased weather independency and more broadband data (see 2.4.2).

Due to ocean currents and tides the streamer was not always perfectly aligned with the profile
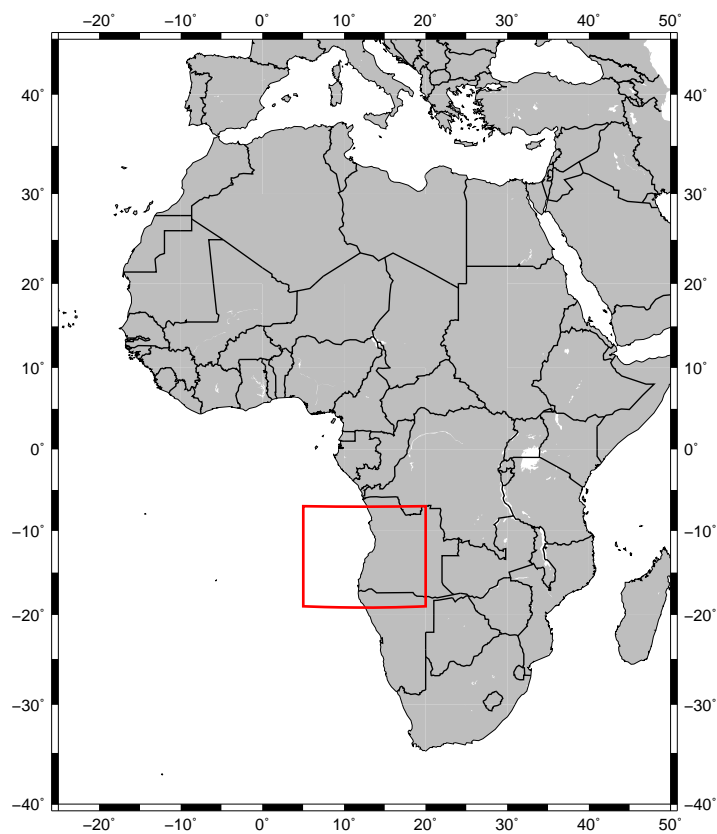
(a) Map of Africa with longitude on the horizontal axis and latitude on the vertical axis. The red rectangle shows the area where the data of the project were acquired.
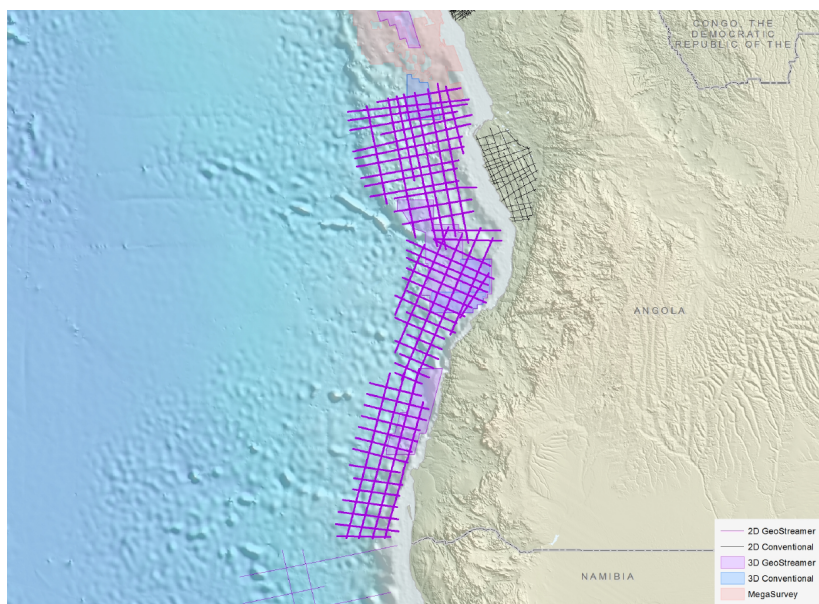
(b) Zoom of the red rectangle shown in figure 3.7a. The purple lines show the acquisition lines of the survey. Source: Petroleum Geo-Services (2018)

Figure 3.7: Map of the acquisition area.

on which the vessel was moving. This deviation of the streamer from a straight line is called streamer feathering. The locations of the shots and receivers are plotted in figure 3.9. The profile was shot in two parts. At about x=100 km the vessel had to turn and restart the shooting for the second part of the profile. The vessel was moving from the right profile edge to the left. The origin is on the left side, following the original numbering in the headers. Without streamer feathering all blue lines in figure 3.9 (receivers) would perfectly follow the track of red stars (sources), but this is not the case in practice. The largest location error due to feathering occurring at the last receiver, is up to $\sim$ 1.5 km in 3D.

As only a 2D model is available and I invert the wavefield in 2D, the positions of the receivers need to be corrected onto a straight line. The examination of the receiver positions revealed a marginally larger receiver sampling. For most lines, accumulated inline position errors for all receivers were up to 100 m when assuming a constant grid distance 12.5 m. Therefore, especially far offsets need to be interpreted carefully.
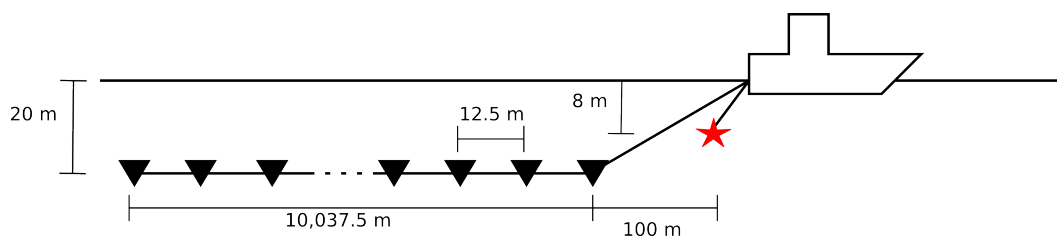
Figure 3.8: Sketch of the acquisition geometry with the source as red star and the receiver as black triangles.
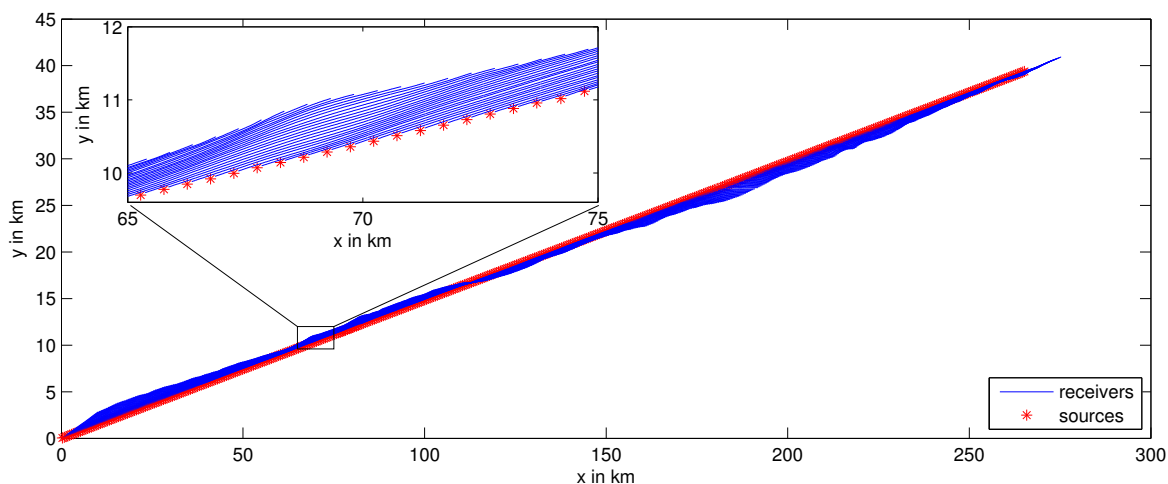
Figure 3.9: Plot of every 10th shot with the corresponding receivers showing the streamer feathering. The vessel was moving from right to left side. In the upper left corner, a zoom is shown.

3.3.2 Recording

The recording length is 15 s with a sampling interval of 2 ms. This results in 7501 samples per trace and 6.03 million samples per shot. In figure 3.10 an exemplary shot is plotted. The direct wave appears very broad in the beginning. This is an effect of the wavefield separation

applied to the data. This technique considers only waves travelling vertically, which is why the direct wave is distorted.

The first reflection from the sea bottom appears at about 4.1 s. The reflection from the salt surface is following directly after it. At about 8.2 s at the near offsets, the first-order water bottom multiple emerges. Also, refracted waves are visible at around 5 s at offsets > 7000 m. The signals prior to the first arrivals are muted. In general, the signal-to-noise ratio appears sufficient for inversion.
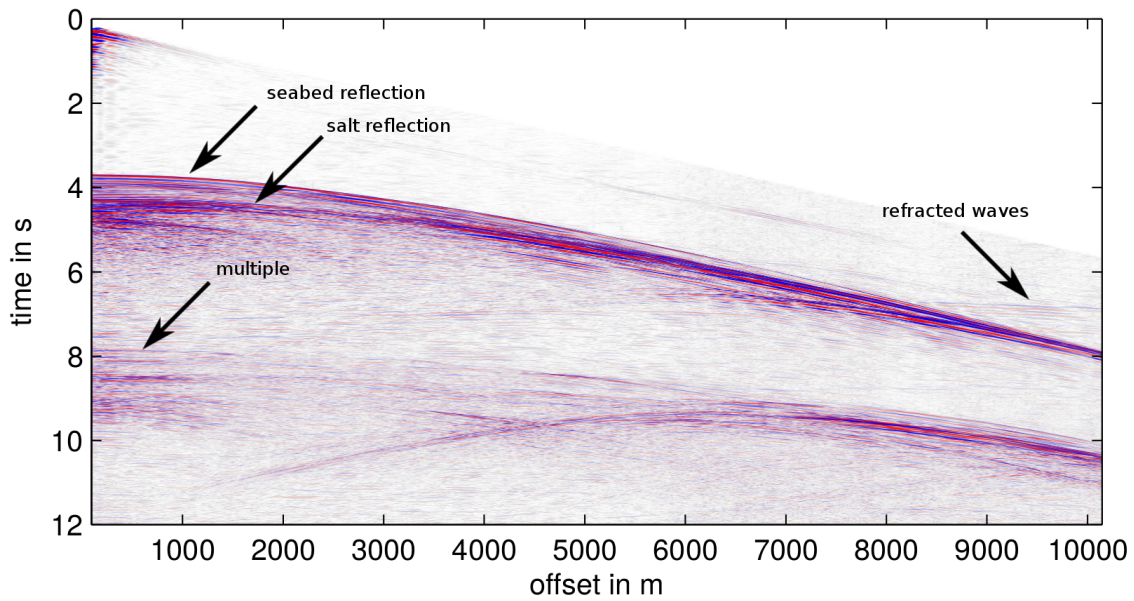
Figure 3.10: Exemplary shot of the field data (shot 61), showing the distorted direct wave and the strong reflections from the water bottom and top salt.

3.3.3 Frequency content

The data were requested as raw as possible. Therefore, no advanced filters were applied on the data, only a 2 Hz high-pass filter to suppress the swell noise. In order to analyse the frequency content of the raw shots, a conventional Fourier transformation was applied to the representative shot shown in figure 3.10. The average of all traces of the frequency spectrum can be seen in figure 3.11a. The amplitudes are normalised to the global maximum. A peak in the spectral amplitudes can be observed between $6 - 10$ Hz as well as the almost linear descending amplitude from a value of 0.5 at about 10 Hz to a value of 0.1 at 80 Hz. By taking a closer look into the $1 - 30$ Hz range (figure 3.11b) it can be seen that the normalised spectral amplitude passes 0.1 at around $2 - 3$ Hz and reaches 20 % at about 5 Hz. After this point, the amplitude is ascending fast to 1 at about 7 Hz. This means that very little information is present in the data below 5 Hz for the inversion. Small local minima at about 12 Hz and 20 Hz are visible. These notches are not related to the receiver ghost, which would appear at 37.5 Hz or a multiple of it.

(a) Frequency window from 0-100 Hz. **(b)** Frequency window from 0-30 Hz.
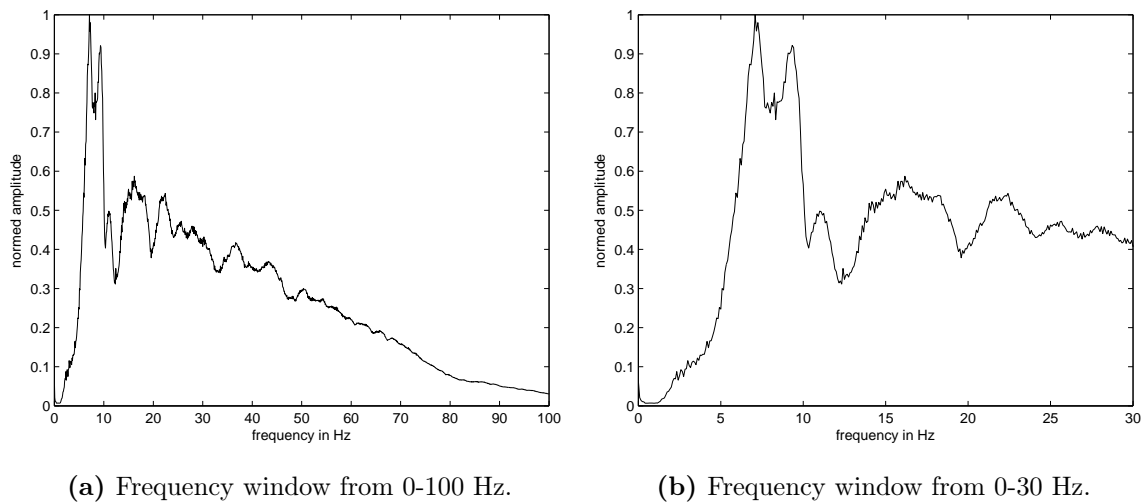
Figure 3.11: Frequency content of the field data. Averaged frequency spectra over all offsets for one exemplary shot.

To analyse the frequency content in the data domain an exemplary shot gather was filtered with different cosine-tapered low-pass filters, similar to the taper shown in figure 2.3. The titles in figures 3.12 state the start and end frequencies of the down-slope of the filter. In figure 3.12a it can be observed that the data below 4 Hz (or below 0.1 on the normalised amplitude scale) contain almost no visible signals. Starting from the next frequency panel using a low-pass filter with corner frequencies of 4-8 Hz low-frequent data appear. Only in the next panel, where the data were filtered by a low-pass filter with the two corner frequencies of 8 Hz and 16 Hz, most of the data become visible. Figure 3.12b shows that now most of the first broad peak in the frequency spectrum is included in the data. The black area represents the filtered spectrum.

In figure 3.13a the single traces of shot 61 were transformed to the frequency domain. The red colour mark areas of high amplitude, located at the middle offsets. Between 5 Hz and 10 Hz is a maximum, as we already observed in figure 3.11. Figure 3.13b shows the Fourier transformation in two dimensions, giving us a frequency-wavenumber (FK) spectrum. Due to the streamer geometry, most waves reach the streamer from the source direction and only very little energy is coming from the opposite direction (e.g., due to reflection). The FK domain is used for the wavefield separation. Before transforming the shot gather to the FK domain, the direct wave was muted as the strongly modified direct wave leads to high amplitude artefacts in the spectrum after the wavefield separation.

For the inversion the maximum usable frequency was calculated to be 14 Hz (equation 2.10) using 12.5 m spatial sampling (section 3.2) and n=8 (4th order FD operator). The maximum frequency is clearly below the location of the first notch in the frequency spectrum resulting from the receiver ghost. However, the wavefield separation performed by PGS manipulated all field data. Therefore, the application of wavefield separation is still necessary for FWI.
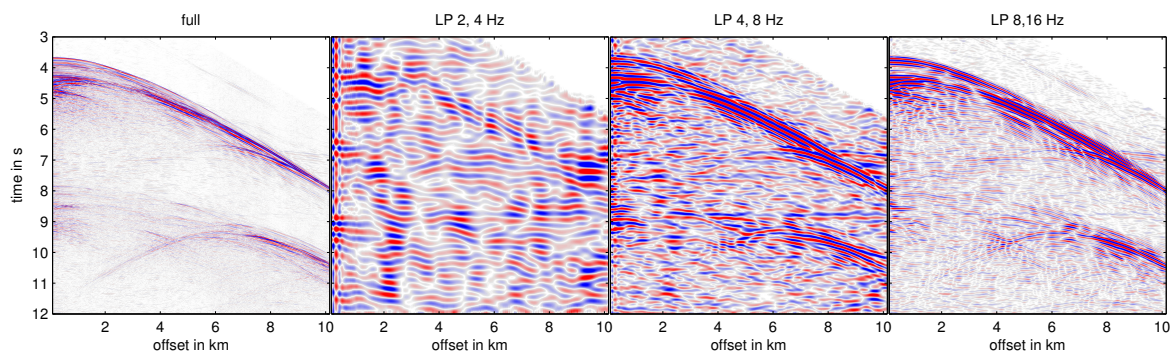
(a) Filtered data in the time domain for different low-pass filters. The data were normalised to the maximum amplitude of the first trace.
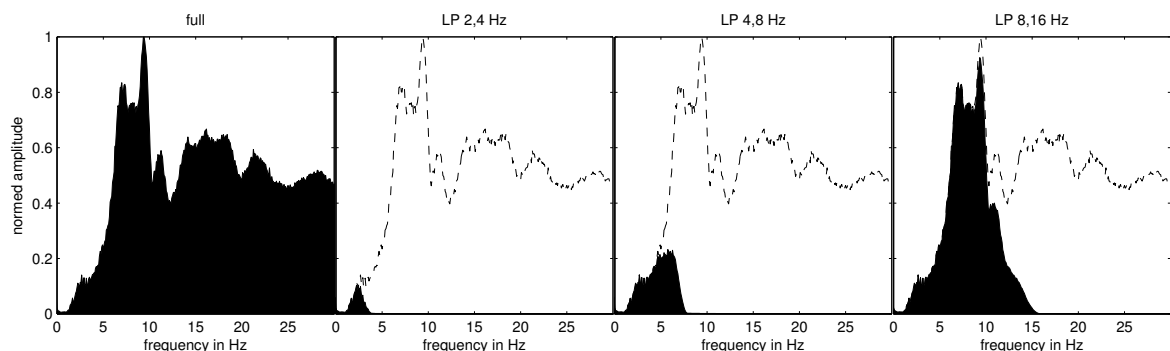
(b) Frequency content of the low-pass filtered data (black area) in comparison to the full frequency content (dashed line).

Figure 3.12: Exemplary shot gather (shot 61) in the time and frequency domain filtered with different corner frequencies. The data was filtered with a cosine-taper low-pass filter, similar to the taper shown in figure 2.3. The start and end frequency of the down-slope of the filter are given in the titles of the plots.
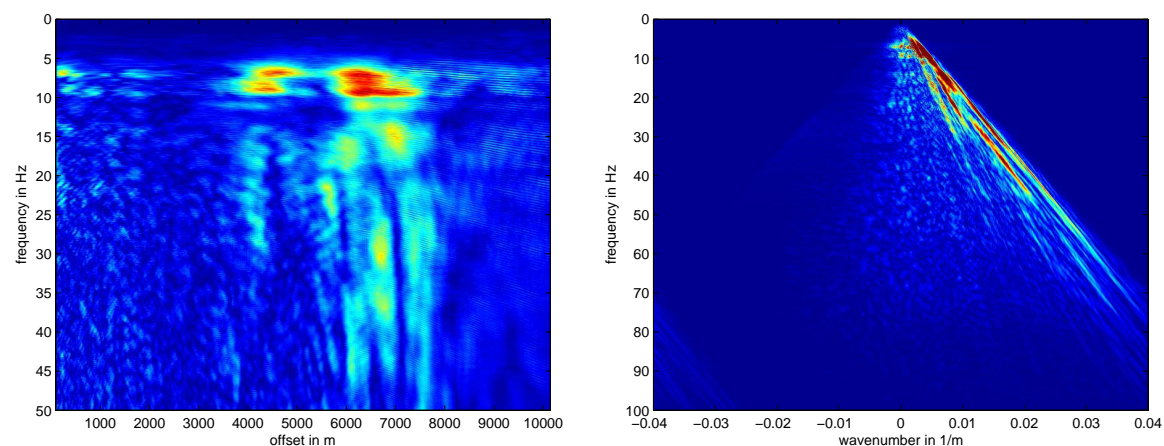
(a) Frequency vs. offset. No energy is visible for frequencies below 5 Hz. Most energy is visible between 5 and 10 Hz.

(b) FK spectrum showing most energy for positive wavenumbers, typical for a marine acquisition geometry.

Figure 3.13: Frequency content of the field data.

3.3.4   Wave types

For a good configuration of an FWI workflow and the examination and evaluation of the results, the data need to be known as best as possible. The last section analysed the data in the frequency domain, now the shot domain will be examined. Therefore, this section studies the existence of different wave types and their importance for FWI.

Diving waves

Diving waves occur in models with a depth-dependent gradient where the velocity increases with depth. Due to Snell's law, the rays travelling downwards are bent upwards again. If the gradient is weak, the diving waves need a large horizontal distance to appear again at the surface. For this case, long offsets are needed to be able to record the diving waves. As the diving waves contain long wavelength information (e.g., Zhou et al., 2015; Chazalnoel et al., 2017), they are essential for successful FWI.

By examining the PGS model (figure 3.6), the most prominent part in the subsurface is the salt body. The thickness extends to more than 2 km depth, and at the boundaries of the salt large impedance contrasts occur. The salt body itself consists typically of more or less homogeneous material with constant velocity. Therefore, no diving waves can occur in the salt body. In addition, the sediment layer above the salt is very thin. This reduces the occurrence of diving waves further. Also, the water is more than 3 km deep in parts of the model. This leads to the fact that first diving waves occur at 30 km offset. This effect can also be seen in figure 3.14. Almost no ray paths are bent back to the surface. With the given geological environment and the given acquisition geometry, no diving waves can be expected.

Refracted waves

The alternative for diving waves pertaining to the low wavenumbers are refracted waves. Refracted waves occur if a ray encounters an interface at the critical angle. At this angle, the ray is transmitted with 90° to the perpendicular of the interface into the second medium. The refracted ray travels with the velocity of the second layer along the interface and continuously emits energy to the surface (head wave).

For the water-sediment interface, Snell's law gives a critical angle of about 50°. For 3 km deep water and the calculated critical angle, the first refracted waves can be recorded by receivers with 7 km offset, at least for a flat sea floor. By looking at the shot gathers the offset, where the refracted waves should start to occur can be confirmed. The refracted waves are strongly influenced by the topography of the interface. In figure 3.15 three exemplary shots are displayed. Some shots contain refracted waves, for example shot 101, other shots do not contain any refracted waves. It also happens that the refracted waves are covered partly by diffractions (e.g., shot 5). This makes it hard to use the refracted waves for FWI, especially when using a starting model with deficiencies in the main structures.
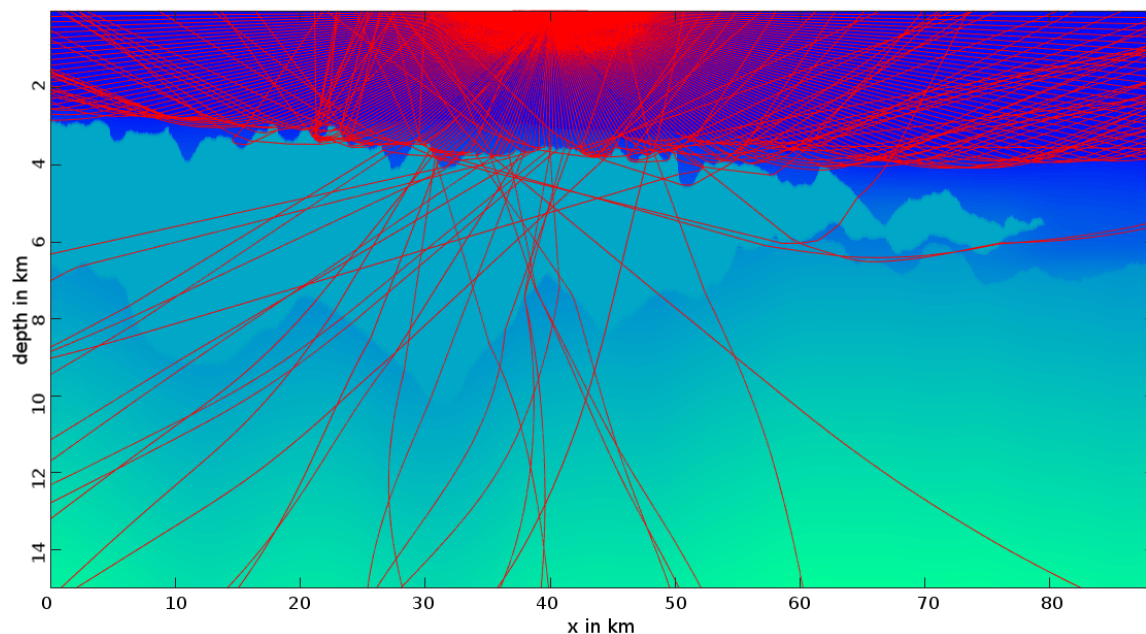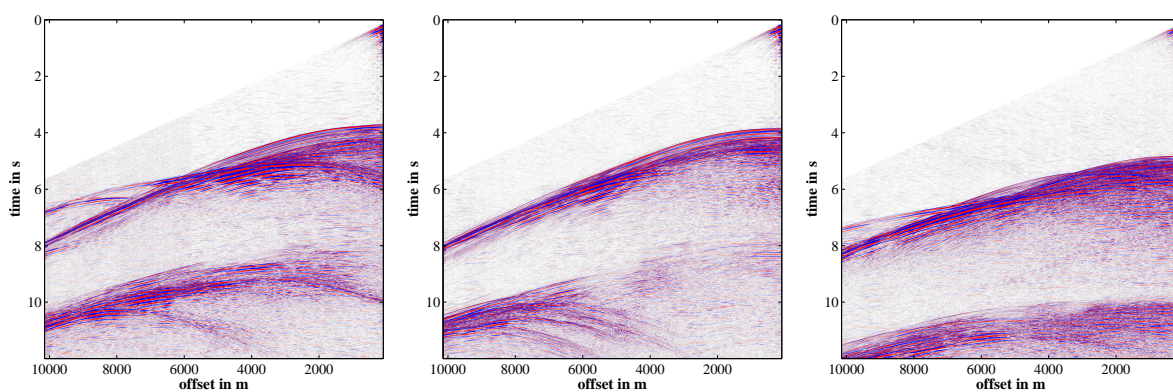
Figure 3.14: Ray tracing in model 2. The source was located at the surface at x=40 km. Most rays travelling back to the surface are reflected or refracted waves. No rays are reflected back from the bottom salt line.

(a) Shot 5, showing refracted waves covered partly by diffractions.

(b) Shot 40, showing data with no refracted waves at all.

(c) Shot 101, showing well defined refracted waves.

Figure 3.15: Exemplary shots of the field data, showing the varying appearance of refracted waves.

Diffracted waves

Multiple diffracted waves are visible in the data. By simulating the full wavefield, the source of the diffractions could be backtracked to the topography of the sea floor and top salt. If the wavefront hits a valley, it is partly diffracted at sharper edges of the valley. In figure 3.16 the diffracted wave is generated at the upper left edge of the valley in the seabed below the source location. After 4.9 s the diffraction occurs as a second wavefront at the left part of the first reflection.

The diffractions can produce difficulties during FWI. If the starting model cannot explain the diffractions, parts of the data with high amplitudes cannot be explained during inversion. FWI might compensate this problem by inserting artefacts in the model.

Reflected waves

The seismograms are dominated by reflections, common for marine data. The disadvantage of reflections is the large high-frequency content and, therefore, the high dependency on the model quality (e.g., Sun et al., 2016). The starting model needs to explain the data kinematically sufficiently well. Shallow reflections are heavily influenced by local structures, for example in my case a high-velocity layer in the shallow sediments. In addition, the low impedance contrasts at the salt bottom interface result in no visible reflections from this area at 6-9 km depth (see figure 3.14). Thus, successful subsalt imaging with FWI relies on a shallow subsurface model as exact as possible in order to adapt waveforms from deeper parts of the model.

All in all it can be said that the data are dominated by reflection waves partly covered by diffractions. The wave types containing the low-frequency component, such as diving waves or refracted waves, do not exist in the data or they are just partly visible. As the low frequencies are important to build up a low wavenumber starting model and prevent the occurrence of cycle-skipping, the demands on the quality of the starting model are very high.

3.4 Preprocessing

The data were delivered with little processing applied. PGS only applied a high-pass filter of 2 Hz, a swell noise attenuation and a linear noise attenuation. Furthermore, the data were already wavefield separated. PGS delivered the data in SEG-Y standard format. For further processing with Seismic Unix and, in order to make the data usable as input for IFOS2D, the data were converted to Seismic Unix (SU) format using the SU program *segyread*. After the transformation, some preprocessing steps (explained in this section) were necessary before the data could be used for FWI. In general, only very few preprocessing steps are necessary for FWI in comparison to other imaging techniques, where for example the multiple waves need to be removed. But in FWI, most effects that occur during wave propagation are taken
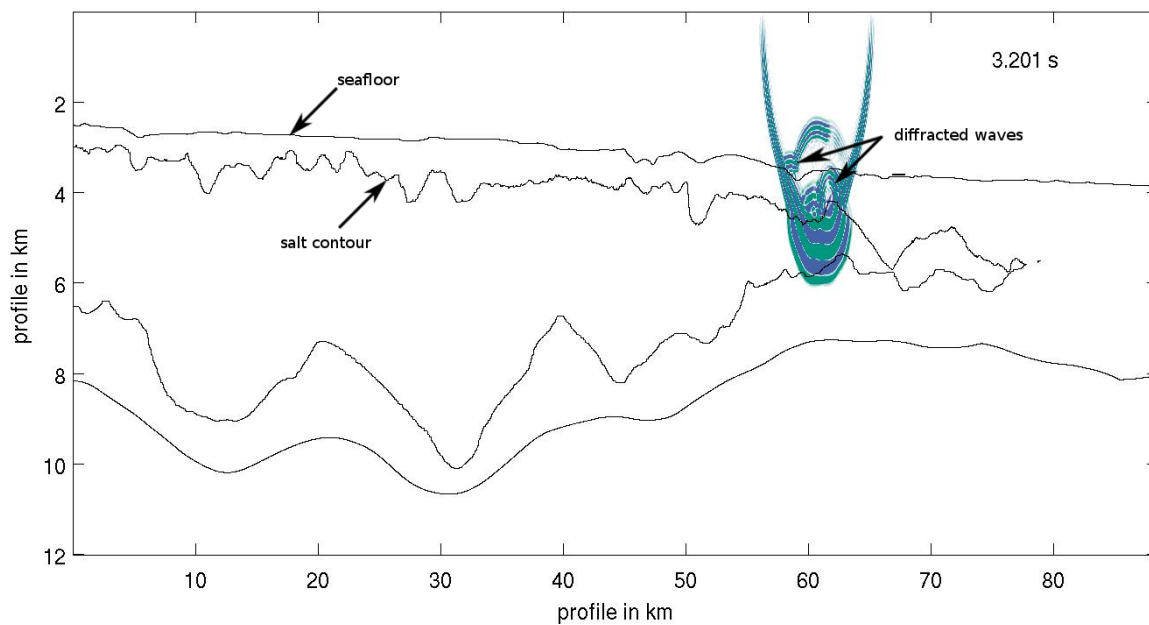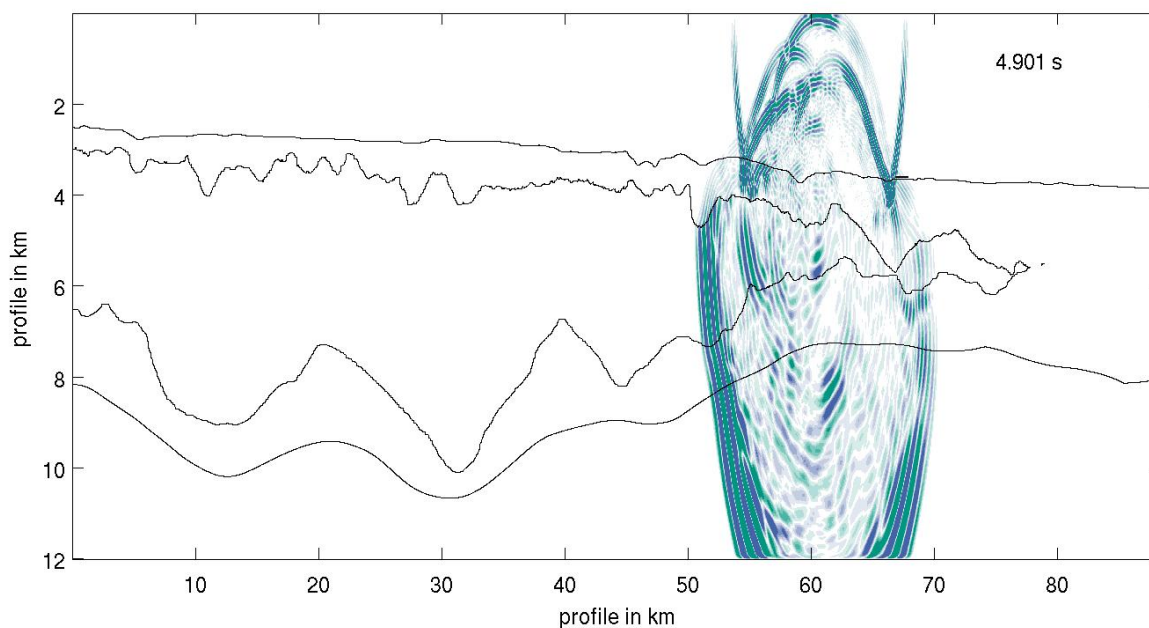
(a) Snapshot at $t = 3.2$ s.

(b) Snapshot at $t = 4.9$ s.

Figure 3.16: Snapshots of the pressure wavefield during acoustic forward modelling. Contour lines for the sea floor and salt body are plotted for better orientation. The line below the salt body represents the location where the vertical velocity gradient of the sediments reach salt velocity.

into account and, therefore, do not have to be removed. The applied preprocessing steps are explained in the following sections.

3.4.1 Resampling

In order to ensure a stable simulation of the wavefield, the Courant-Friederichs-Lewy criterion needs to be fulfilled (section 2.1.2). With a sampling in space of 12.5 m (see section 3.2) and a maximum P-wave velocity of about 6000 $\frac{\text{m}}{\text{s}}$, the time sampling dt has to be smaller than 1.5 ms with second-order FD operators, or even smaller with higher order operators (equation 2.11). To ensure a stable simulation I decided to use a 1.2 ms time sampling interval. A smaller sampling interval would increase the size of the data even more and, therefore, the required disk space and memory during the inversion. The resampling was done using the SU program *suresamp*.

3.4.2 Correction of delay time

In the original field data all seismic traces were shifted up by 0.1 s. For the application of FWI all shot gathers needed to be padded with zeros in front of all traces in order to shift them in the correct position. This is necessary to ensure the comparability of the modelled seismograms and the field data. Setting of *delrt* in the header was not an option, as IFOS2D is not able to use any header values.

3.4.3 3D-2D transformation

FWI in three dimensions is extremely expensive in terms of time and memory requirements. Therefore, and due to the fact that the profile was acquired along a straight line, the inversion and modelling was performed in 2D. As the field acquisition took place in 3D, the field data were corrected as explained in the following in order to make them comparable to the modelled data (Auer et al., 2013). The line-source simulating (*lisousi*) software of Thomas Forbriger was used to apply two corrections on the data (Forbriger et al., 2014). The first is a scaling of the amplitudes with the factor $\sqrt{t}$. It compensates the geometrical spreading effect. In the field measurements, the energy is distributed on a 3D-wavefront, whereas in the modelling only a 2D wavefront exists. The second adjustment, a phase correction, is applied by convolving all traces with $1/\sqrt{t}$ (Pica et al., 1990).

3.4.4 Data selection for FWI

Shots

For inversion, the shot spacing of 50 m was enlarged to 500 m in order to reduce computational costs. Therefore, only every 10th shot was used. The shot positions with the new shot distance

were defined on the equidistant model with 12.5 m grid spacing (see chapter 3.2). To find the correct shots for the defined source positions in the model, a *MATLAB* routine was written. By using the shot coordinates in the headers of the data and model, the shot nearest to the defined shot position in the model was selected. Thus, a maximum error of 25 m (two samples) in x-direction was accepted, as it is far below the minimum wavelength.

In most FWI tests in the following I will concentrate on the area of model 2. Therefore, only the shots fitting this limited profile including all receivers were used. For model 2, the shot selection reduces the number of shots to 155; for model 3 only 19 shots were used.

Time window

As the model depth was reduced to 12 km (see chapter 3.2), the data were also reduced from 15 s recording time to 12 s. The shortening of the data was performed with the SU program *suwind*.

For all inversion processes the direct wave could not be used due to the wavefield separation (compare chapter 2.4.2). Therefore, an additional time window was applied in IFOS2D to all shots, using only the data after the direct wave, beginning at the first reflection of the seabed. The muting times for all shots were picked in *MATLAB* by using the non-filtered seismograms. Ten to twelve picks per shot were set by hand about 0.1 s before the first arrival. After picking, the picked times were interpolated to get a list of mute times for all traces of the given shot. The interpolation was done by using the 1D interpolation *interp1* in *MATLAB* with the interpolation method *pchip*, a shape-preserving piecewise cubic interpolation.

To reduce the number of picks, only every second shot was picked. As the water depth is increasing with the shot number, also the time of the first reflection increases with the shot number. This allows the usage of the mute function of the previous shot for the intermediate shots. The continuously increasing time of the arrivals of the first reflection prevents that the picked times from the previous shot cross the first arrivals of the intermediate shots. For quality control all shots (also the intermediate shots) were plotted, including the interpolated picks, and checked visually. In figure 3.17 the data used for FWI are shown in the yellow shaded area. It includes all data, except the direct wave, visible in figure 3.17 at about 0.2-1 s only at the first few traces due to trace normalised amplitudes.

During the FWI flooding workflow the size of the yellow shaded area can be varied. The deeper the target of the inversion, the more time or offsets of the data are used.
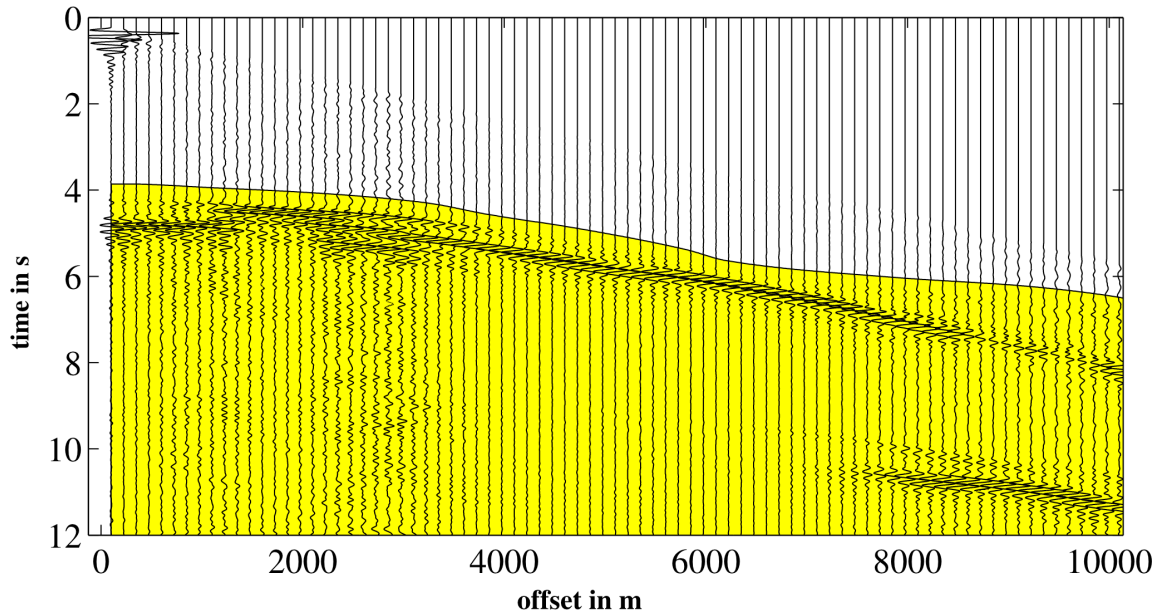
Figure 3.17: Data windowing for removing the direct wave. The yellow shaded area of the data is used for FWI.

3.5 Summary

This chapter introduced the geological environment in which the data were acquired, the provided subsurface model and the field data set. The geological evolution in this region produced a complex environment. The subsurface includes a salt layer with strong topography and sediments including a velocity/density-layer representing a strong reflector. With this knowledge, a complex wavefield is expected.

The data consist mainly of reflections. Due to the deep water and only thin sediments above the salt, no diving waves and only a few refracted waves were recorded. As no usable information is included in the data below $4-5$ Hz, FWI requires a sufficiently accurate starting model, able to explain the main low-frequency features of the data.

After applying a few necessary preprocessing steps explained in the last section, the next chapter will start with synthetic tests to become even more familiar with the model and the acquisition geometry.

Chapter 4

Synthetic inversion tests

Prior to the field data inversion, I conducted several synthetic inversion tests. For a given model, assumed to be the true one, the propagation of waves produced by a source is simulated. The wavefield is recorded at the given receiver points and treated as acquired data for the following FWI process. The synthetic tests are important to investigate the practicability and applicability of the inversion workflow. By using the same acquisition geometry as used for the field data, I can study illumination limits induced by the combination of the given acquisition geometry and subsurface structures. As the true model is known, the influence of certain parameters on the reconstruction of the model can be investigated.

The first section provides an introduction to the resolution test used in this chapter (section 4.1). In section 4.2, the resolution test is used to examine the influence of wavefield separation on the data and, therefore, on the success of FWI using only the upgoing part of the wavefield. In order to allow a good interpretation of the inversion results, I started with a simple 2-layer model and a simple acquisition geometry. Before using the PGS model for the resolution tests shown in section 4.5, I introduce the model and acquisition geometry in section 4.3 and the main modelling and inversion parameters in section 4.4. Section 4.6 introduces the flooding technique and the successful reconstruction of the top of salt (TOS) and the bottom of salt (BOS).

4.1 Resolution test method

A chequerboard test is a common method (e.g., Lévěque et al., 1993; Morgan et al., 2013; Butzer et al., 2013) which helps to become familiar with the model. For a given model, acquisition geometry and frequency content, the result of this resolution test reveals areas with insufficient illumination. Therefore, this method shows if the given setup is sufficient to invert structures in the target area of the model. The chequerboard test is a pure synthetic FWI test. A model is perturbed with a chequerboard pattern and used to generate the synthetic field data. In my case, the resolution tests were limited to the v_P model in order to keep the test as simple as possible. Therefore, only the true v_P model was perturbed, the

true density model was kept as is. For the same reason, the inversions were performed in the acoustic approximation. In all resolution tests, I set the perturbation to ± 2 % of velocity in the model to be perturbed. In salt, the perturbation corresponds to ± 80 $\frac{m}{s}$, in sediments only about half of it. Using the true perturbed model, a forward modelling for all shots is performed, resulting in a data set pretending to be the true one for the following inversion.

For the acoustic inversion the true model without the perturbations is used as starting model. The quality of the reconstructed chequerboard pattern in the inversion result can vary strongly and depends on the illumination. The illumination is mainly influenced by the model composition and the used acquisition geometry. Furthermore, the frequency content used for the inversion does control the resolution of the chequerboard pattern. Therefore, the selection of the size of the squares is important to correlate with the used frequencies. I set the edge length to 80 m in both dimensions. For the shallow part (2000 $\frac{m}{s}$) and low frequencies (2-5 Hz) the edge length is equal to about one fifths of the averaged wavelength of 400 m in the given area and frequency range. For a maximum frequency of 10 Hz, the wavelength is reduced to 200 m. As the inversion is able to image structures far below the wavelength, I expect a reconstruction of the chequerboard pattern in the model with a slightly smoothed area between the squares.

4.2   Influence of wavefield separation on FWI

In general, several approximations in FWI are widely used, e.g., the acoustic approximation or the assumption of an isotropic medium. Depending on the medium, FWI can still produce successful results despite the neglect of parameters. If the influence of a unconsidered parameter on the data is high it becomes necessary to include the parameter in the FWI workflow. In order to test the influence of the wavefield separation on the wavefield and, therefore, on the inversion result, I performed some synthetic tests, described in this section.

The model used for the tests is a simple 2-layer model, shown in figure 4.1. The background model consists of a 1 km thick horizontal layer of $v_P = 1500$ $\frac{m}{s}$. Below, a second layer with $v_P = 2000$ $\frac{m}{s}$ is located, also with 1 km thickness. In total, the model covers 2 km in depth-direction and 10 km in x-direction. The spatial sampling is 1.25 m to allow the usage of higher frequencies. The sources and receivers are distributed equally below the surface of the model in 16 m depth. 19 sources and 721 receivers are used. Every shot uses all receivers. The model and acquisition geometry is kept simple by purpose in order to exclude as many effects as possible based on the model and acquisition geometry.

The velocity perturbations in a chequerboard pattern start at a depth of 500 m and includes the whole area underneath. The velocity perturbations are ± 2 % of the background model (see section 4.1). The starting model is the true model without the velocity perturbations. The squares of the chequerboard pattern have a size of 80×80 m. Using a $2 - 5$ Hz frequency range for inversion, the size of the chequerboard squares is about one fourth of the minimum wavelength (300 m to 400 m).
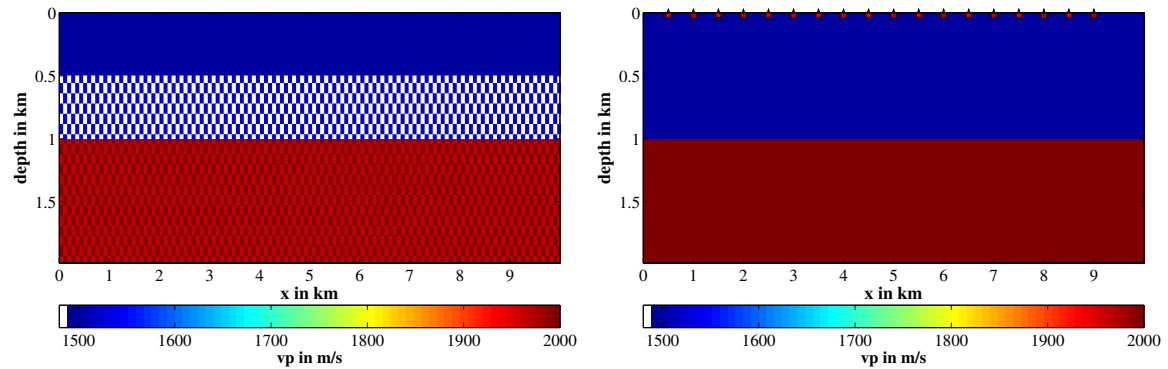
(a) True model including perturbations in a chequerboard pattern of ± 2 % of the background model.

(b) Starting model without perturbations.

Figure 4.1: Simple 2-layer model for a wavefield separation test.

To create a reference inversion result, the first inversion was calculated using no wavefield separation, neither in the forward modelling using the true model nor during the inversion. The result after 30 iterations is shown in figure 4.2a. The chequerboard pattern is clearly visible over the complete depth range. Only the borders could not be resolved well due to bad illumination in this area. By looking at the profile shown in figure 4.2b, located at $x = 5$ km, the very good resolution of the pattern can be observed. Above the step in the velocity, the inversion was able to reconstruct the chequerboard pattern almost perfectly. The perturbations are located in the correct position and, also, the absolute values of the chequerboard patterns could be reconstructed perfectly. Due to the lack of high frequencies in the data, the corners of the squares are slightly rounded. Below the velocity step, the inversion was also able to reconstruct the perturbations in the correct position. Only a little loss in resolution can be observed compared to the inversion result in the upper layer. The lower resolution occurs due to the longer wavelength (higher velocity) in this layer. A second reason is that the amplitudes in the data produced by structures in the second layer are lower, compared to events from the first layer. This is caused by a high reflectivity at the layer interface, why only a part of the energy is transmitted. In consequence, the inversion will produce stronger updates in the first layer than in the second layer. Also the interleave-plot in figure 4.3b shows a very good data fit. Almost no differences of the synthetic and field data can be observed. Figure 4.3a shows the total update after the last iteration. In this plot, the limited illumination and, therefore, the limited update in the corners is visible. On the other hand, the very good update in the centre can also be observed.

For the second test I performed the same forward modelling to get the true data and, in addition, applied the wavefield separation on the modelled data. The following inversion was performed using no wavefield separation, to show the influence of the wavefield separation on the inversion result. The differences between the original data and the wavefield separated data are so large that the inversion is not able to reconstruct the chequerboard pattern (figure 4.2c and figure 4.3c). Only the horizontal and vertical artefacts of the sources and receivers are visible as well as artefacts at the velocity step. Also, in the profile (figure 4.2d)

the overshoots and undershoots at the step and the low velocity artefacts at the source and receiver positions are present. In the interleave plot shown in figure 4.3d, the large differences are visible. The direct wave and main reflections are in the correct position as expected, as they already exist in the starting model. But almost no features of the chequerboard pattern, visible as ripples in the data between the main reflections, could be fitted. Due to the wavefield separation, the wavelet changed and some horizontal artefacts occur at about 0.2 s and 1.5 s. Especially the direct wave is highly modified by artefacts or partly distorted. Since the high-amplitude artefacts cannot be fitted by the inversion, the lower amplitude features generated by the chequerboard pattern have no influence on the updates inside FWI.

In the third test I used the wavefield separated forward modelled data set and performed an inversion workflow, where the wavefield separation is performed after every forward modelling. The results are shown in figure 4.2e-4.2f and figure 4.3e-4.3f. All plots show a great similarity with the results of the first test using no wavefield separation at all. The profile shows only a very small lower absolute amplitude in the second layer.

These three tests show the great potential of FWI and the necessity of including the wavefield separation in FWI when using wavefield separated data. The wavefield separation cannot be neglected. In this test, the very same wavefield separation was used for generating the true data and for FWI. As the exact parameters used for the wavefield separation performed by PGS on the field data are not known in detail, I decided to mute the direct wave, as this is the part of the shot gather mostly distorted by the wavefield separation. As second action the usage of a source time function (STF) inversion is recommended. As the wavefield separation changes the appearance of the waveforms, the STF inversion can compensate small differences in the waveforms of the field data and synthetic data generated by the wavefield separation.

4.3   Model and acquisition parameters

In order to make the seismograms of the modelled data and field data comparable, the acquisition geometry of the forward modelling needs to represent the field data acquisition as best as possible. I used a constant source depth of 8 m, following the field acquisition. This value was set in the input file. The program automatically changes the position to the next grid point (in this case 12.5 m), accepting a maximal location error of half a grid point. The same applies for the receiver depth. The original receiver depth of 22 m was changed to the next grid point of 25 m below the free surface. For every shot 804 pressure and velocity receivers were used with a spacing of one grid point (12.5 m) in x-direction.

For the synthetic tests I increased the shot distance from 50 m to 500 m. This allowed me faster testing and avoided a lot of data output. As mentioned in the previous chapter, the synthetic tests focus mostly on an 88.5 km-long and 12 km-deep subarea of the model (model 2). With a constant grid distance of 12.5 m this results in $7080 \times 960 \approx 6.8$ million grid points. As source wavelet a $\sin^3$ wavelet was used with a main frequency of 7 Hz. All parameters are summarised in table 4.1.
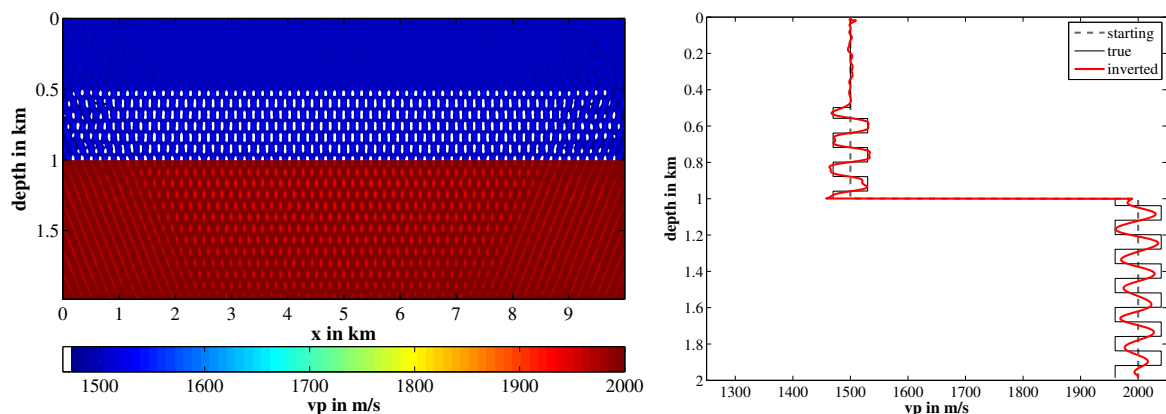
(a) v_P model after the inversion using no wavefield separation at all.

(b) v_P profile of the inversion result at $x = 5$ km using no wavefield separation at all.
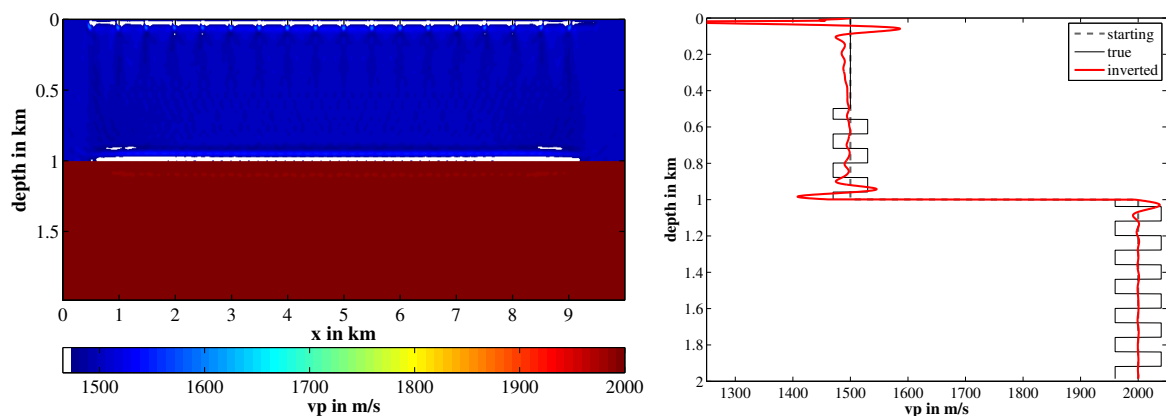
(c) v_P model of the inversion with applied wavefield separation on the true data.

(d) v_P profile of the inversion located at $x = 5$ km with applied wavefield separation only on the true data.
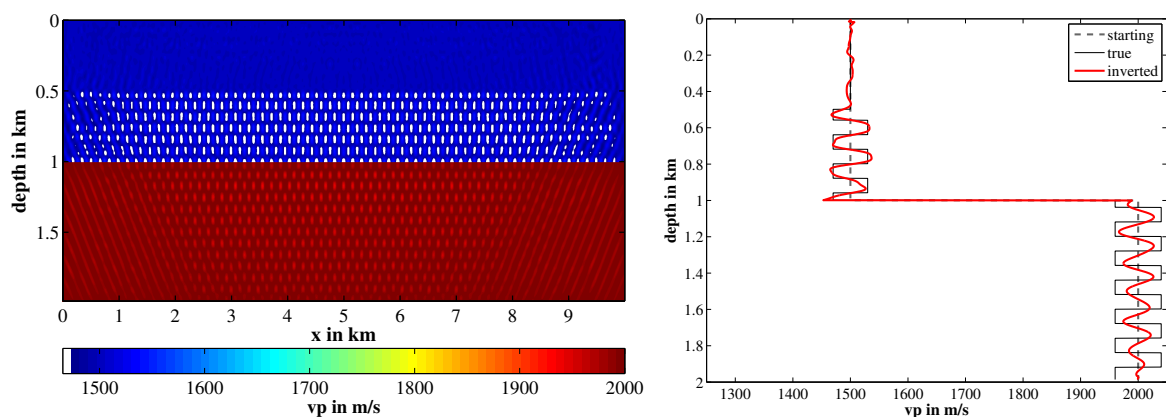
(e) v_P model of the inversion with applied wavefield separation on true data and inversion.

(f) v_P profile of the inversion located at $x = 5$ km with applied wavefield separation on the true data and synthetic data.

Figure 4.2: Inversion results of the resolution test with and without wavefield separation after 30 iterations using the models shown in figure 4.1 (v_P-model and profile).

(a) Difference plot (starting model minus inverted model) using no wavefield separation at all.

(b) Interleave plot of true data (red/blue) and inverted data (green/blue) using no wavefield separation at all.

(c) Difference plot (starting model minus inverted model) using wavefield separation only for the true data.

(d) Interleave plot of true data (red/blue) and inverted data (green/blue) using wavefield separation only for the true data.

(e) Difference plot (starting model minus inverted model) using wavefield separation for the true data and the inversion.

(f) Interleave plot of true data (red/blue) and inverted data (green/blue) using wavefield separation for the true data and the inversion.

Figure 4.3: Inversion results of the resolution test with and without wavefield separation after 30 iterations using models shown in figure 4.1 (data and difference plot).

In the previous version of the IFOS2D code it was necessary to store seismograms for all possible receiver positions from all shots. For my moving streamer geometry, this results in 6803 traces instead of the 804 traces of the streamer. Using 12 000 time samples, this produces a file size of about 300 MB for each shot gather. For memory reasons I reprogrammed the implementation of the receiver positioning. With this new implementation the number of traces is equal the number of receivers per shot. For every shot the receiver positions are recalculated. For the model explained above, the memory footprint decreases by a factor of about 8.5 for the shot gathers.

Table 4.1: Model and acquisition parameters for the synthetic tests. The values in brackets are the positions on the grid modified by the code used for the modelling.

Parameter	Value
Grid size	$7080 \times 960 = 6.7968 \cdot 10^6$
Grid spacing	12.5 m
Time sampling	1 ms
Record length	12 s
Number of time samples	12 000
Source wavelet	$\sin^3$
Frequency range	3 - 14 Hz
Number of shots	155
Shot spacing	500 m
Shot depth	8 m (12.5 m)
Number of receivers	804
Receiver spacing	12.5 m
Receiver depth	22 m (25 m)
Offsets	100 - 10 138 m

4.4 Modelling and inversion parameters

Before starting the FWI process, several parameters have to be set in the input file controlling the inversion process. One of these parameters is the order of the FD operator. As mentioned in section 2.1.2, the higher the FD order, the lower the grid sampling and time discretisation requirements need to be. On the other hand, experience shows that a higher FD order in combination with high-velocity contrasts cause instabilities during the propagation of the wavefields. For acoustic FWI I successfully tested an FD order of six. In the following chapters, also the results of elastic modelling and inversion are shown. In the shear-wave models, higher velocity contrasts occur than in the P-wave models, for example at the sea floor. Therefore, the FD order needed to be reduced to two for the elastic inversion.

The data were delivered as pressure data. Therefore, the receivers in the modelling also record pressure data. In addition, to be able to perform the wavefield separation, the vertical velocity is written out. The code is able to perform the modelling in different parametrisations. The

user can choose between Lamé parameter, seismic impedances or seismic velocities and density. I used the seismic velocities and density to ensure that no transformations are necessary between input, calculation of the wavefield separation and output.

For calculating the gradient the preconditioned gradient (PCG) method is used. It proved to have robust convergence in combination with high stability. The gradients are preconditioned by using the approximated Hessian matrix after Plessix and Mulder (2004). In my case, the approximated Hessian is calculated for all shots individually and applied directly on every single gradient before the summation of the total gradient. As objective function, I chose the L_2-norm in the trace-normalised version (see section 2.2.2).

The source time function inversion is an essential part in FWI. In this work I use a frequency-domain least-square implementation including a taper, as specified in section 2.3. For the frequency filtering of the data a Butterworth filter of 4th order was used. All data were filtered with a 2 Hz high-pass filter. In addition, the data were filtered with a low-pass filter according to the actual frequency band. I chose a minimum number of iterations per frequency band of eight. That means the inversion is forced to stay in the frequency band for at least 8 iterations, even if the criteria for a frequency change are reached earlier. This was chosen from experience to prevent the inversion from moving to the next frequency band too early, as is often observed.

The inversion parameters are summarised in table 4.2. All inversions were conducted using these parameters unless stated otherwise.

Table 4.2: Inversion parameters for synthetic and field data FWI.

Parameter	Value
FD order	6 (2 in elastic FWI)
Receiver	pressure
Parametrisation	seismic velocities and density
Preconditioning	approximated Hessian after Plessix and Mulder (2004) applied to each shot directly
Gradient	preconditioned conjugate gradient method (PCG)
Objective function	L_2-norm trace-normalised
Source time function inversion	frequency-domain least-squared, tapered
Frequency filtering	Butterworth filter with 4th order: low-pass fixed at 2 Hz, high-pass increased in 1 Hz steps starting from 5 Hz
Minimum number of iterations per frequency band	8

4.5   Resolution test for the PGS model

In general, before starting with an actual inversion, it is recommended to perform a resolution test in order to become familiar with the model and test the limits of the acquisition

geometry. For this purpose, I applied the chequerboard test as described in section 4.1. I applied the velocity perturbations of ± 2 % to the 88.5 km-long subpart of the PGS model (figure 4.4b). A forward modelling was performed on this perturbed model. The recorded synthetic data set was used as reference data set for the following FWI. As starting model I used the non-perturbed model (figure 4.4a). For the first iterations the data were bandpass-filtered using frequencies between 2-6 Hz. The inversion increased the frequency bandwidth after 10 iterations to 2-10 Hz. This large step in the frequency bandwidth is possible only in the synthetic case (see section 2.2.7). For the inversion of field data, smaller steps need to be used. The change in the frequency band is shown in figure 4.4e with a red dashed line.

The result after 30 iterations is displayed in figure 4.4c. The perturbation pattern could be resolved very well. Only the edges are not as sharp as in the true model, due to a maximum frequency of 10 Hz in the inversion. The lack of high frequencies limits the resolution. The profile in figure 4.4f illustrates that the perturbations are located in the correct place and also the absolute values are almost correct. By taking a closer look at the difference plot in figure 4.4d it can be observed that the update was performed equally in the whole model, except near the right and left boundaries and directly below the salt body in a layer about 200 m thick. The lower resolution of the lateral boundaries are caused by the low illumination in these parts. In the middle of the model the illumination is better and the waves travel through the model in several directions. The poor resolution directly below the salt can be explained by the drop in the velocity.

All in all, the resolution test shows the good suitability of the model together with the used acquisition geometry for the generation of good inversion results. But it also shows that below the salt body only a limited resolution can be expected.

4.6 Starting model generation using the flooding method

A crucial part in FWI is the selection of an appropriate starting model. It needs to explain the data sufficiently well in the frequency range where the inversion is started. If the error of seismic phases in the data space of the starting model is more than half a wavelength, the risk of fitting wrong phases is given. The results are artefacts in the inverted model. They appear as erroneous velocity updates not present in the true model. For the synthetic case, artefacts can easily be detected as the true model is known. For field data inversion, the identification of artefacts is not that easy. After the inversion, several parameters can give a hint of the success and the reliability of the FWI result, such as, for instance, the misfit development during FWI or the data fit.

To ensure a good quality of the starting model, usually a traveltime tomography is used. In this work, however, the starting model is also created with FWI. This avoids the application of several different methods for the starting model generation. All steps can be performed inside one FWI workflow. For this purpose, I apply a flooding method, based on the method proposed by Boonyasiriwat et al. (2010). It starts the inversion using a constant velocity

(a) Starting model.

(b) True model.

(c) Inversion result.

(d) Difference plot of starting model minus inversion result.

(e) Misfit values normalised to first misfit value.

(f) Profile of v_P values at $x = 43.75$ km.
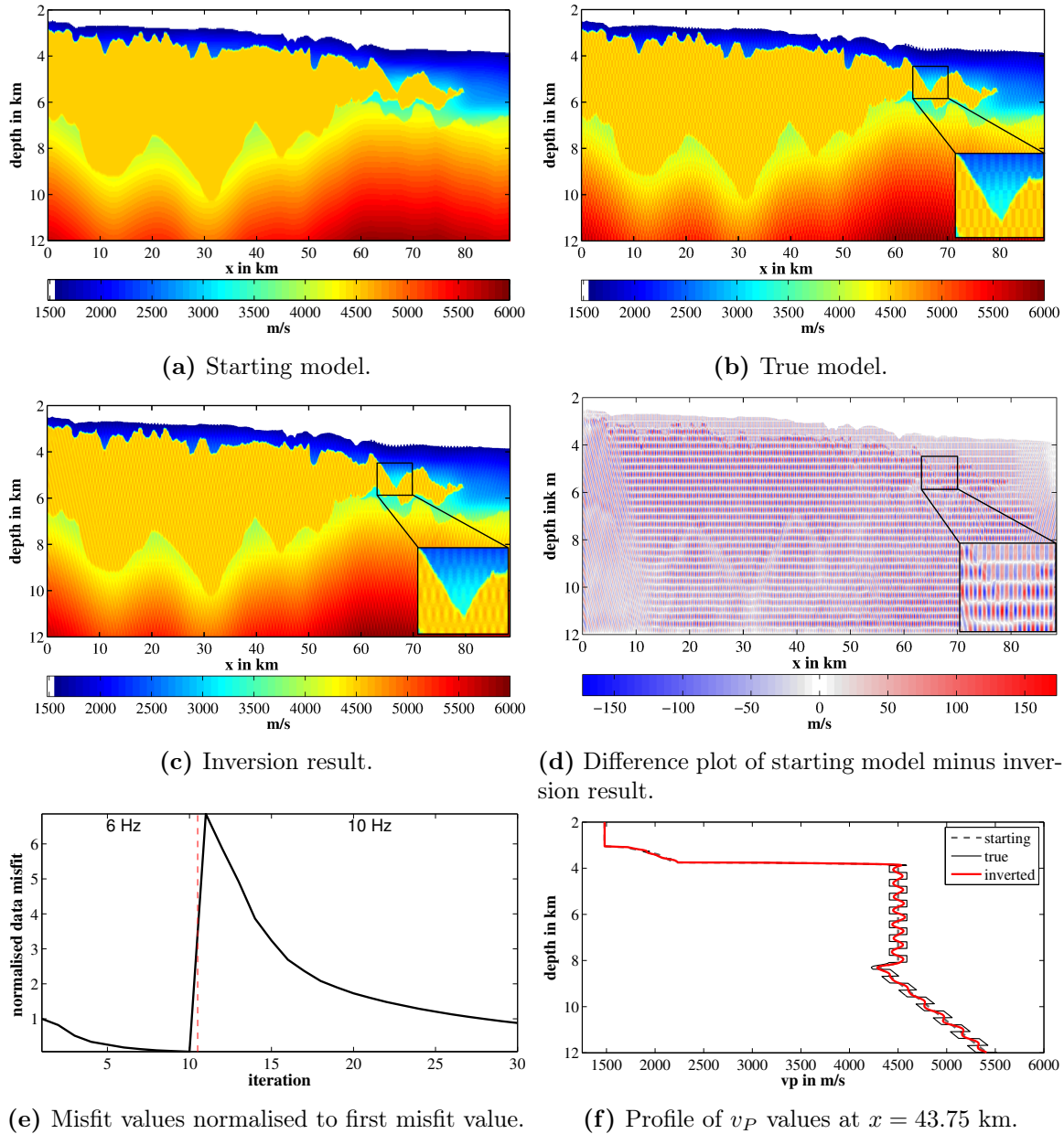
Figure 4.4: Inversion result (v_P) of a chequerboard test after 40 iterations.

model with an estimated water velocity as starting model. After a few iterations, the seabed appears in the inversion result and can be picked. At the location of the interface, the wavelet appears in the inversion result. The location of the interface is picked between the first and second extremum of the wavelet as previous tests revealed. The picked points are interpolated for all grid points in x-direction by using the *pchip* method in *MATLAB*, a shape-preserving piecewise cubic interpolation. Below the picked line, the model is flooded with an estimated gradient for sediment velocities. After the flooding of the sediments, this model is used as starting model for the next inversion step. After a few iterations, the top of salt (TOS) can be picked in the inversion result and the model below is flooded with an estimated salt velocity. Using the flooded model as new starting model, the bottom of salt can be picked in the resulting model after a few iterations. The method is described in detail for the synthetic

case in Thiel (2013). In contrast to the method proposed by Boonyasiriwat et al. (2010), my method requires significantly less iterations and uses a vertical velocity gradient for the sediment flooding. The gradient is more realistic and can enhance the inversion development and the resulting model.

The picking of the seabed is usually not necessary, as the water depth is monitored continuously during the marine acquisition. Therefore, for the synthetic tests, I only pick the TOS and BOS. However, for the generation of the starting model from field data, I also perform the picking of the sea floor for calibration reasons and quality control.

The frequency content in the inversion is kept as low as possible (2-5 Hz). On the one hand, this leads to a significantly lower resolution of the interface and, therefore, increases picking errors. But on the other hand, low frequencies avoid the influence of low-wavenumber structures above the target horizon. In addition, the subsequent inversions start also at low frequencies and should be able to correct small location errors by smoothing the sediment-salt interfaces.

In the next two sections, I show the application of the flooding method in the synthetic case using the PGS model (model 2) as true model. A synthetic test prior to the flooding using the field data can reveal challenges due to the geological composition, such as low reflection coefficients for important interfaces.

4.6.1 Top of salt

As explained above, the seabed depth and topography is well known in most cases due to additional measurements. Thus, the first interface that had to be localised is the TOS. For this purpose, the starting model was generated by picking the sea bottom automatically from the PGS model and flooding below with a sediment velocity gradient. The resulting starting model can be seen in figure 4.5a.

The TOS is together with the sea floor the most prominent reflector in the data and the model. Therefore, after only two iterations the inversion result was good enough in order to be able to pick the salt surface. The inversion result of the P-wave velocity model (figure 4.5b) does not look very different in comparison to the starting model in figure 4.5a, but in the difference plot (figure 4.5c) the salt surface appears clearly. I picked the TOS by hand and interpolated it. It is plotted as green line in figure 4.5c. In order to assess the quality of the picking result, the contour of the salt body from the true model is plotted additionally in black. By comparing the two lines it can be observed that the salt surface was picked correctly with an error of less than 50 m in most parts. Only in the deep valleys there are errors of about 100 m (about one fourth of the minimum wavelength at 5 Hz). The larger errors in the valleys can be explained by the poor illumination in this areas. Therefore, these errors should not significantly influence the following inversions.

For the next flooding step, the starting model was modified by flooding below the picked TOS with salt velocity. To allow a correction of the TOS location during the inversion to

compensate small picking errors, a 200 m thick gradient zone was inserted around the picked TOS. FWI can move the location of a sharp interfaces only with difficulties. The flooded result is shown in figure 4.5d.
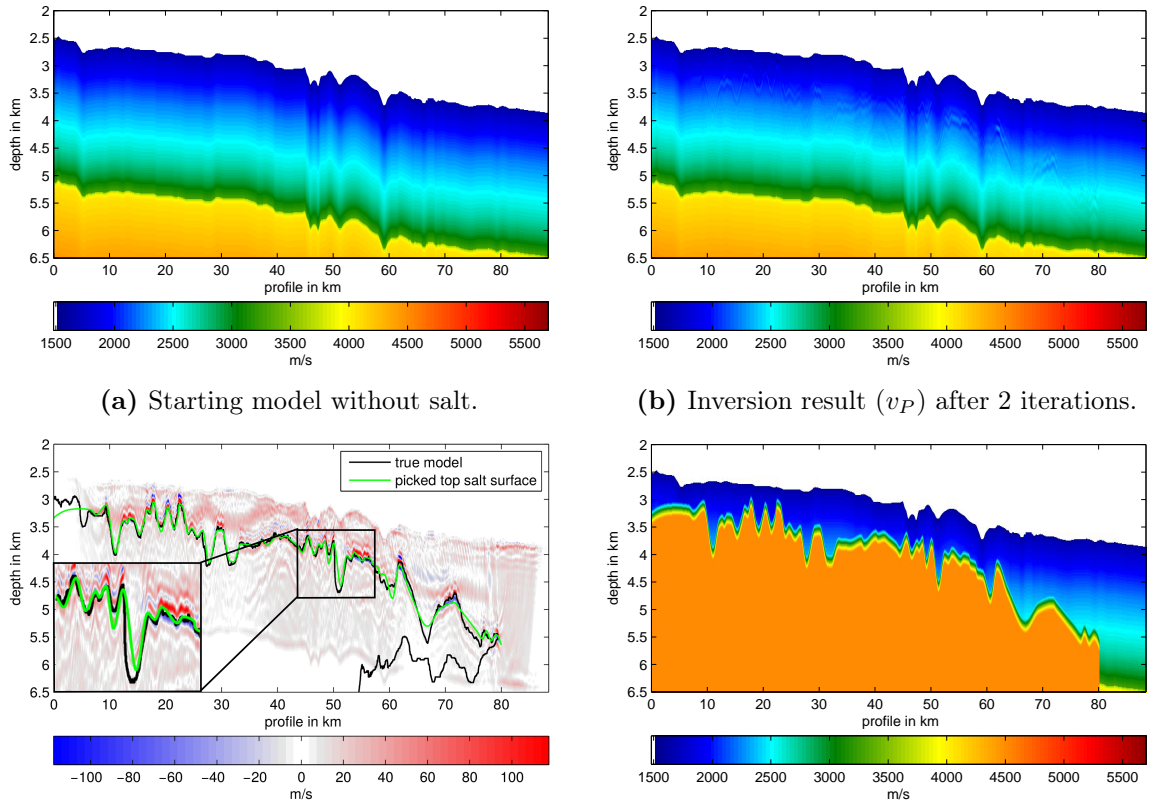
(a) Starting model without salt.

(b) Inversion result (v_P) after 2 iterations.

(c) Starting model minus inverted model: the green line represents the picked TOS, the black line shows the location of the salt body in the true model.

(d) Starting model with flooded salt velocity below the picked TOS and included gradient zone.

Figure 4.5: v_P model during the picking procedure of the top of salt (TOS) and flooding below in a synthetic test.

4.6.2   Bottom of salt

The identification of the bottom of salt was more challenging. As starting model, the flooded model in figure 4.6a was used. Due to the low reflection coefficient and the depth of this interface, 10 iterations were necessary (figure 4.6b). Also, small location errors of the TOS influence the inversion quality. After this number of iterations the sea floor started to appear in the difference plot in figure 4.6c. The picked interface is marked as green line. The difference plot is trace normalised due to strong variations in the amplitude. As the salt body in the right part is thinner and located shallower, the updates in this area of the model are higher.

The result after picking and flooding the model with a sediment velocity gradient below the picked BOS is shown in figure 4.6d. I used the sediment velocities of the corresponding area of the starting model. In addition, the contour of the salt body in the original model is plotted in black. By comparing the picked salt body with the black line, a good consistency

(a) Starting model with flooded salt.

(b) Inversion result (v_P) after 10 iterations.

(c) Starting model minus inverted model (trace-normalised): the green line represents the picked BOS.

(d) Model flooded with a sediment velocity gradient below the picked BOS. The black line shows the location of the salt body in the true model.
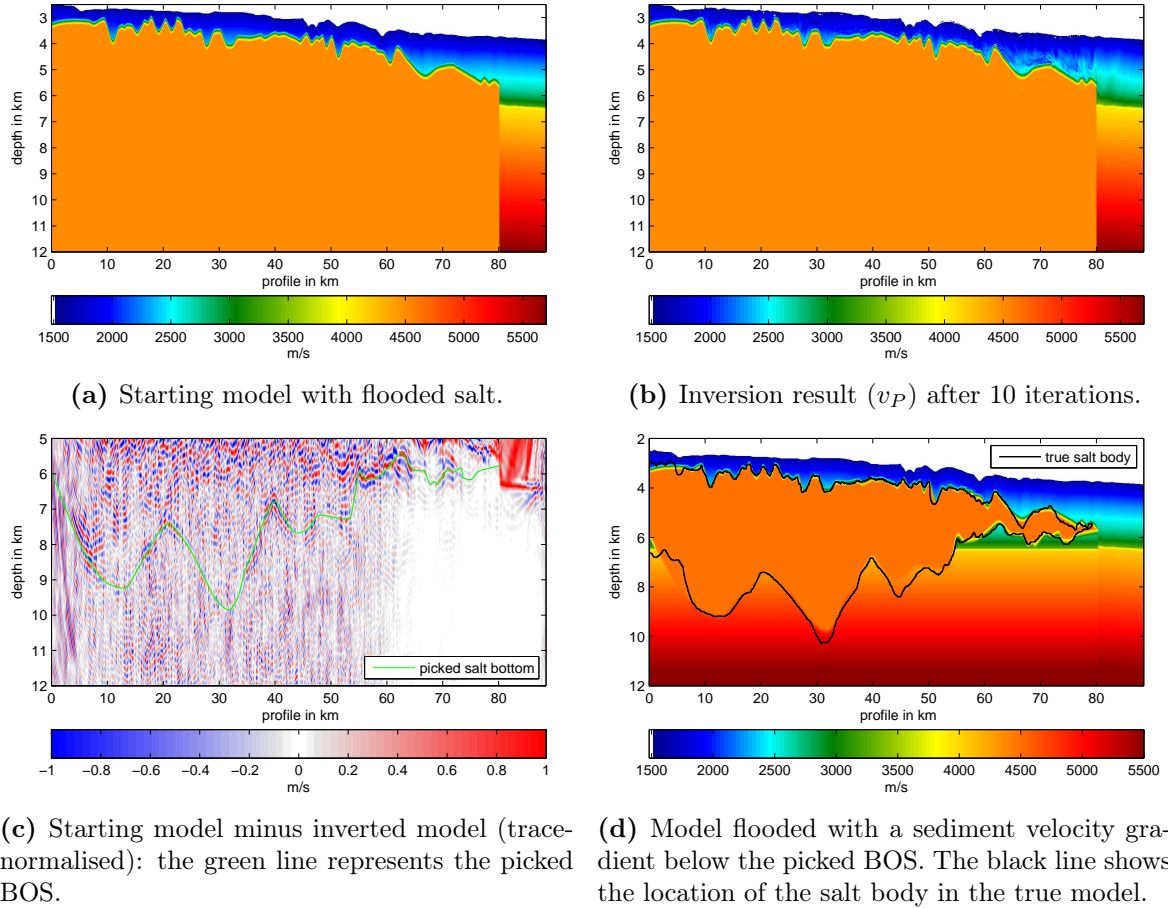
Figure 4.6: v_P model during the picking procedure of the bottom of salt (BOS) and flooding below in a synthetic test.

is noticeable. The biggest error of approximately 400 m is in the deepest part of the salt body (about half of the minimum wavelength in this area). In this part, the reflectivity is the lowest.

The synthetic tests in this section showed the potential of the flooding technique in FWI for the generation of starting models in the presence of salt. Only very few iterations are necessary to include the salt body in the velocity model. The resulting model from the flooding technique can then be directly used as input for FWI. How this approach works with field data will be investigated in the next chapter.

4.7 Summary

By performing several synthetic inversion tests, I could show the applicability of the inversion workflow. In the beginning of the chapter I showed the necessity to incorporate the wavefield separation into the workflow. Otherwise, no successful inversion was possible. Furthermore, I presented the chequerboard resolution test using field data acquisition geometry and the PGS model. The chequerboard test showed a good resolution throughout the entire model

except at the left and right boundaries as well as a layer directly below the salt of about 200 m thickness. I also showed the successful generation of a starting model including the salt layer starting from a constant velocity model by using the flooding method. In the synthetic case using a maximum frequency of 5 Hz, the TOS could be located with a maximum error of about 100 m and the BOS with a maximum error of about 400 m. The location errors of both salt interfaces already indicate potential difficulties for the application on field data.

Chapter 5

Field data inversion tests

In order to understand the field data as best as possible for the actual FWI and to analyse some features of the inversion, I performed the following inversion tests using the field data. The model was reduced to 20 km length and 8 km depth to allow an efficient testing (see also section 3.2). The dimensions of the new model (model 3) are 1600 grid points in x-direction and 640 grid points in z-direction with 12.5 m grid point distance in both dimensions. For the elastic tests the grid sampling was halved and, consequently, the number of grid points doubled in both dimensions (3200 × 1280). Unless specified otherwise, the same acquisition geometry given in the FWI tests with the 88.5 km large model in x-direction is used, shown in chapter 6. The number of shots was reduced to 19 based on the reduction of the model size. Figure 5.1 shows the v_P starting model, including the shot positions, on the left, and the data fit of the forward modelled data and the field data on the right.

The following sections show results from tests about the influence of data windowing and the 3D-2D transformation of the data on the FWI process. After the preprocessing tests, the effect of reducing the number of shots and the well known problem of cycle-skipping during FWI is presented. The last two tests in this section deal with the source time function inversion and the examination of parameter effects on the FWI result.

For all tests, the v_P inversion results are plotted. To be able to evaluate the quality of the results and the performance of the inversion, additional parameters are shown, including the data fit, the misfit development and the inverted source time functions. The data fit is plotted as interleave plot, which means that the field data are plotted alternately with the inverted data. The full shot gathers are shown in the appendix in figure A.1. A comparison of both shot gathers gives details on the quality of the data fit and possible cycle-skipping. The values of the objective function should decrease with increasing number of iterations and, therefore, show convergence. In the following tests, the objective function can also increase for a few iterations, especially in multi-parameter elastic FWI. The reason for this is firstly the implementation of the step length estimation that uses a parabolic fitting method (Köhn, 2011). In this method the misfits of three test step length are calculated. Due to computational reasons, only a subset of shots is used. The step length is plotted against the

misfit and a parabola is fitted through the the points. The minimum of the parabola gives the best step length. After applying the update for all shots with the given step length, the misfit can vary from the misfit calculated using only the subset of shots. In addition, I set the minimum number of iterations to 8 (see section 4.4), which also allows possible updates with higher misfit values.
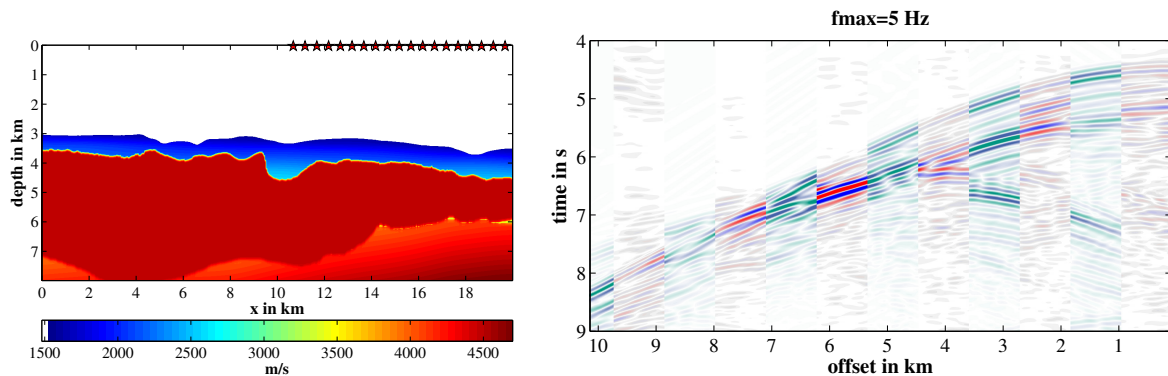
(a) Starting v_P model for the field tests. The stars indicates the shot positions. The streamer is located on the left of each shots with about 10 km length.

(b) Interleave plot showing the field data (red/blue) and the modelled data (green/blue) based on the starting model of shot 7 for the first frequency band ($2 - 5$ Hz).

Figure 5.1: v_P starting model for field data inversion and the corresponding data fit.

5.1   Influence of the 3D-2D transformation

As written in section 3.3.1, I applied a 3D-2D transformation on the field data by using the program *lisousi* (Forbriger et al., 2014). During the inversion tests, data with and without 3D-2D transformation were used. The inversion results reveal only little difference (cp. figures 5.2a). This is a consequence of the source time function (STF) inversion. Some differences resulting from the missing dimension can be compensated by the STF inversion. By comparing, for example, the inverted wavelets of shot 9 in figure 5.2d, the 3D-2D transformed data fits better to the neighbouring wavelets than the one inverted from data without the 3D-2D transformation. On the other hand, wavelets 6 to 8 in figure 5.2d are still not similar to the neighbouring wavelets. This can, however, also be caused by other influences, such as, for example, errors in the starting model. Despite the small differences in the results of the inversion with and without the 3D-2D transformation, I decided to apply the 3D-2D transformation to the field data because from the theoretical point of view it should be correct.

5.2   Data windowing

The influence of data windowing is explored in this section. I conducted two tests. The first uses a time window to limit the data to a window that follows the first arrival of the first reflections and refractions and has a constant length of 2 s. The second test analyses the influence of offset limitation.
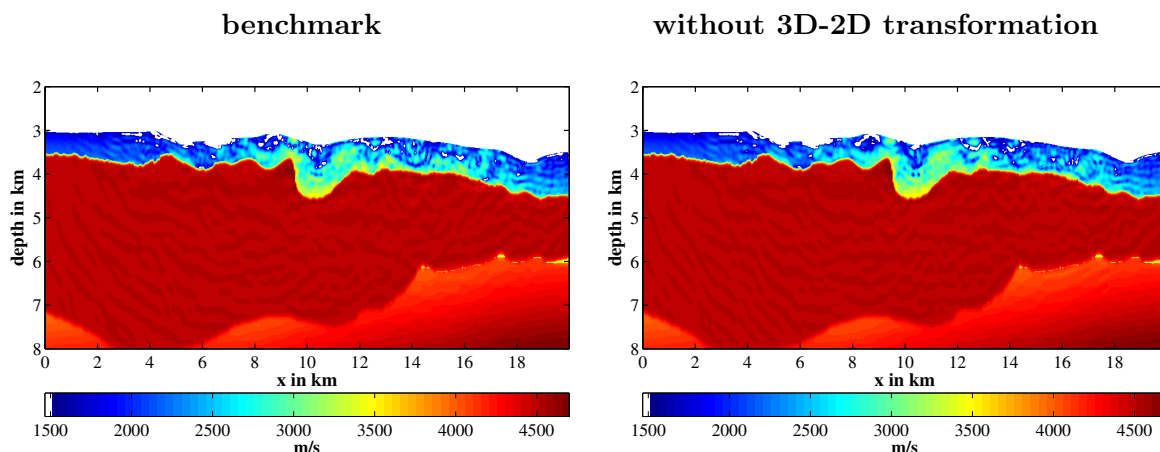
benchmark   **without 3D-2D transformation**

(a) v_P inversion result after 50 iterations.
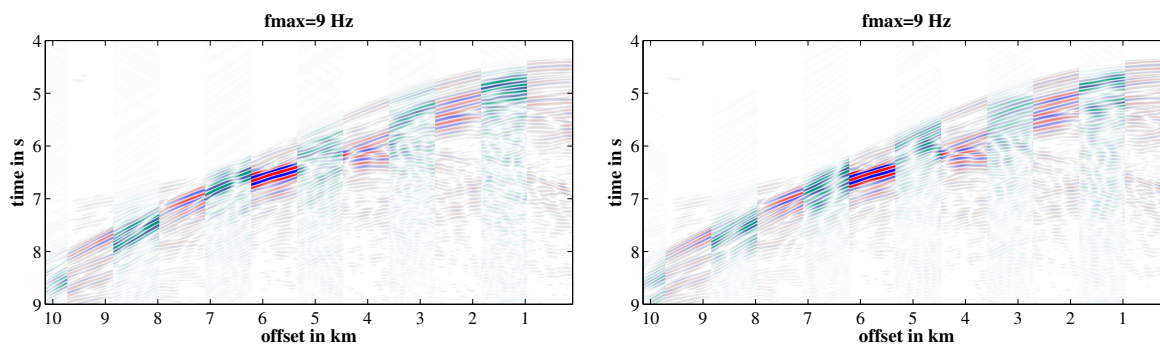
(b) Interleave plot showing field data (red/blue) and inverted data (green/blue) of shot 7. The full shot gathers are shown in appendix A.
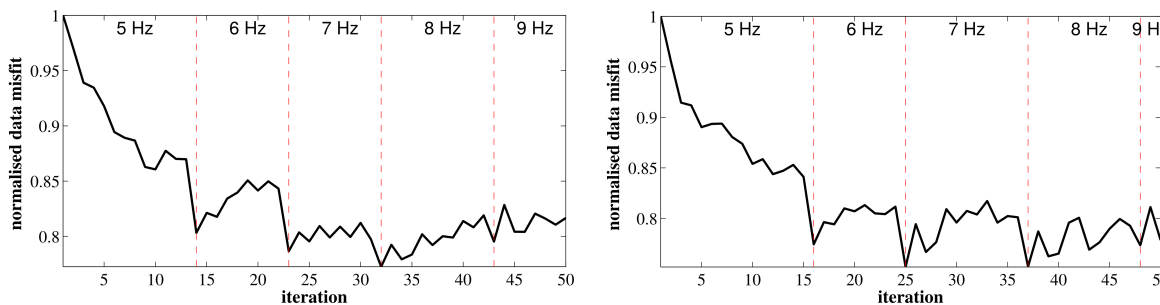
(c) Misfit development during inversion.
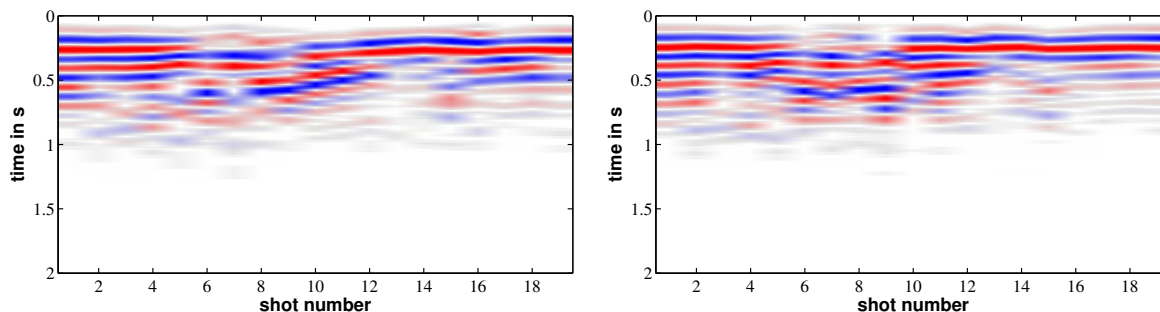
(d) STF inversion result at last frequency step.

Figure 5.2: Inversion results after 50 iterations. Left column: results with 3D-2D corrected data; right column: results without 3D-2D correction applied to the data.

The time windowing will limit the influence of deeper and not yet optimised regions of the model. The main contribution will be made by the reflections of the sea bottom and salt surface. In the left column of figure 5.3 it can be observed that the data misfit decreases monotonously in most parts and that the inversion can almost halve the misfit during the first 50 iterations. In comparison with the benchmark results in figure 5.2, left column, the misfit decreased 20 % more by using the time window and also the STF inversion results are more similar to each other. The inversion can limit the updates to a smaller part of the data, which leads to better inversion results.

The usage of only the first half of all offsets did not change the inversion result significantly. By comparing the inversion results of the second test using only offsets up to 5 km, displayed in figure 5.3a (right column), with the benchmark results in figure 5.2 (left column), no considerable changes can be seen. This shows the low influence of the longer offsets on the inversion results in the beginning of the inversion for this data set.

Due to the good results of the time windowing I restarted the inversion and let it run for more iterations. The results after a full FWI up to 14 Hz of the time-windowed data and the benchmark test can be seen in figure 5.4. The inversion was able to reduce the misfit down to 60 % of the initial misfit. In figure 5.4c it can be observed that after 50 iterations, the misfit was not reduced any more. By examining the data fit during the inversion it can be said that the reason for the stagnated decrease in the data fit is the bad fit of relative amplitudes. For instance, the amplitude difference between the reflection of the sea floor and the reflection of the salt are considerably higher in the field data than in the synthetic data. The inversion cannot fit the synthetic waveforms to the field data well enough in order to fit higher frequency information. This is the result of elastic effects which cannot be explained by the acoustic inversion, as subsequent tests show.

5.3   Effect of shot selection

All shots have varying quality related to the signal-to-noise ratio or the number of diffractions. Therefore, I conducted a test with varying shot positions and number of shots per inversion to study the influence of the shot selection on the FWI process and its results. In a first test the shot distance was kept at 500 m, but I selected the shots located in between the previously used shot locations for the inversion. Thus, all used shots differ from the shots used for the benchmark test in figure 5.2, left side. The result is shown in figure 5.5, left side. The misfit development and the lowest misfit are similar to the benchmark test. Also, the inversion result and data fit are similar and differ only in details. The STF inversion results are more inhomogeneous and shots 6 to 11 have a stronger amplitude at the beginning of the wavelet. From the very similar results of the benchmark test and the test using a totally different subset of the original data I conclude that the shots chosen for the inversion are representative. The changed subset of data has a similar number of shots with varying inverted wavelets compared to the benchmark test, showing also a comparable quality of the two subsets of data.

time-windowed data   **first half of all offsets**

(a) v_P inversion result after 50 iterations.

(b) Interleave plot showing field data (red/blue) and inverted data (green/blue) of shot 7.

(c) Misfit development during inversion.

(d) STF inversion result at last frequency step.
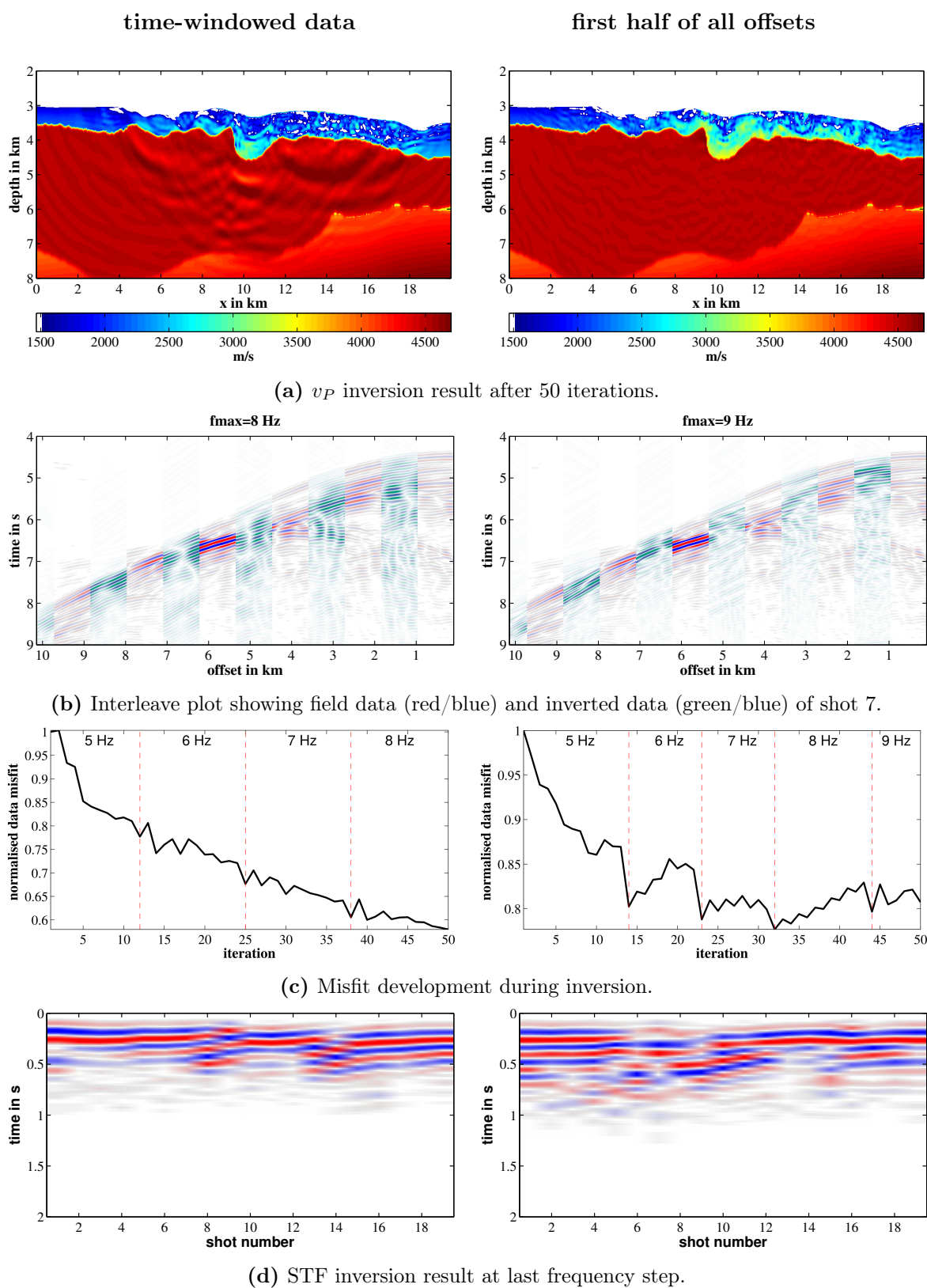
Figure 5.3: Inversion results after 50 iterations. Left column: results using time-windowed data (first arrival plus 2 s); right column: results using only the first half of all offsets (near-offset part) of the data.

benchmark   **time-windowed data**

(a) v_P inversion result after 130 (benchmark) and 142 iterations (time-windowed data).

(b) Interleave plot showing field data (red/blue) and inverted data (green/blue) of shot 7.

(c) Misfit development during inversion.

(d) STF inversion result at last frequency step.
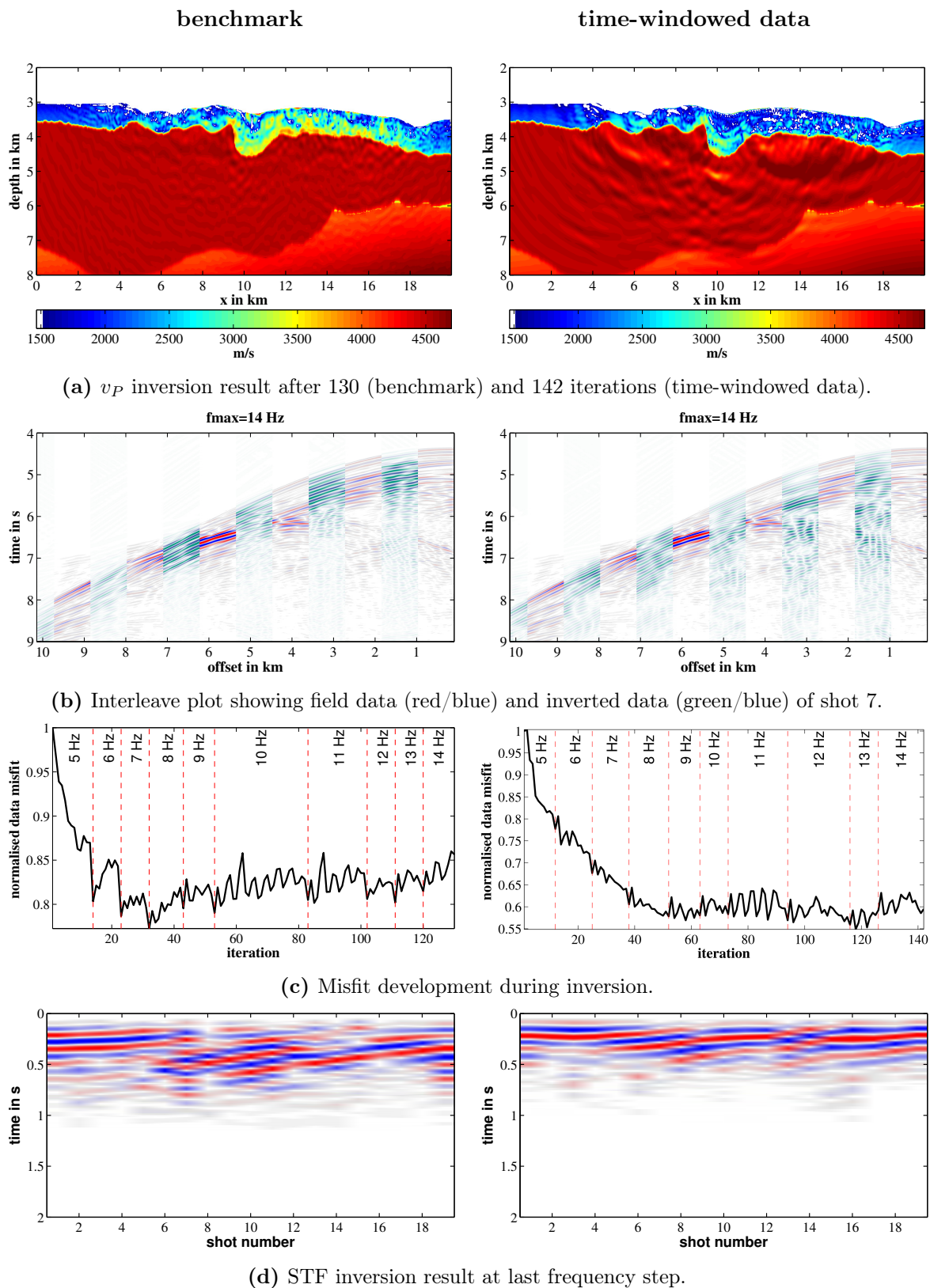
Figure 5.4: Results after full inversion. Left column: results of benchmark test; right column: time-windowed data (first arrival plus 2 s).

The second test uses two times the number of sources with halve the source distance (250 m). Thus, FWI uses the shots of the previous test and the shots of the benchmark test. Consequently, the computational time is almost doubled. The result is shown in figure 5.5, right column. Again, the misfit is very similar to the previous test. In the inversion result the high-velocity/density layer above the top of salt is marginally more continuous and clearer visible. The prominent diffraction in the data is better visible, starting at 7 s at near offsets and having its peak at about 6 s at 4.5 km offset. Also the STF inversion looks more homogeneous, indicating a better model-data adaptation. It can be concluded that more shots are better, but resulting in higher computational cost. For the inversion, I will use a shot distance of 500 m, as the advantages of using more shots are limited due to the low frequencies used for inversion, and I have only access to a restricted amount of core hours.

5.4 Cycle-skipping

The starting model is one of the most crucial and important parts of a successful FWI. To study the influence of the starting model and the potential occurrence of cycle-skipping, the starting model was moved vertically. For my test, the starting model was moved down by 100 m. The 100 m move is equal to about one fourth of the minimum wavelength at 5 Hz maximum frequency content of the data. The results of the modelling in comparison with the field data are displayed in figure 5.6. An obvious mismatch of the shot gathers can be observed in all regions. The main events are shifted by more than one cycle, thus, the occurrence of cycle-skipping artefacts in the inversion result is expected.

In figure 5.7 the results of FWI after 15 iterations are shown. The inverted model using the down-shifted starting model shows the correction of the sea floor location. The inversion is able to move the sea bottom upwards as the contrast from water to sediments is not very high. In contrast, the location of the salt body could not be moved. In order to match the dominant reflection of the salt surface in the data, the velocity in the sediments is increased. Another effect of using an insufficient starting model can be seen in the STF inversion results (figure 5.7d, left side). The inversion tries to compensate the bad starting model by creating complex source wavelets. This shows the necessity of a good starting model for an STF inversion. The combination of a bad starting model and STF inversion can lead to an inversion process with decreasing misfit. Therefore, the STF inversion needs to be monitored carefully.

The outcome of the test shows the large influence of the starting model on the inversion quality. The down-shifting of the model decreased the model quality significantly and resulted in several artefacts in the model. Therefore, the starting model should be as accurate as possible. High-contrast interfaces cannot be relocated by FWI. Several further tests with the given model and acquisition geometry using larger and smaller shifts of the starting model revealed that prominent interfaces should be correctly located within less than 100 m in the starting model for a successful FWI in the frequency band of $2 - 5$ Hz.
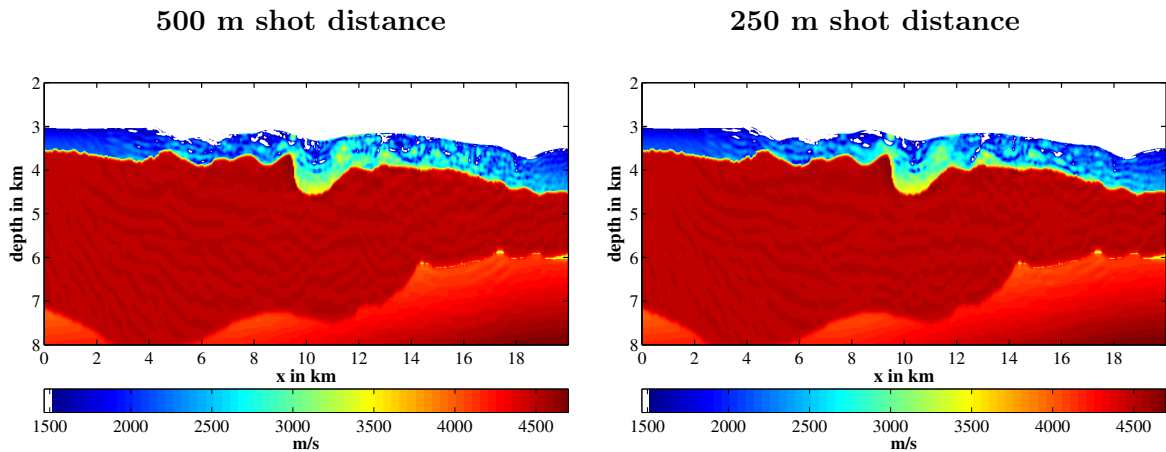
500 m shot distance   **250 m shot distance**

(a) v_P inversion result after 50 iterations.
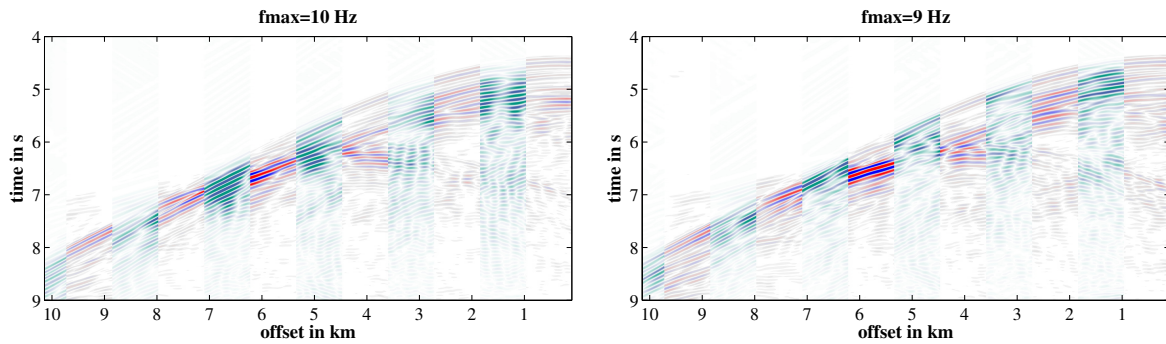
(b) Interleave plot showing field data (red/blue) and inverted data (green/blue) of shot 7 (left) and shot 13 on the right (same shot coordinate).
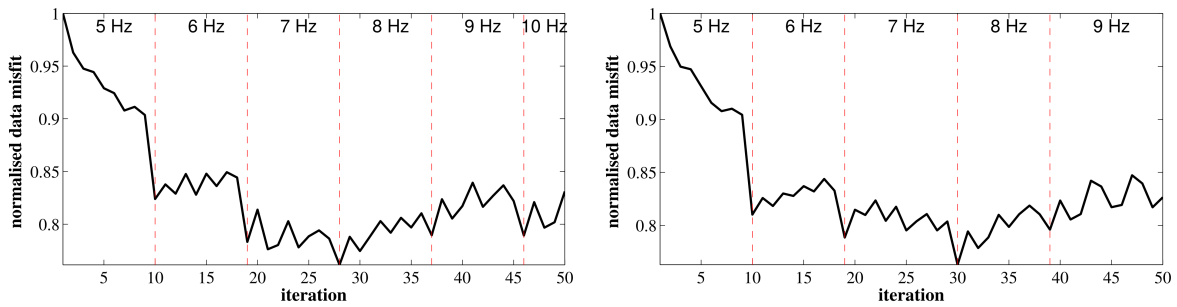
(c) Misfit development during inversion.
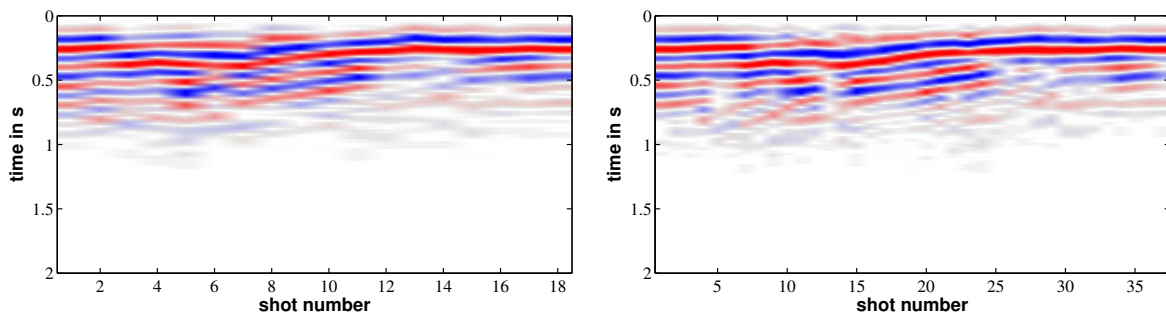
(d) STF inversion result at last frequency step.

Figure 5.5: Inversion results. Left column: results with 500 m shots distance (different shot selection as benchmark test); right column: results with 250 m shot distance.

(a) Starting model moved down by 100 m.

(b) Starting model moved up by 100 m.
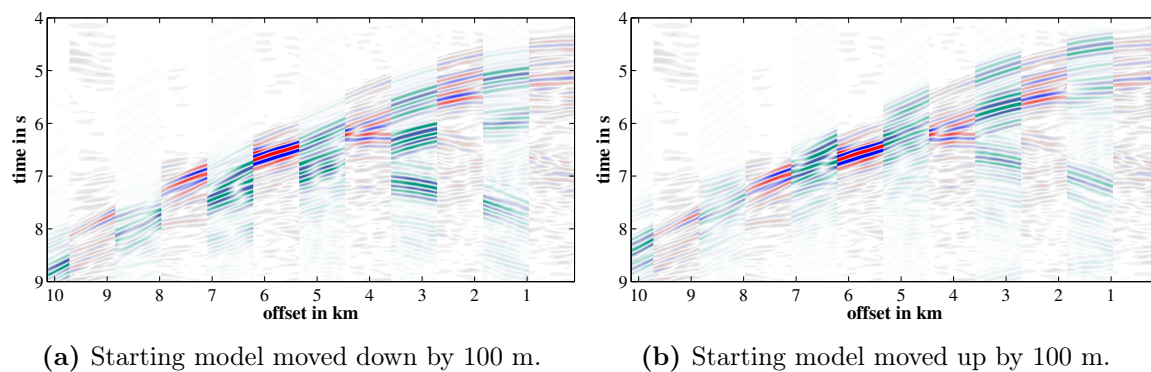
Figure 5.6: Interleave plot showing field data (red/blue) and inverted data (green/blue) of shot 7 after first iteration.

(a) v_P inversion result after 15 iterations.

(b) Interleave plot showing field data (red/blue) and inverted data (green/blue) of shot 7.

(c) Misfit development during inversion, normalised by initial misfit of benchmark inversion.

(d) STF inversion result at last frequency step.
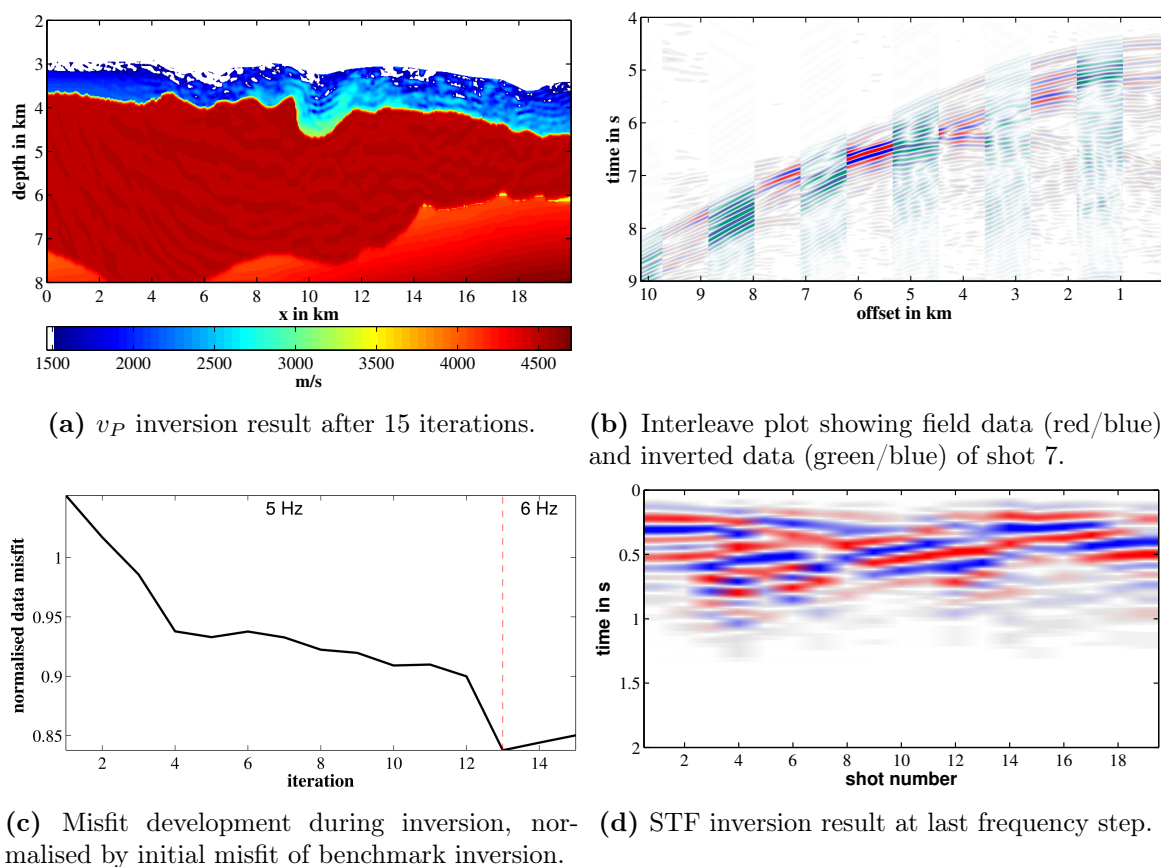
Figure 5.7: Inversion results using starting model shifted down by 100 m.

5.5   Model parameter effects

IFOS2D allows to invert separately for three parameters: P-wave velocity, S-wave velocity and density. For the acoustic case, the user can choose between the inversion of v_P and/or density. For the elastic case, additionally the inversion of v_S is possible. In this section, I study the influence of the inversion on different parameters. For the elastic inversion, the grid distance needed to be reduced to 6.25 m in order to match the dispersion relation. This results in a model size of four times the size of the original model. Also the time sampling needed to be reduced to 0.6 ms in order to match the Courant-Friederich-Lewy criterion (section 2.1.2). These two changes result in a significant increase of the computational time and memory requirements.

The results of the acoustic inversion of only v_P, and of v_P and density, as well as the elastic inversion of all three parameters are shown in figure 5.9. By comparing the v_P models of the acoustic inversions with and without density inversion, no obvious differences are visible after 20 iterations. The elastic inversion result, however, already shows differences in comparison to the acoustic inversions. The velocities of the sediments above the salt, especially in the salt valley at about $x = 10$ km and 4.5 km depth, were not increased as much as in the acoustic case. In both density models, the layers in the sediments are clearly visible, much better than in the v_P models. But in the acoustic case, the density contrast is very high due to unrealistically low values of partly below 1300 $\frac{\text{kg}}{\text{m}^3}$. The expected values for the sediments start at 2100 $\frac{\text{kg}}{\text{m}^3}$ in the literature (see table 3.1). The velocity differs partly more than 600 $\frac{\text{m}}{\text{s}}$ within less than 100 m. In the elastic case, the differences are lower and seem to be more realistic. The lowest density is about 1900 $\frac{\text{kg}}{\text{m}^3}$. The update of the v_S-model is marginal and updates can hardly be observed.

By looking at the data fits, misfit curves and STF inversion results, the differences of the results become even clearer. For both acoustic inversions, the results look very similar. Only very few events can be fitted and the STF inversions of the individual shots appear very heterogeneous. The misfit drops for the inversion of v_P and density slightly lower (about 77 %) than for the pure v_P inversion (about 83 %). In contrast to the acoustic inversion, most reflections up to 6 km offset can be fitted during elastic inversion. The misfit can be reduced by more than 40 % of the initial misfit value and also the STF inversion results are more similar to each other than in the acoustic inversions. Figure 5.8 shows an exemplary trace of the field data. In addition, the corresponding traces of the acoustic and elastic inversions are plotted. In figure 5.8a the data fit of the starting model is plotted. The first break and the main phases are fitting, but all other events are not fitting at all. After only 17 iterations at 2-5 Hz (figure 5.8b), most of the phases up to 6.5 s are fitting very well. The amplitudes are better adapted to the field data using the elastic inversion, especially in the beginning. Nevertheless, after the main reflections from the seabed, the sediments and the salt (after 6.5 s) the fit becomes worse.

This test shows that the usage of elastic inversion is definitely producing better results than the acoustic inversion. On the other hand, there is a considerable increase of computational

cost. Comparing the two acoustic results, the inversion of density seems to enhance the overall inversion result slightly. Thus, I recommend to include the inversion of density in the acoustic FWI workflow when using reflection data. The literature supports these conclusions of using the density inversion (e.g., Plessix et al., 2013; Przebindowska et al., 2012). In particular for the usage of data dominated by higher-frequency components, which applies for this data set as it contains almost only reflections, the influence of the inversion depends highly on the accuracy of the density model (Chazalnoel et al., 2017). I showed already in Thiel (2013) that problems occur when inverting elastic data with acoustic inversion, also confirmed by other studies (e.g., Mulder and Plessix, 2008).

For a better understanding of the elastic effects on the wavefield I took a look into snapshots of the elastic wavefield propagation. Those results are presented in the next section. I also studied, which parameter is best suited for the picking of the interfaces.

(a) Starting model. (b) After 17 iterations
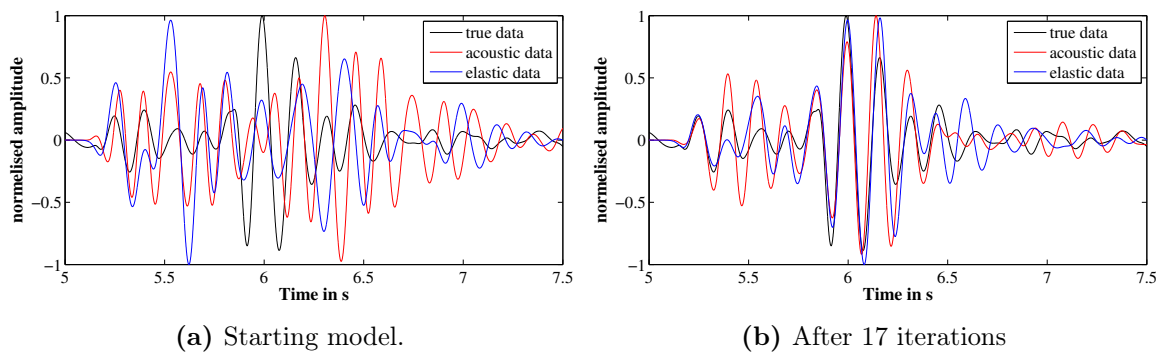
Figure 5.8: Trace 300 of shot 4 during acoustic (v_P, density) and elastic FWI.
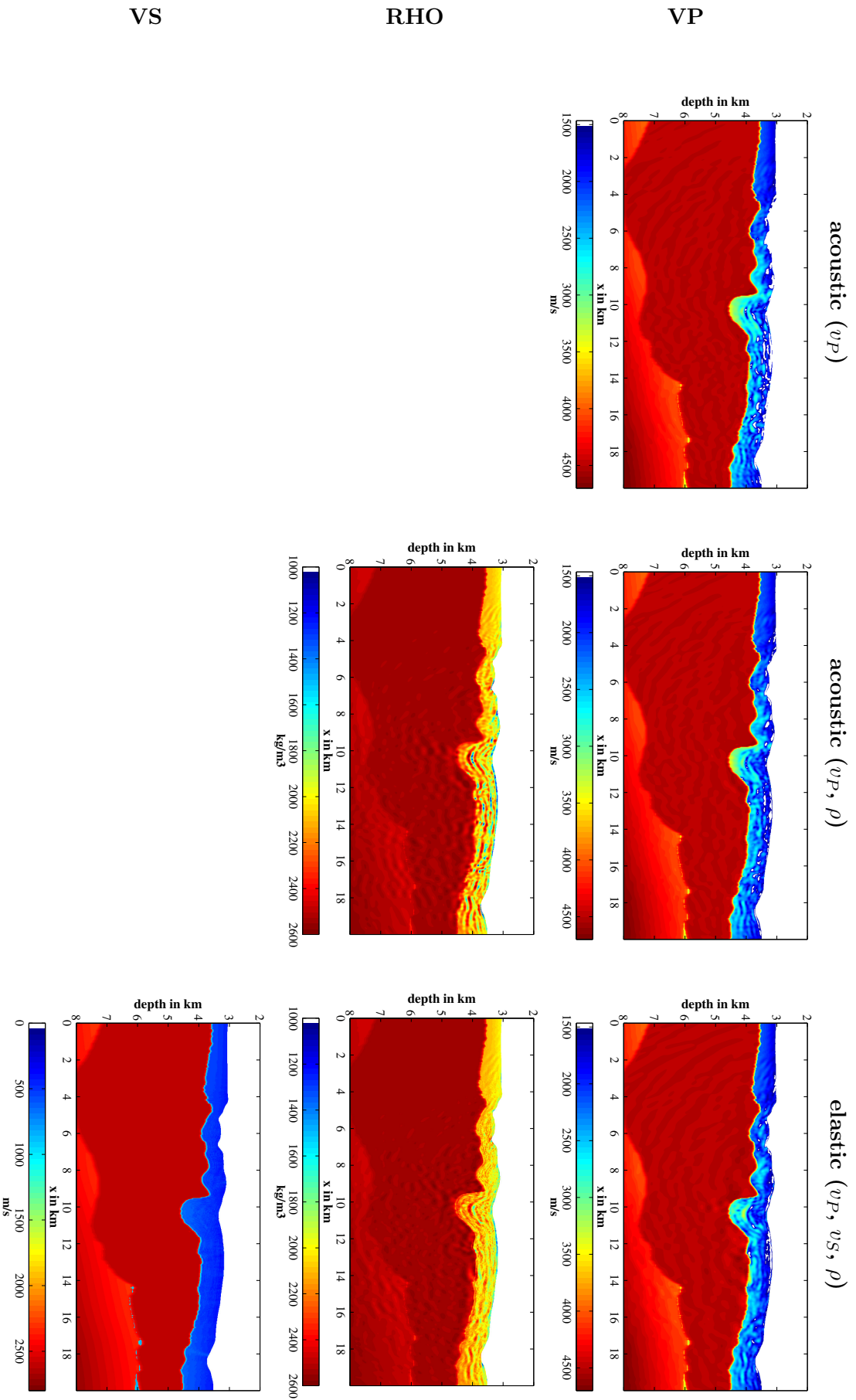
Figure 5.9: Inversion results after 20 iterations. Left column: acoustic inversion of v_P; middle column: acoustic inversion of v_P and density; right column: elastic inversion of v_P, v_S and density.
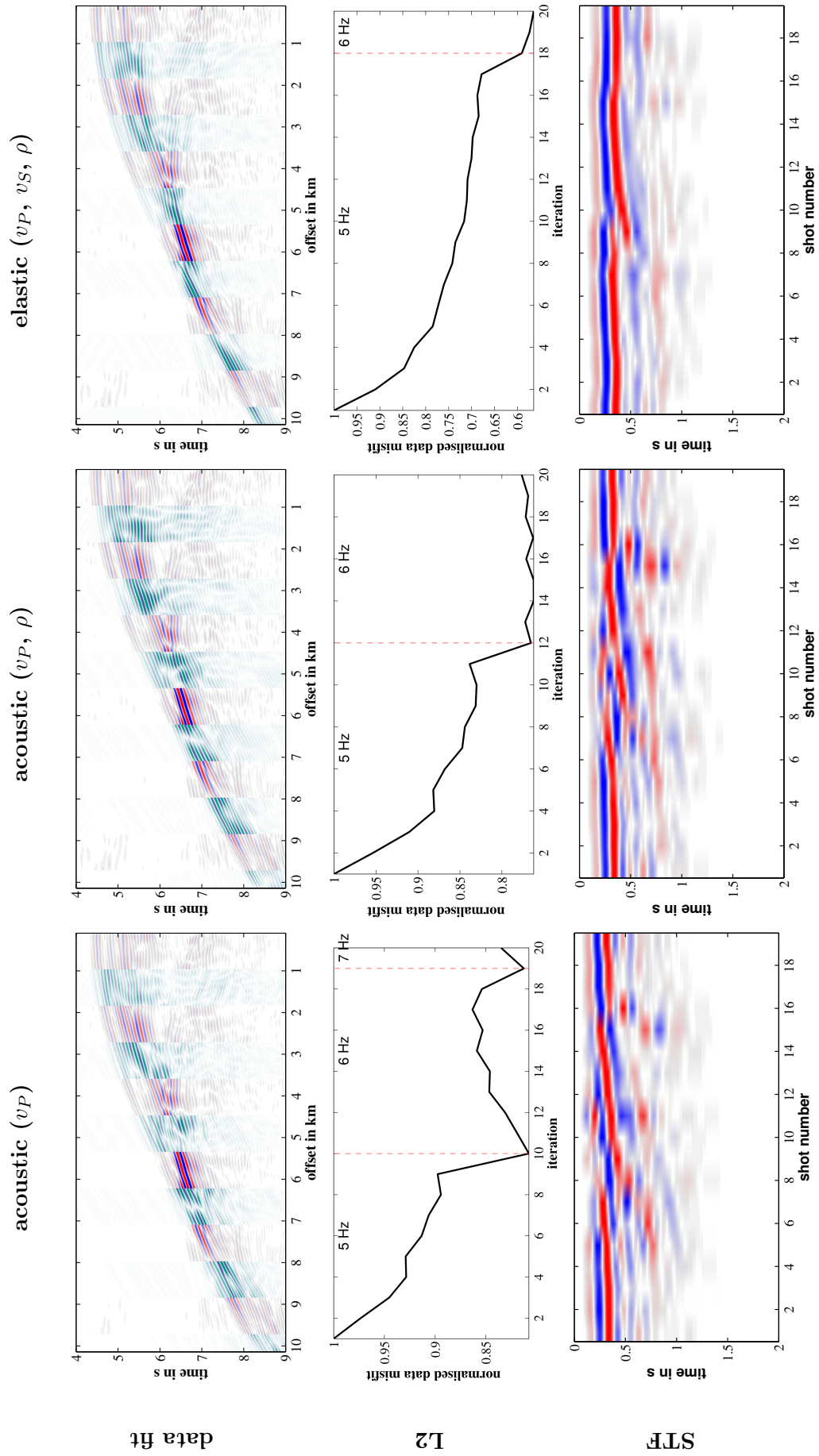
Figure 5.10: Inversion results. Left column: acoustic inversion of v_P; middle column: acoustic inversion of v_P and density (ρ); right column: elastic inversion of v_P, v_S and density. First row shows interleave plot of field data (red/blue) and modelled data (green/blue) of shot 7. Second row shows data misfit during inversion. Last row shows inverted source time functions for all shots.

5.5.1   Wavefields and seismograms

In order to study the influence of elastic properties of the subsurface on the wavefield, snap-shots of acoustic and elastic forward-modelled wavefields are displayed in figure 5.11. The wavefields were propagated in the model shown in figure 5.1a and a snapshot for shot 7 was taken at $t = 4.44$ s. For better orientation, two black lines were added to the snapshots: the upper line represents the sea floor and the lower line the top of salt. To ensure comparability, all snapshots are scaled equally. To be able to distinguish between the P- and S-waves in the wavefield, I show snapshots of the spatial divergence and magnitude of curl of the particle velocities (see chapter 2.1.4).

The upper three plots show the divergence of the acoustically or elastically modelled wavefield. The divergence represents the P-wave part of the full elastic wavefield. The curl of the elastic modelling is plotted in figure 5.11d, representing the S-wave part. For acoustic modelling, the curl is zero. A significant curl component can only be observed in the sediments above the salt. In water, the S-wave velocity is zero, but the P-wave is converted partly into S-waves when transmitted into the sea floor. Also, parts of the P-wave hitting the top of salt are converted into S-waves. A comparison of the amplitudes in the snapshots of the curl and divergence components shows that a considerable amount of the P-wave energy was converted into S-waves.

The difference plot in figure 5.11c shows the discrepancies of both divergence components of the wavefield snapshots. Since water is assumed as purely acoustic medium, the direct wave is the same in the acoustic and elastic simulation. Thus, the direct wave (first event from the left or right side at the surface in the first two plots) is not visible in the difference plot. Also, the reflection of the sea floor (second event from the left or right side at the surface in the first two plots) is hardly visible, as only little energy is converted into S-waves. Most of the differences appear in the reflection from the top of salt. In the upper two snapshots of the wavefield in figures 5.11, this event can be located as third event from the left or right border of the model at the water surface.

From the high amplitudes in the difference plot it can be concluded that the elastic effects in the presence of salt are considerable. But the effect does not appear as additional events in the data from converted waves. By comparing the wavefield snapshots of the divergence and curl components of the elastic forward modelling it can be observed that the main part of the converted energy is trapped in the sediment layer between the sea floor and the TOS, or transmitted into the salt layer. Therefore, the main differences in the seismograms are the change of relative amplitudes of the reflected events. This can be seen in particular for the salt reflection and the diffraction from the top of salt (see figure 5.11c). This effect makes it difficult for the acoustic inversion to adapt the waveforms. Despite the use of normalised seismograms, the relative difference in amplitude between the events is still present.

Whether the differences in the wavefields also appear in the shot gathers was analysed in figure 5.12. Again, both shot gathers were normalised to the maximum amplitude of the direct wave. When comparing the elastic and acoustic shot gathers themselves, differences

are already visible. For instance, in the acoustic shot gather an event starting at $t = 8.2$ s in the first trace, going upwards, is visible, which does not occur in the elastic shot gather. Also, the difference plot shows a large amount of energy, especially for the middle-offset range. It represents the energy converted into S-waves.
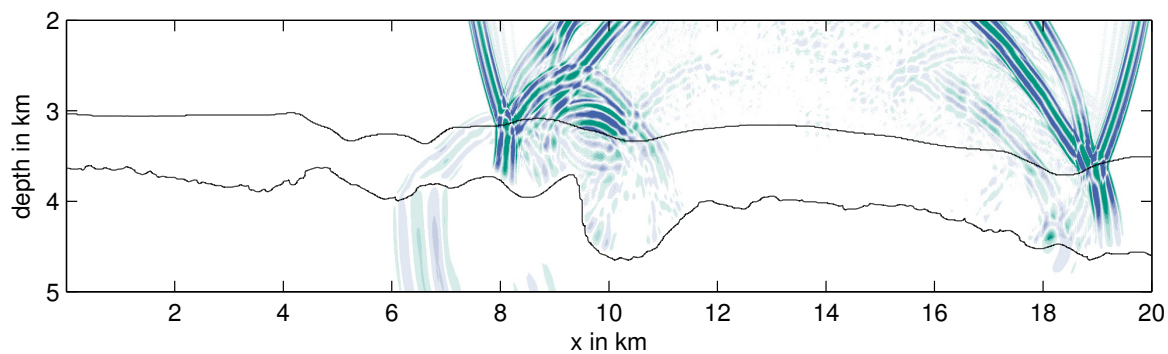
(a) Divergence wavefield of acoustic forward modelling.
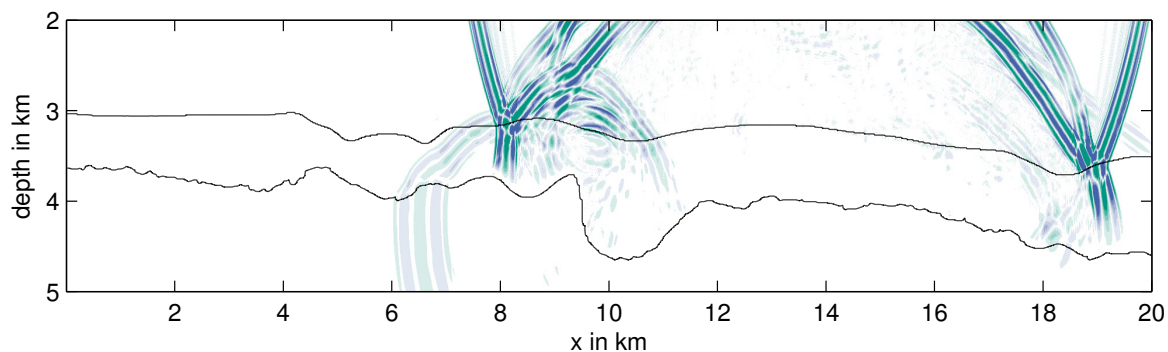
(b) Divergence wavefield of elastic forward modelling.
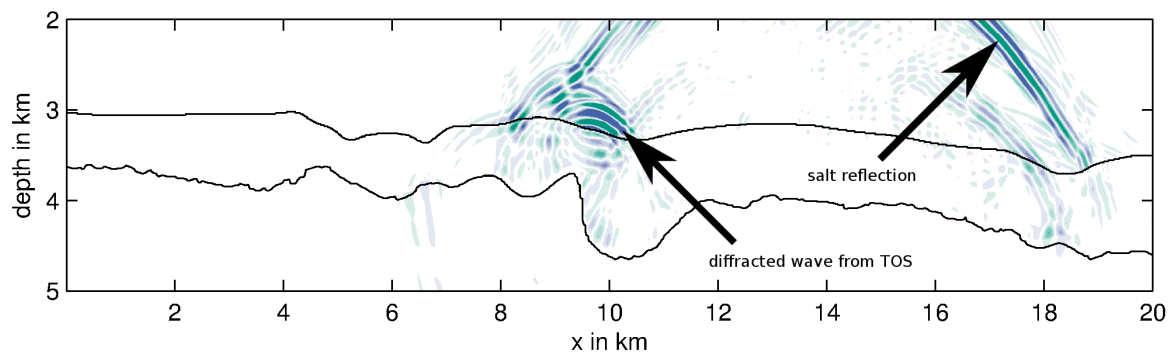
(c) Difference of the divergence wavefields shown in figures 5.11a and 5.11b.
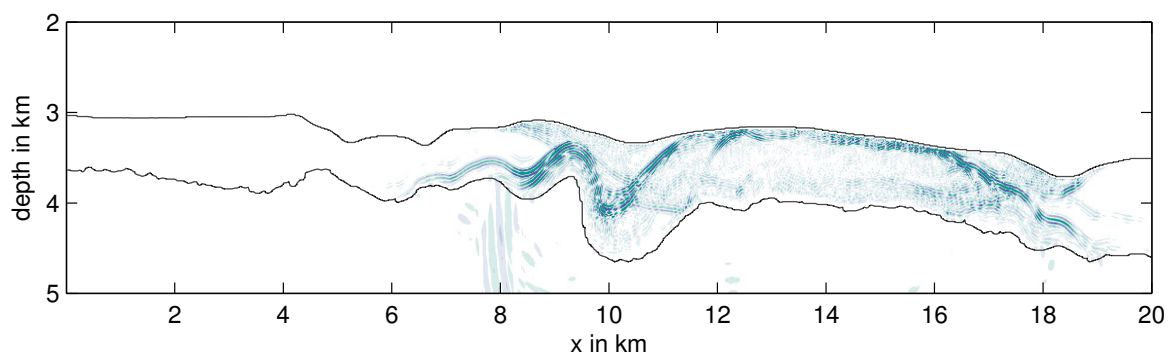
(d) Curl wavefield of elastic forward modelling.

Figure 5.11: Snapshots of the acoustically and elastically forward-modelled wavefields. Snapshots of the forward-simulated wavefield in the test model shown in figure 5.1a at $t = 4.44$ s. The first contour line in black represents the sea floor, the other contour line the top of salt. All amplitudes are scaled equally.
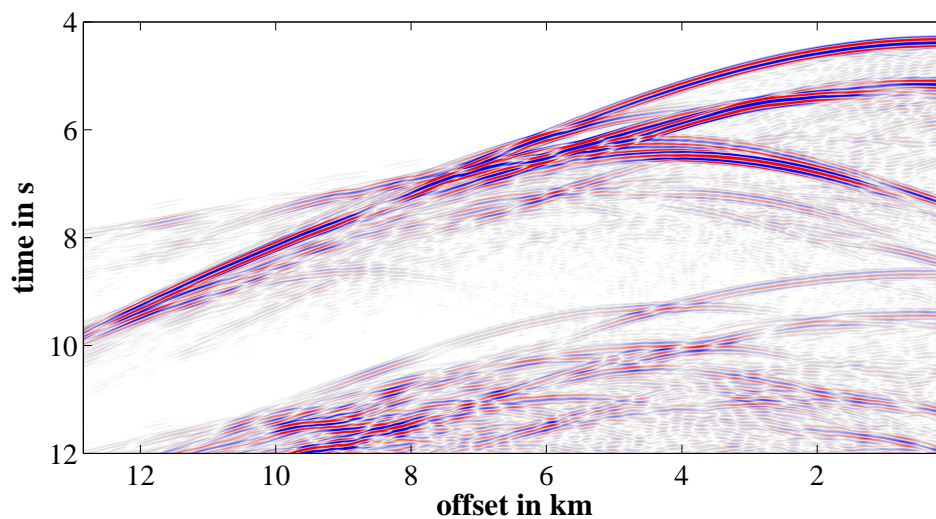
(a) Acoustic modelling.
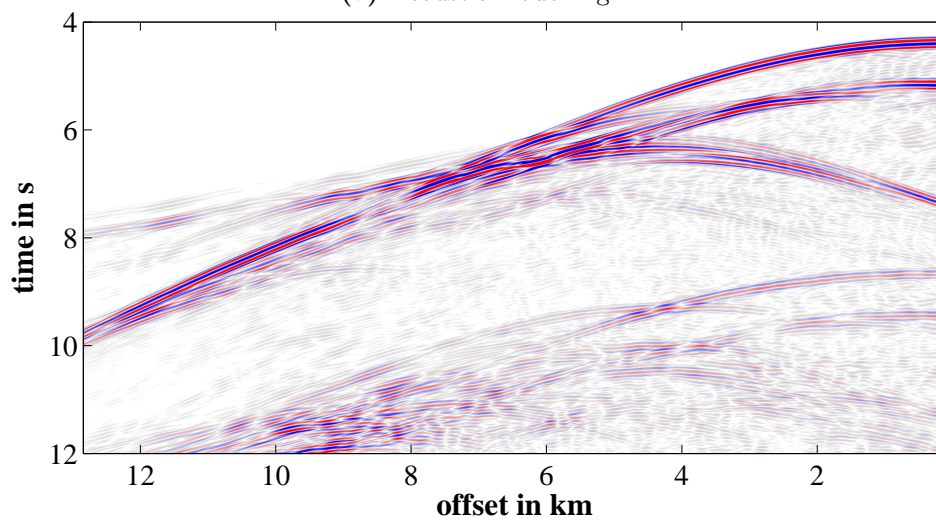
(b) Elastic modelling.
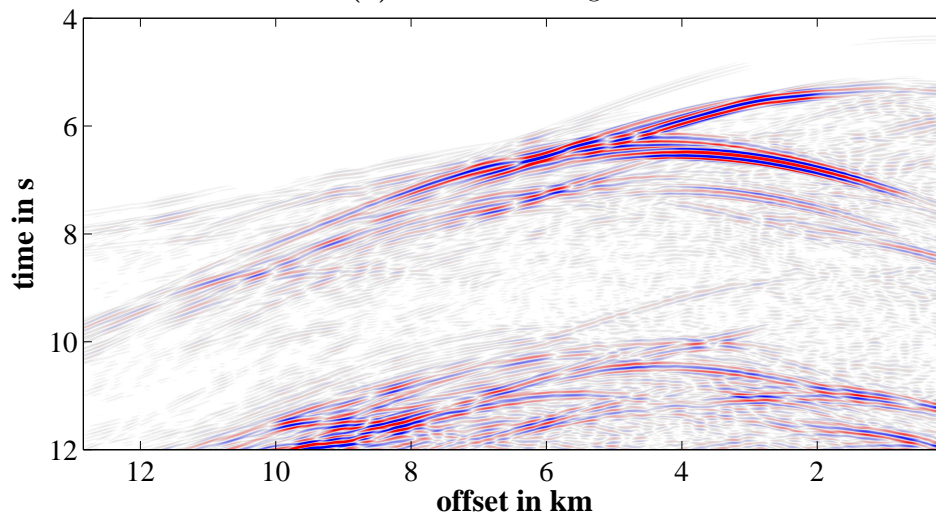
(c) Difference of the shot gathers shown in figures 5.12a and 5.12b.

Figure 5.12: Comparison of acoustic and elastic forward modelled seismograms (pressure component) in the test model shown in figure 5.1a, shot 7. In all plots, the amplitudes are scaled to the same value.

5.5.2   Picking interfaces

The picking of the interfaces was done by hand a difference plot where the starting model was subtracted from the inversion result. The difference plot shows the total update for all iterations. The outcome is shown in figure 5.13. For the picking, I used the inversion results after only one or two iterations. This small number of iterations is already enough to allow the inversion to insert the most prominent features which I would like to pick. In addition, the computational cost is kept low. In contrast to the inversion of the salt interfaces, I set the bandpass filter of the inversion for the sea floor to 2-14 Hz. The high frequencies are possible due to the homogeneous well known water column and allows the highest resolution possible with the used model and data. For calculating the difference plot, always the elastic inversion results were used.

In the left column of figure 5.13 the inversion result after one iteration is shown using the homogeneous water model as starting model. For the picking of the water bottom, the v_S model does not show any advantages in comparison to the v_P and density model. As the v_S velocity is set to 1 $\frac{m}{s}$ in the water (see section 3.2) and the starting model contains only water, the inversion result of the v_S model is not usable. Only noise is visible in the update. By comparing the v_P and density models, both have a similar resolution. In the right column, the starting model contained the picked water bottom and was flooded with an estimated sediment gradient for all parameter models.

After flooding, the resulting models were used as starting model for the next inversion step. In comparison to the first inversion step, I used only the very low frequency content of the data (2-5 Hz). Higher frequencies increase the influence of small-scale structures in the sediments above the target horizon considerably. Therefore, after two iterations the updates already contain many small-scale features making it difficult to pick the horizon. Only for the sea floor high frequencies are usable due to the homogeneity of the water column. After two iterations, the difference plots of all parameters show structures that can be picked, also the v_S model (figure 5.13, right column). In the v_P result, the dominating feature with about 500 m wavelength is the high-velocity/density layer. As the v_S velocities are lower, the wavelength is smaller and the resolution of the high-velocity horizon is better. By looking at the difference plot of the density results, an even higher resolution and more layers than in the velocity models can be observed. Therefore, I recommend to use the density results for picking. An additional test with only acoustic inversion shows similar results for the density inversion. For the picking, the observed unrealistically high updates are rather an advantage than a disadvantage.

From these tests it can be concluded that no elastic modelling is necessary for the picking of the water bottom. The highest resolution is provided by the density model for all horizons. Because a considerable improvement of the density model by using elastic FWI could be shown in the previous section 5.5, I recommend using elastic inversion to generate the parameter models and picking the horizons in the density model.
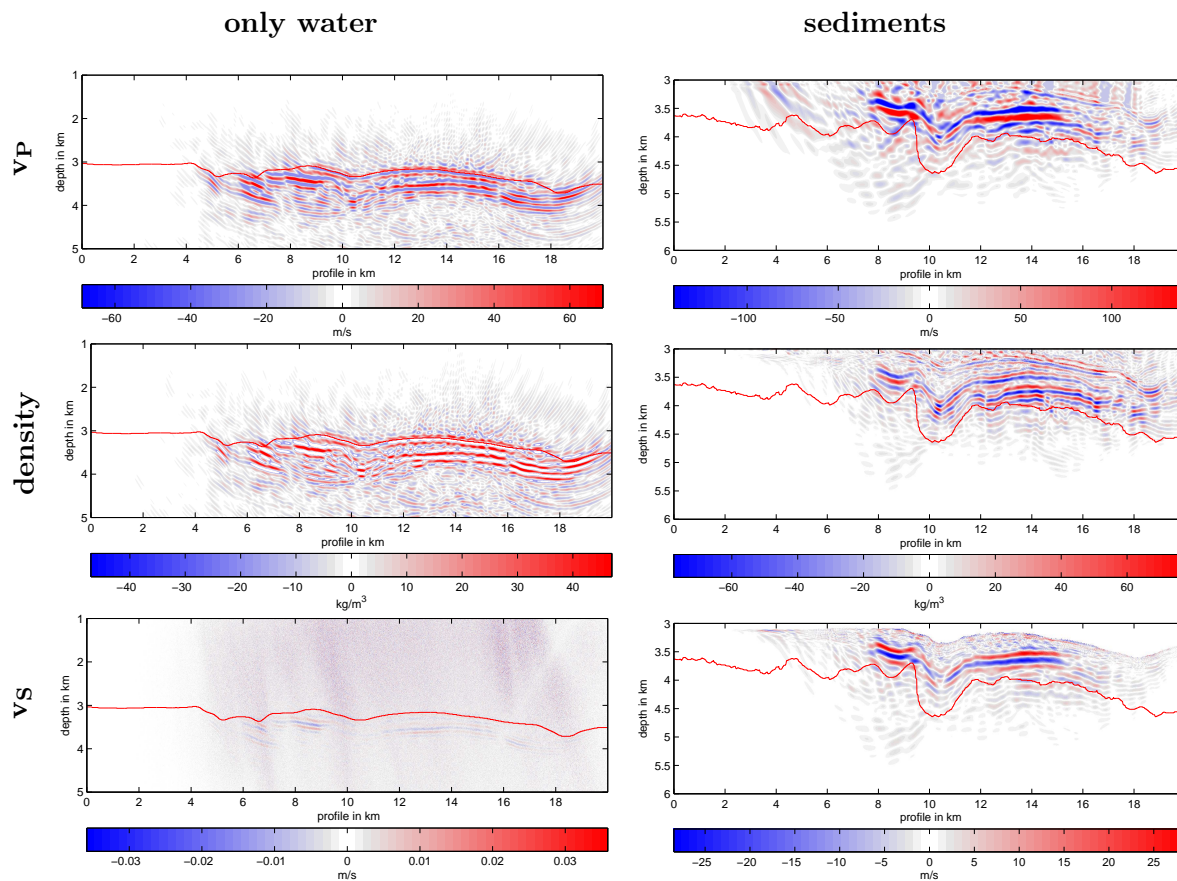
Figure 5.13: Difference plots for three parameter models after elastic inversion. The left column shows inversion results after one iteration using a constant velocity model (water velocity) as starting model. The red line indicates the water bottom in the PGS model. For the inversion results after two iterations in the right column, the starting model contained water and sediments. The red line indicates the top of salt in the PGS model.

5.6   Summary

With the field data tests in this chapter I analysed several parameters of the inversion. In the first test, the influence of the 3D-2D transformation was examined. It showed that the source wavelet inversion is able to compensate most of the effect. Despite this result I decided to apply the 3D-2D transformation. It supports a convergence inside the FWI process. The second set of tests showed the small influence of the long offsets on the inversion result and the significantly better results when using a time window. Thus, the inversion can concentrate on less data leading to a lower misfit.

The subsequent test analysed the influence of a changing number and set of shots. I could show that the used subset of shots with 500 m shot distance is representative and the inversion results do not change by using different shots. Also, a denser sampling of the shot locations did not lead to significantly better results. But due to the significantly higher computational effort, I decided to use the larger (500 m) shot spacing.

For the test of cycle-skipping, the starting model was moved vertically. I could estimate with this test that strong parameter contrasts should be located correctly with less than 100 m location error in the starting model for a frequency content of 2-5 Hz in order to avoid cycle-skipping.

The subsequent test dealt with the influence of using and inverting for a varying number of parameter models. I could show that the best results were achieved by using an elastic approach. In the elastic tests, FWI inverted simultaneously for v_P, v_S and density. With this approach, the misfit could be reduced significantly more than for the acoustic approach. The STF inversion revealed wavelets which are all almost identical to each other, showing the high quality of the inversion results. Even the density model showed realistic features with considerably less detectable artefacts.

The last test in this chapter analysed the question which parameter model is most suitable to pick the horizons. I could show that the density model is the best model to use in combination with an elastic FWI.

Chapter 6

Field data inversion results

The following chapter shows the field data inversion results for acoustic and elastic FWI of the 20 km long model (model 2). For the field data inversion a starting model is generated from the field data themselves. In addition, field data inversion results are presented using the PGS model as starting model.

6.1 Flooded model

6.1.1 Starting model generation

In the following section, I describe the generation of the starting model for the field data. I follow the same steps as shown in section 4.6. In addition, the sea floor is picked. This step is typically not necessary as the water depth is logged during the data acquisition. However, I decided to pick the sea floor to validate the acquisition geometry and the picking of the horizons. All interfaces are picked in *MATLAB* by hand and interpolated between the picked points (see section 4.6 for more details). For every interface, I place 50 to 70 picks.

Sea floor

The sea floor was picked for quality control. Typically, this horizon is well known due to on-site measurements. In this section, the sea floor was recovered from a constant velocity model and the picked horizon compared with the one from the PGS model to ensures the correctness of the used acquisition geometry. For the generation of the sea floor interface I used a starting model with a constant velocity of 1490 $\frac{m}{s}$ for FWI. After two iterations, the resulting updated model was used to pick the sea floor.

In figure 6.1a the inversion result of the density parameter after two iterations in the 2-14 Hz frequency band is shown. As explained in the previous chapter, the frequency filtering during the inversion included also high-frequency parts to allow the highest resolution possible. The

data were windowed to only 1 s after the first reflection or refraction. Despite the artefacts
in the water column, I could clearly identify the sea floor. In the difference plot shown in
figure 6.1b the seabed was picked and interpolated. Figures 6.1c and 6.1d show the v_P model
after flooding below the picked water bottom with a sediment velocity gradient, extracted
from the PGS background model. In addition, the water bottom of the provided model is
plotted as magenta line. The line shows a very good match with the picked interface. Only
on the first 5 km distance (half streamer length) and in the two valleys at about $x = 47$ km
and $x = 59$ km, variations of about 100 m are visible. The reason for this is the insufficient
illumination in these areas of the model. Apart from the three mentioned areas the picking
was successful and the acquisition geometry was also chosen correctly.

Top of salt (TOS)

For picking the TOS, FWI was performed again for two iterations, using the flooded model
shown in figure 6.1c as starting model. The used frequency band was chosen as low as possible
(maximum frequency of 5 Hz) to avoid a large influence by small-scaling structures in the
sediment. I limited the inversion to a dynamic time window starting at the first break of the
first reflection and refraction and ending after 2 s. The inversion result of the density model is
shown in figure 6.2a. Clear structures are visible. For better visualisation the difference of the
starting model and the inverted model is generated (figure 6.2b). Please note that not only
the TOS is visible, but also additional layered structures in the sediments above the TOS.
Nevertheless, I was able to pick the TOS.

One of the reasons for the high-amplitude structures in the sediment occurring after only two
iterations is a high-reflectivity layer already visible in the migration result. In depths of three
to four kilometres, sediment layers from the Cretaceous can have velocities similar to salt or
even higher (Faust, 1951). Therefore, these layers can generate high-amplitude reflections,
having a large influence on FWI. As the layers are thin and not continuous they are difficult
to pick and it is difficult to include them in the starting model. Thus, the only possibility is
to pick the top of salt roughly and smooth the flooded velocity model. The smoothing allows
FWI to apply corrections to the TOS and include the sediment structures in the model.

The high updates in the difference plot in the first kilometre below the sea floor are produced
by structures in the sediments. The clear drop of updates below the area of high amplitudes
is produced by the high impedance interface between the sediments and salt. Therefore, the
TOS was picked in the difference plot below the distinctive drop in amplitude. The picked
line can be seen in figure 6.2b and the flooded model in figure 6.2c. For comparison, the TOS
of the PGS model is also displayed. The picked TOS and the TOS of the PGS model (plotted
in green) show a good match except for the first 5 km and valleys at about $x = 42, 52, 68$ km
(indicated by arrows), where the picked horizon differs up to 200 m compared to the PGS
model. Which line is more accurate cannot be said at this stage. Thus, during inversion these
areas of the model need to be monitored carefully.
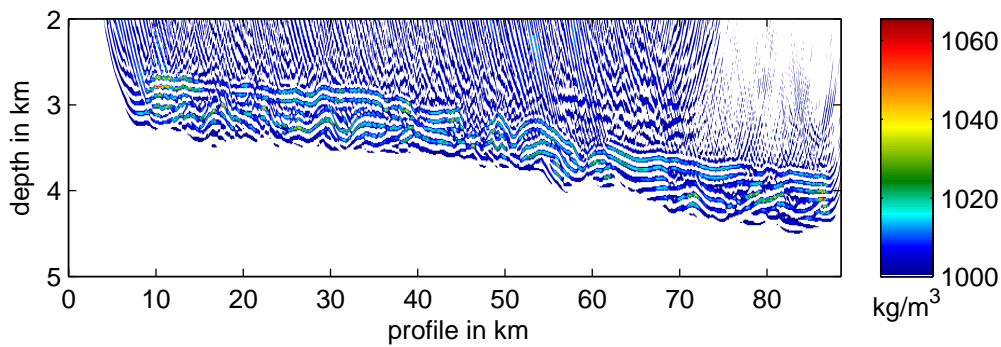
(a) Density inversion result after two iterations using a constant velocity starting model. White areas indicating the value of the starting model ($1000 \frac{\text{kg}}{\text{m}^3}$), other colours show updates.
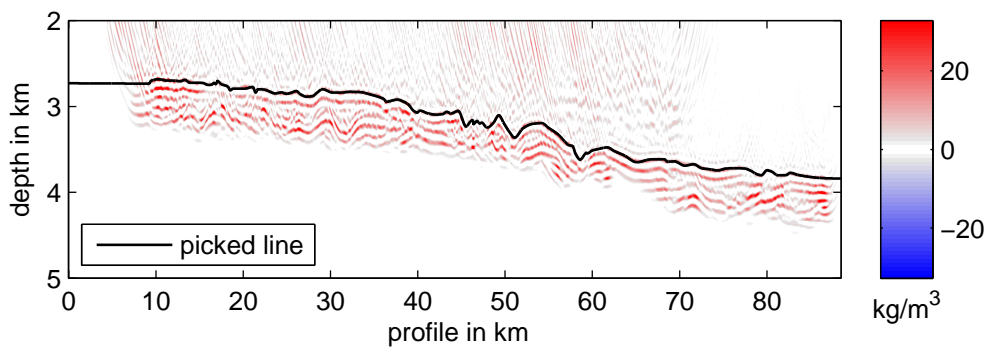
(b) Difference plot of density inversion result minus starting model.
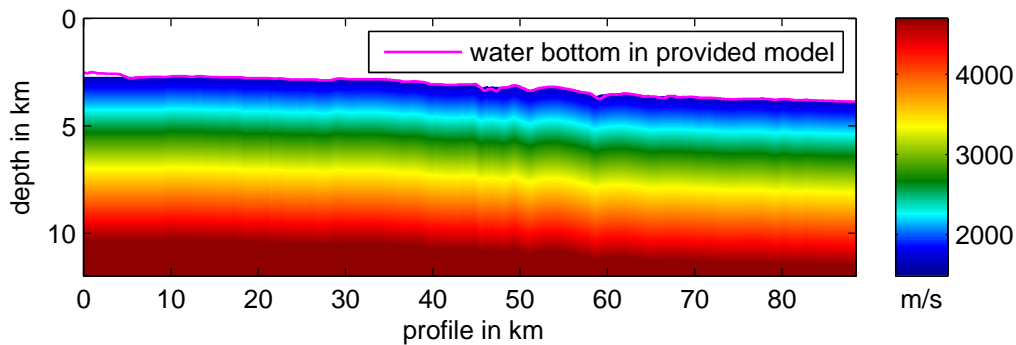
(c) v_P model after flooding with sediment gradient below the picked water bottom. For comparison, the location of the water bottom in the provided PGS model is plotted as magenta line.
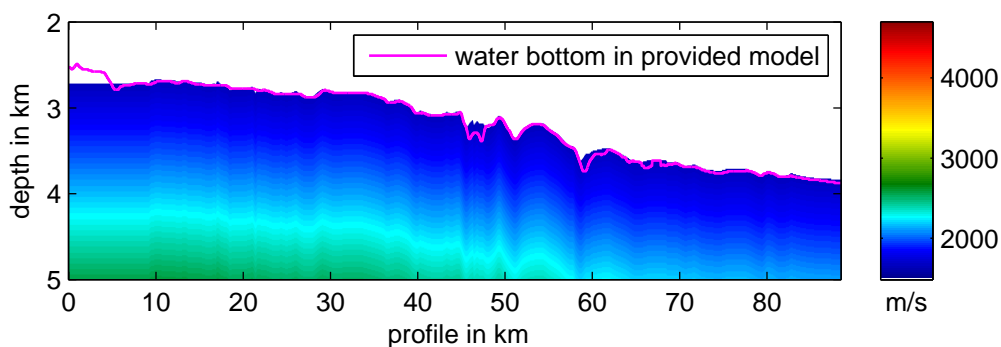
(d) Zoom of v_P model shown in figure 6.1c.

Figure 6.1: Picking of the seabed and flooding underneath for model 3 after field data inversion.
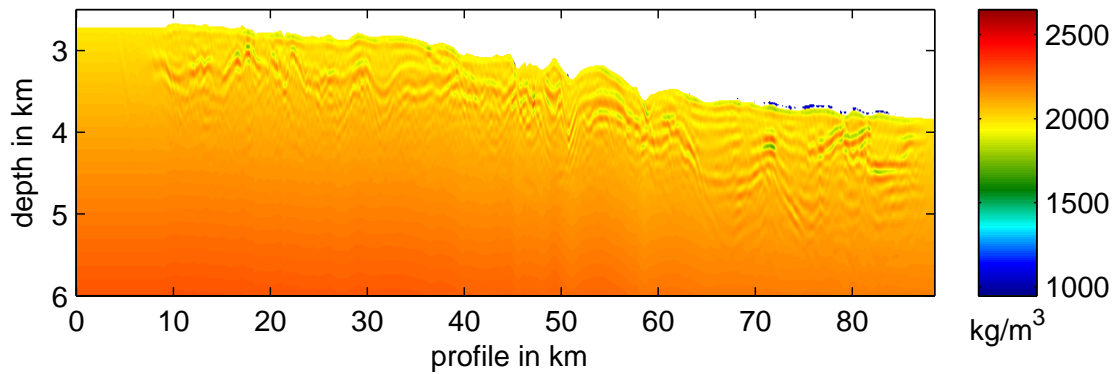
(a) Density inversion result after two iterations using the model shown in figure 6.1c as starting model. In white, the starting density of 1000 $\frac{\text{kg}}{\text{m}^3}$ or lower is plotted. All other colours indicate an updated higher density.
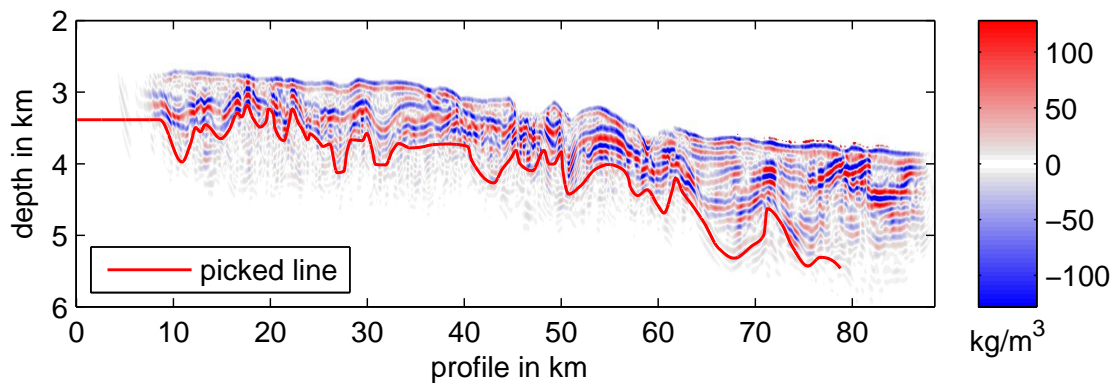
(b) Difference plot of density inversion result minus starting model.
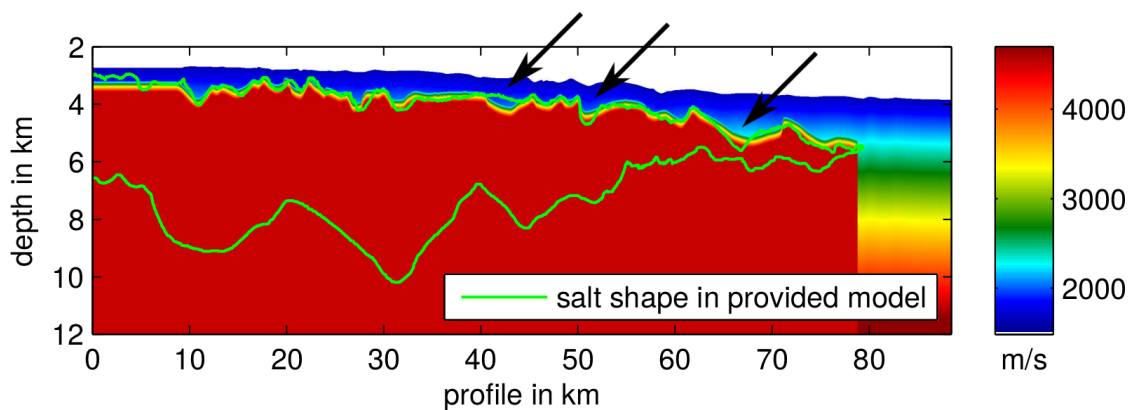
(c) v_P model with flooded salt velocity below the picked top of salt. The arrows indicate areas of large differences between the picked interface and the interface in the PGS model.

Figure 6.2: Picking of the top of salt and flooding underneath for model 3 after field data inversion.

Bottom of salt (BOS)

The bottom of salt is located between 6 km and 10 km depth. The inversion primarily updates the shallower part of the model first due to the comparatively higher amplitudes of the events from shallow structures compared to events from deeper parts of the model. Therefore, at least 10 iterations were necessary to be able to pick the bottom of the salt body. Again, I used as few iterations as possible to avoid artefacts due to an insufficient starting model. The frequency content was also limited to low frequencies (2-5 Hz) to avoid the influence of smaller structures as best as possible. I windowed data from the first reflection/refraction up to 12 s. A smaller and later time window, concentrating on the later events, turned out impractical due to the large depth range of the target area between 5 km and 10 km.

The inversion result after 10 iterations can be seen in figure 6.3a. Most of the updates are visible in the upper part of the model, as expected. In the inversion result, almost no updates are visible in the target area. In the difference plot in figure 6.3b, higher amplitude areas and continuous structures can be identified among the noise in the updates. Due to the knowledge of the extent and shape of the salt body from the PGS model, I was able to pick the approximated depth of the BOS. Without the a priori knowledge, no picking would have been possible with the flooding method. The picked line is plotted in red.

The result after flooding below the picked interface with a sediment gradient is plotted in figure 6.3c. By comparing the model with the green line representing the contour of the salt body in the PGS model, a partial conformance is visible. But still, the location differences are up to 1 km in the deeper parts, for example at $x = 10$ km, where the picked BOS line is shallower than the one from the PGS model.

In summary, I was able to produce a starting model with only little information about the salt body. The picked seabed and the seabed in the PGS model show a high conformance with only little differences. Also the picked salt interfaces and the salt contour in the PGS model match, but with considerably higher location differences, especially for the BOS. The location differences are the result of the complex overburden above the salt body and the low reflection coefficient for the BOS. However, the flooded model including the smoothed salt interfaces is used in the following section as starting model for inversion. The results will show, if the flooded model is sufficient as starting model for FWI.

6.1.2   Acoustic results

After the creation of the starting model, the next step is the actual inversion. As the elastic inversion requires much more computational cost, I decided to use a smaller model. For better comparison, the acoustic inversions also use the smaller model as starting model. Model 3 (see section 3.2 for more details), used in the following inversions, is 20 km long and 8 km deep. It represents a subpart of the flooded model constructed in the previous section. The starting model is shown in figure 6.4a. The red stars indicate the shot positions and the 10 km streamer is located on the left side of each shot.
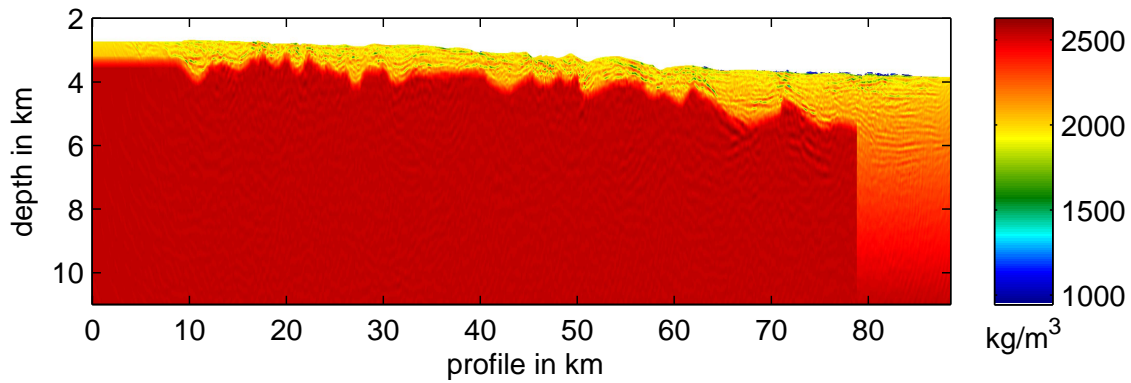
(a) Density inversion result after 10 iterations using model in figure 6.2c as starting model.
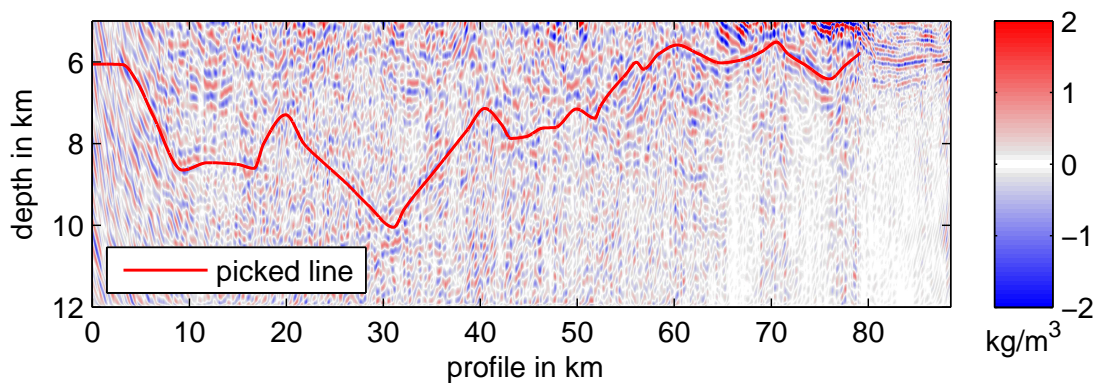
(b) Difference plot of density inversion result minus starting model.
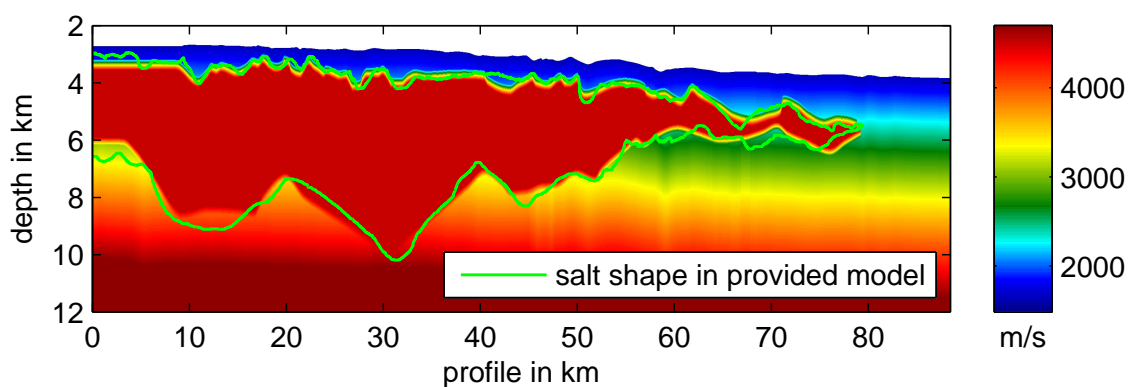
(c) v_P model with flooded sediment velocity gradient below the picked bottom of salt.

Figure 6.3: Picking of the bottom of salt and flooding underneath for model 3 after field data inversion.

The inversion result after 100 iterations of acoustic inversion is shown in figure 6.4. The update in the v_P model (figure 6.4b) shows an increase of the velocity in the sediment layer below the profile. The velocity is increased by almost 500 $\frac{m}{s}$. Especially at the boundary zone of the salt, the velocity is increased to salt velocity. This is the beginning of correcting the shape of the salt. The smoothed sediment-salt interface is necessary to enable a sufficient correction of the velocity during FWI. Several tests without the smoothing of the model, not shown in this work, support the necessity of smoothing high-contrast interfaces.

In the density model in figure 6.4c similar high-contrast updates in the sediment layer can be observed. In most areas of the sediments, contrasts of up to 1000 $\frac{kg}{m^3}$ in less than 100 m are visible. These large contrasts cannot be explained by geological formations. In addition, these updates are not layer, as the reflection image in figure 3.5a indicates. Therefore, most of the updates are classified as artefacts. The high-velocity layer in the sediments is not visible. The data fit in figure 6.4e decreases after 40 iterations down to a minimum value of 75 % of the initial misfit, but increases again to 82 % at the last iteration. This diverging of the inversion is an indicator for an insufficient starting model or other physical effects, which cannot be explained by the modelling and inversion. A partial increase of the misfit value is possible due to implementation of the step length estimation and the given minimum number of iterations per frequency (see section 2.2.6). In the inverted STFs (figure 6.4f) only the source wavelets of shots 5-15 are similar. All STFs for other shots differ clearly. For example, shot 18 and 19 have a later first break and inverted polarity, whereas shot 4 has a totally different appearance than the other shots. These disparities in the STFs are indicators for an unsuccessful inversion and unreliable results. This suspicion is supported by the poor adaption of the waveforms of the field data and inverted data, shown in figure 6.4e, already indicated by the large misfit values. Especially the amplitudes of the trace in the mid-offset range show a poor adaption. Also a comparison of the full seismograms in figure 6.4g and 6.4h can confirm this. The poor adaption can be the results of elastic effects not explained by the acoustic approximation.

6.1.3   Elastic results

Due to the unsuccessful acoustic inversion, elastic FWI was utilised. I limited the maximum frequency to 10 Hz for the elastic inversion. This frequency is lower than in the acoustic case due the stability criterion (section 2.1.2), even the data and model had to be resampled in space to a grid distance of 6.25 m and in time to 0.6 ms.

The results of the elastic inversion using the flooded model are displayed in figure 6.5. The inversion behaves much better than for the acoustic inversion. The most obvious difference is the misfit behaviour in figure 6.5d. A constant decrease (beside local exceptions) can be observed down to a misfit of about 50 % of the initial value after 68 iterations. The data fit in figure 6.5e shows a much better fit of the waveforms than for the acoustic inversion. The same can be observed by comparing the full seismograms in figure 6.5g and 6.5h. All main events shown in the field data are also visible in the modelled data. Also, the amplitudes of the events are comparable. The STFs appear much more similar than for the acoustic inversion.
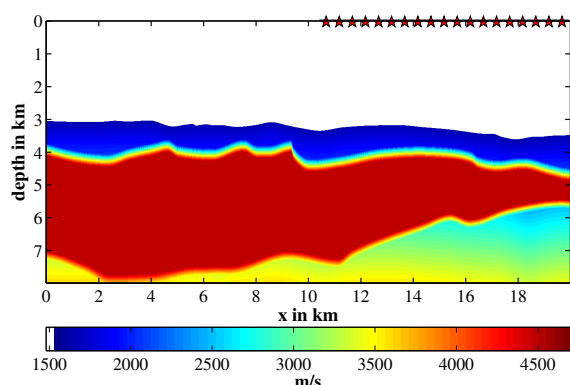
(a) v_P starting model. The red stars indicate the shot positions with the streamer located left of each position.
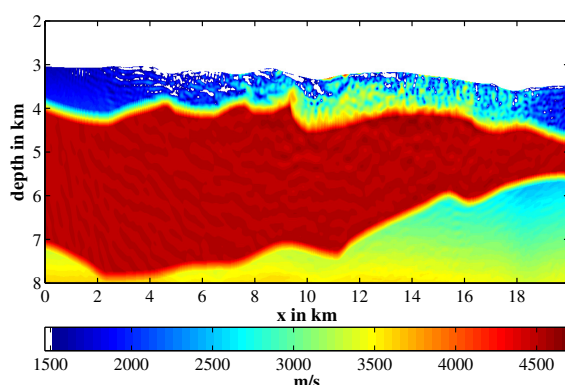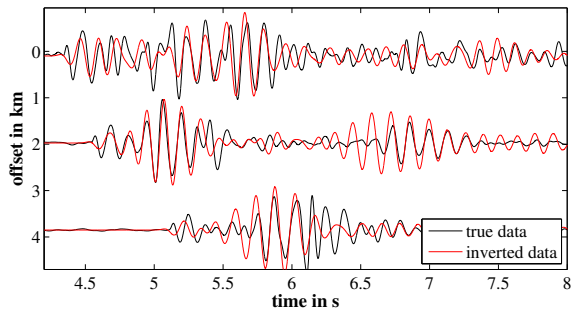

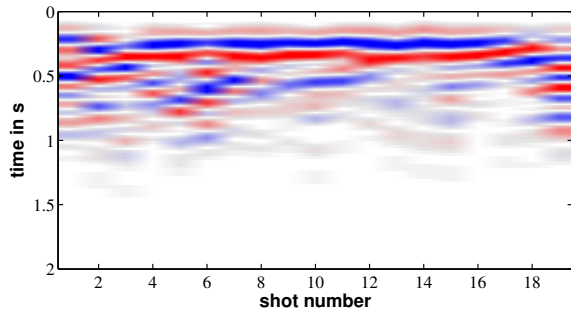(b) v_P inversion result.
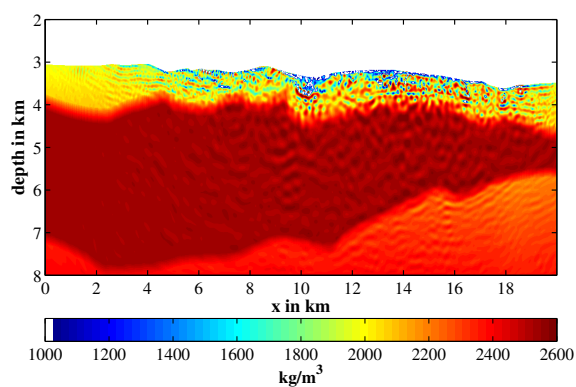
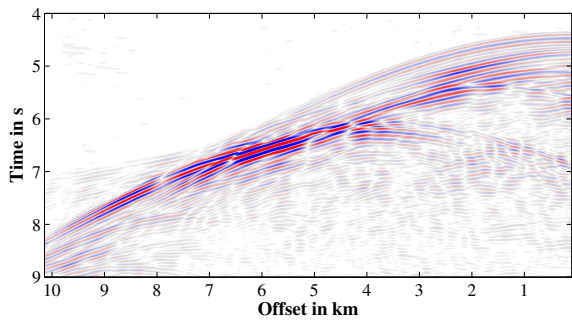(c) Density inversion result.
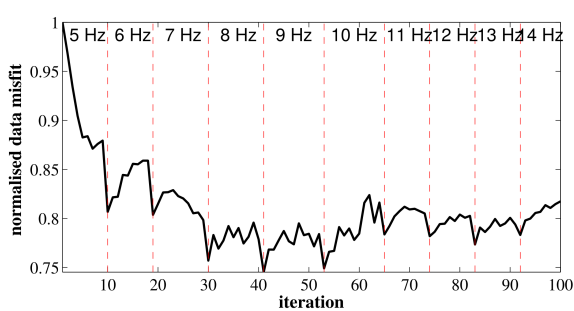
(d) Misfit development during inversion.
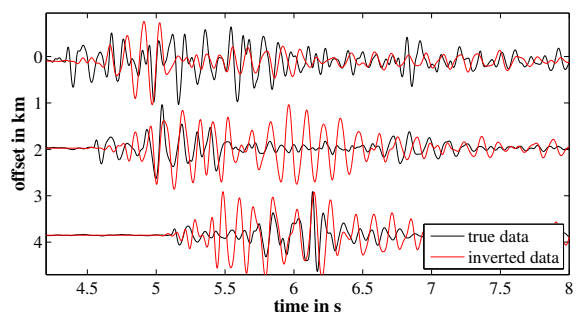
(e) Data fit of selected traces (shot 7) at 14 Hz maximum frequency.
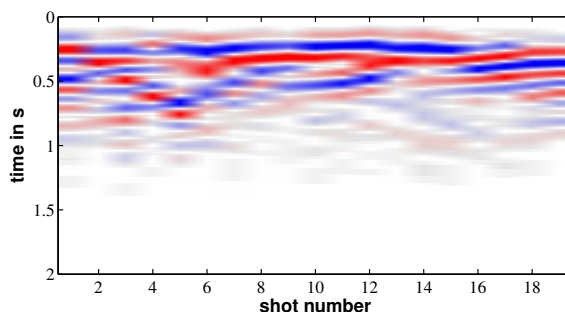
(f) STF inversion result at last frequency step.
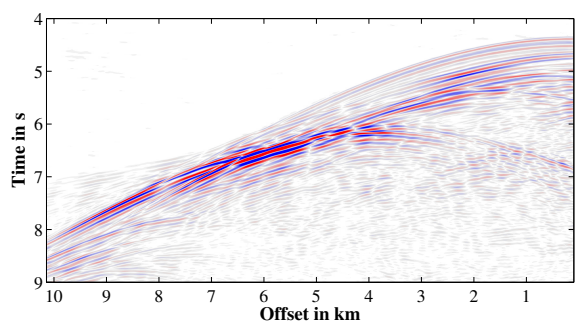
(g) Field data low-pass filtered to 14 Hz.
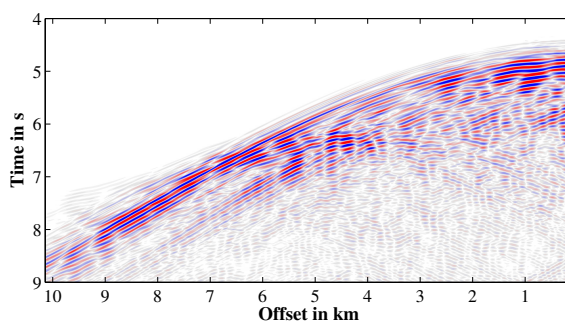
(h) Modelled data low-pass filtered to 14 Hz.

Figure 6.4: Acoustic inversion results after 100 iterations using the flooded model as starting model.

The only exceptions are the first and last three shots. Their appearance change in comparison to all other shots. This indicates remaining local insufficiencies in the starting model.

The v_S model is not plotted because it contains no visible updates due to the usage of only pressure data (Raknes and Arntsen, 2014). The inversion results of the v_P and density models show significantly less artefacts compared to the acoustic results. No extreme contrasts are visible and the values appear geologically reasonable by comparing them with values from literature (see table 3.1). Layered structures start to appear in both parameter models. But the high-reflection layer, visible in the migrations results, does not appear.
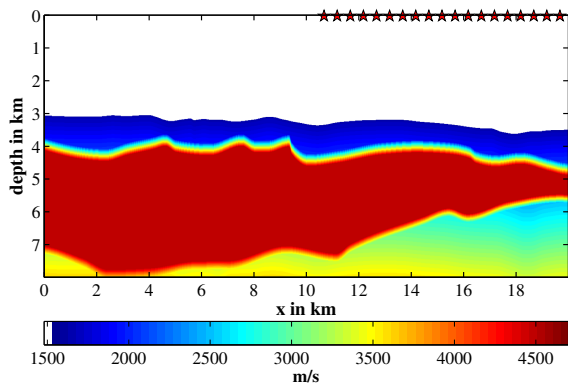
(a) v_P starting model. The red stars indicate the shot positions with the streamer located left of each position.
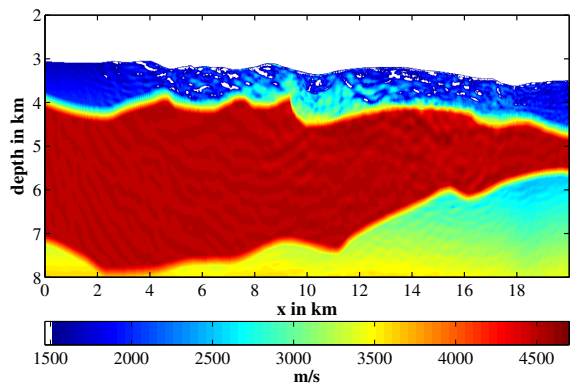
(b) v_P inversion result.
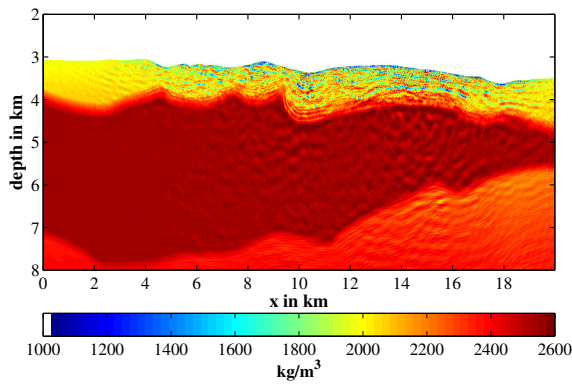
(c) Density inversion result.
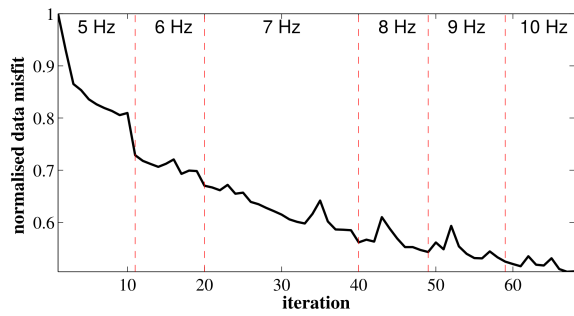
(d) Misfit development during inversion.

(e) Data fit of selected traces (shot 7) at 10 Hz maximum frequency.

(f) STF inversion result at last frequency step.

(g) Field data low-pass filtered to 10 Hz.
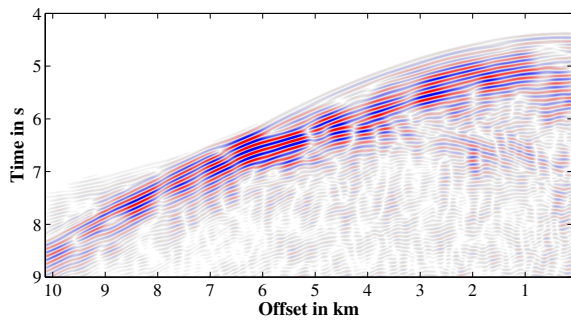
(h) Modelled data low-pass filtered to 10 Hz.

Figure 6.5: Elastic inversion results after 68 iterations, using the flooded model as starting model.

6.2 PGS model

6.2.1 Acoustic results

The starting model of the v_P-component of the acoustic FWI is shown in figure 6.6a. The source positions are indicated by red stars. The streamer is located to the left of each shot and moves with the shot from left to right.

The inversion results are plotted in figure 6.6b and 6.6c. The inversion was able to reduce the data misfit by 20 % in 98 iterations, up to a frequency of 14 Hz. From the development of the misfit curve it can be noticed that the misfit was clearly reduced during the first frequency stage and the minimum misfit is already reached after the change to the second frequency stage. However, after including frequencies up to 6 Hz the misfit starts to increase. Then, after changing to 7 Hz, the misfit value drops again. This unusual behaviour indicates that the inversion is unable to find an update reducing the data misfit. The reason for this can be explained by an attempt of the inversion trying to explain elastic data with acoustic modelling. Therefore, especially for acoustic FWI, the inversion results need to be interpreted carefully because the models can include artefacts.

The inversion results of the v_P model and the density model are plotted in figure 6.6b-6.6c. In the next chapter, the density and v_P results are plotted enlarged including marked structures (figure 7.1a and 7.2a). The inversion of the v_P parameter updated only long-wavelength structures in the sediment layer above the salt. Above the valley in the middle of the TOS, a lower velocity valley is visible and higher-velocity layers below. The density model shows more detailed structures in the sediments. On the right side of the valley, a high-density layer was included above the salt. Above the valley of the TOS, two well defined high-density layers were added. Layered structures are also visible on the left side of the valley. The updates seem to be blocky, why they are interpreted as artefacts. Also, the contrasts between the low- and high-density structures are very high with partial almost 1000 $\frac{kg}{m^3}$ difference within a few hundred metres. This can be explained by the acoustic approximation and the attempt of the inversion to fit amplitudes of the elastic data. If inverted structures are visible over several shot distances, they were influenced and built up by multiple shots. Therefore, they can be interpreted as reasonable structures. As the high-velocity/density layers in this inversion result are continuous throughout the model, they are defined as reasonable and they are not interpreted as artefacts.

In order to evaluate the results, the data fit is plotted in figure 6.6e. Some of the main events could be fitted, but still most events could not, neither in phase nor in amplitude. The same can be seen by comparing the field data and the modelled shot gather in figure 6.6g and 6.6h. Only the main events were fitted. A comparison of the results of the STF inversion (figure 6.6f) shows also large differences. Especially in the middle, the STF inversion results differ strongly from each other. These differences indicate insufficiencies in the starting model.
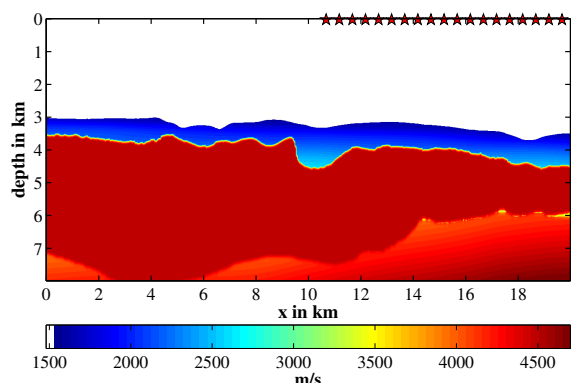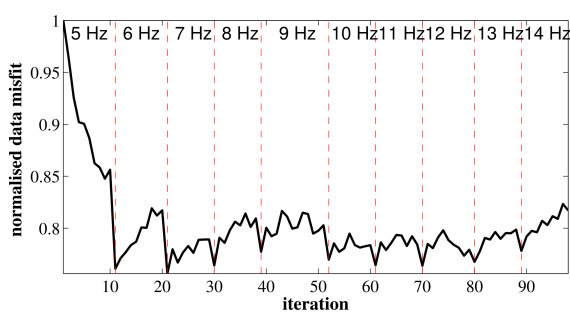
(a) v_P starting model. The red stars indicate the shot positions with the streamer located left of each position.
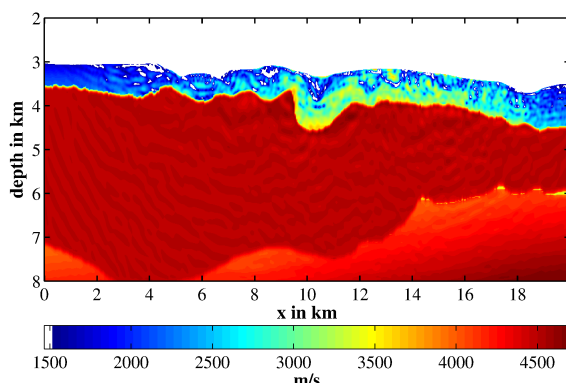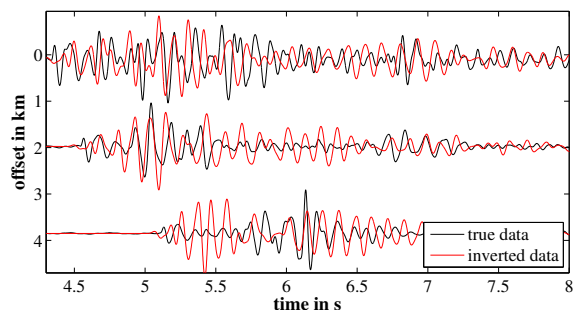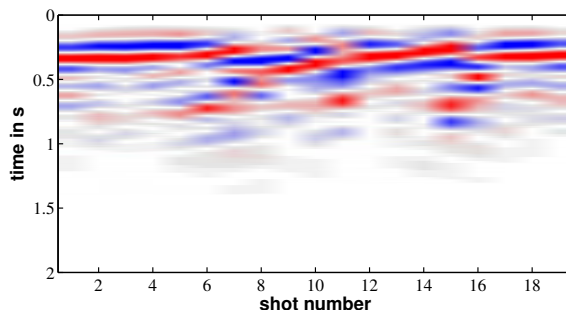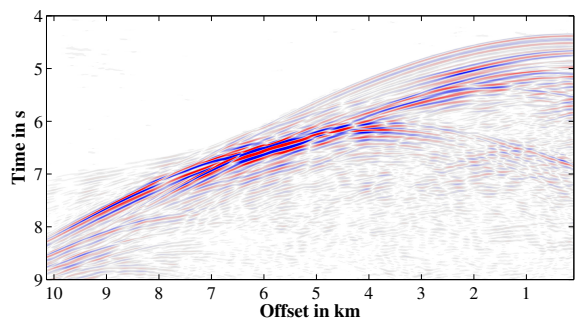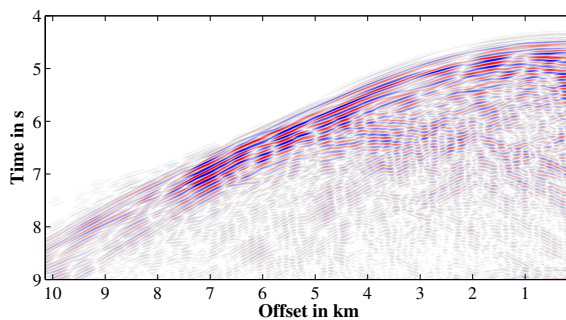

(b) v_P inversion result.
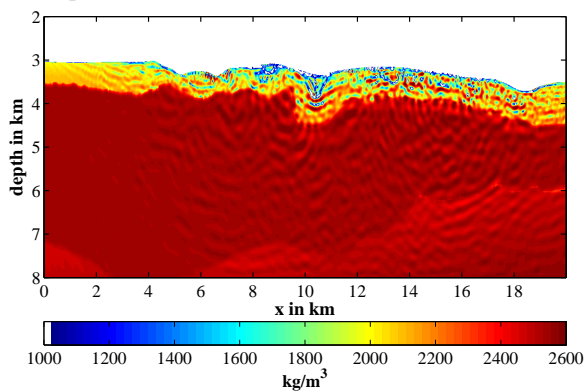
(c) Density inversion result.

(d) Misfit development during inversion.

(e) Data fit of selected traces (shot 7) at 14 Hz maximum frequency.

(f) STF inversion result at last frequency step.

(g) Field data low-pass filtered to 14 Hz.

(h) Modelled data low-pass filtered to 14 Hz.

Figure 6.6: Acoustic inversion results after 98 iterations, using the PGS model as starting model.

For the acoustic FWI I was able to perform an inversion using the 88.5 km long model for 33 iterations. More iterations were not possible due to the available computational resources. The results are shown in figure 6.7. As starting model, a smoothed version of the PGS model was used to avoid artefacts due to location errors of the salt body. A labelled version of the density and v_P results are plotted in figure 7.3. The quality is similar to the results of the 20 km-long model in figure 6.6. The high-velocity/density layer is visible directly above the salt for most of the salt bodies extent. Also at about $x = 80$ km and a depth of 4 km, well defined dipping structures appear in the sediments. However, also various artefacts are visible in both models indicated by the monitoring factors. For example, the misfit (figure 6.7d) reaches the minimum of about 75 % of the initial misfit after 19 iterations. After that the misfit increases up to about 82 % after 33 iterations. In the plot of the data fit for the given maximum frequency of about 8 Hz in figure 6.7e the fitting of the main phases can be observed. But especially for the longer offsets, the amplitudes of events after the large reflection of the salt (indicated by the arrow) are too high compared to the field data. Also the STFs displayed in figure 6.7f are only partially equal to each other. Even phase changes are visible.

Over all, the acoustic inversion was possible, but the resulting parameter models contain several artefacts, often overlaying inverted structures. The resulting v_P parameter model of the acoustic inversion shows only long-wavelength structures. The density results show well defined high-density layers above the top of salt, interspersed with small-scale artefacts. In the results it is difficult to distinguish between artefacts and structures.

6.2.2 Elastic results

As already mentioned in section 6.1.3, I limited the maximum frequency to 10 Hz for the elastic inversion. This frequency is lower than in the acoustic case due the stability criterion (section 2.1.2), even the data and model had to be resampled in space to a grid distance of 6.25 m and in time to 0.6 ms.

The results of the elastic inversion after 89 iterations (up to 10 Hz) of the v_P and density component are shown in figure 6.8b-6.8c. In the next chapter, the density and v_P results are plotted enlarged including marked structures (figure 7.1c and 7.2c). The v_S result is not shown as it contains no visible updates. The reason for this is that almost no S-waves are back-converted into P-waves at the seabed to reach the receivers as converted P-waves (see section 5.5.1) and due to the usage of only pressure data. Again, the density update is most detailed in the sediment area above the salt. Various high-density layers were added to the starting model, following roughly the topography of the salt. Some small-scale horizontal artefacts are visible, caused by the acquisition geometry. The application of horizontal filtering of the gradients had no positive effect on the result. Therefore, I decided not to use the filter.

After all iterations the inversion was able to reduce the misfit by almost 60 % (figure 6.8d). In order to evaluate the quality of the result, the data fit of selected models, the STF inversion results and the comparison of the field and inverted data are plotted (figure 6.8e–6.8h). For the data fit, three traces are plotted for a near, middle and far offset, respectively. In black,
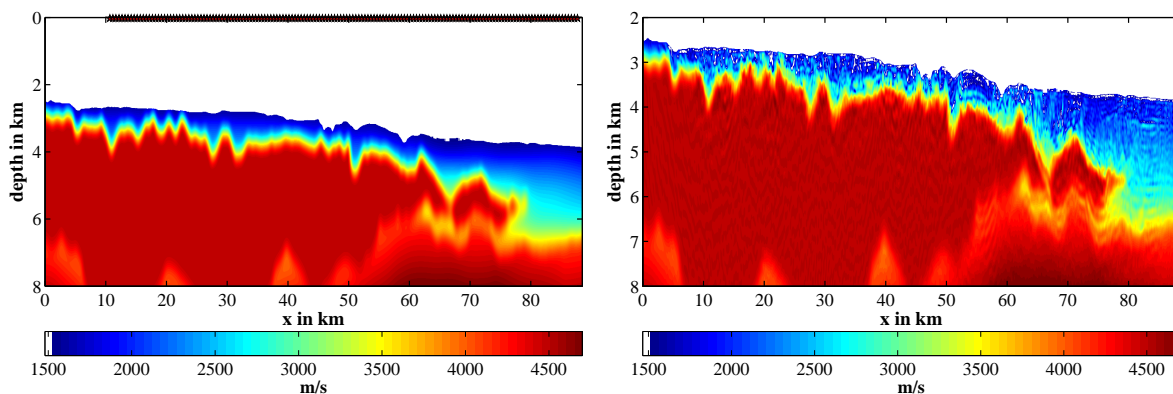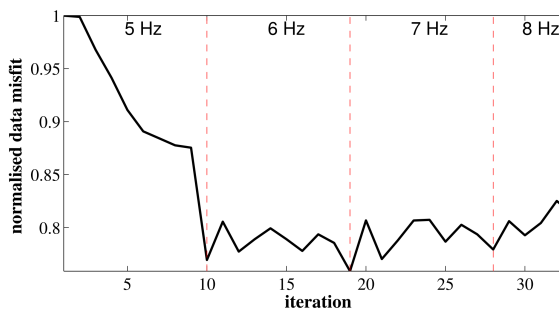
(a) v_P starting model. The red stars indicate the shot positions with the streamer located left of each position.
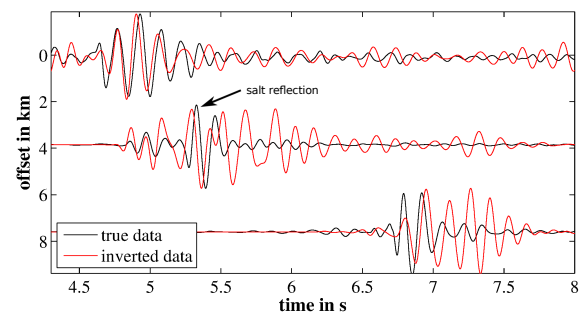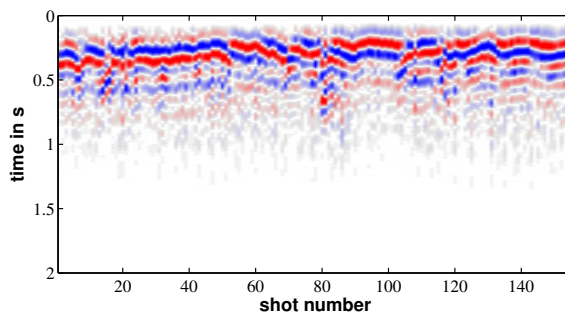
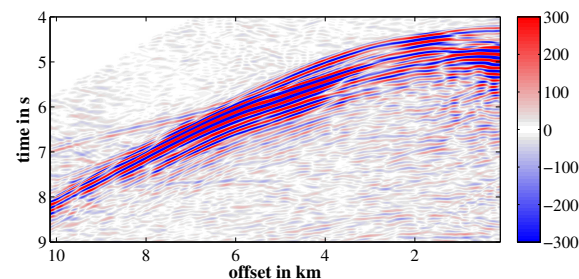(b) v_P inversion result.
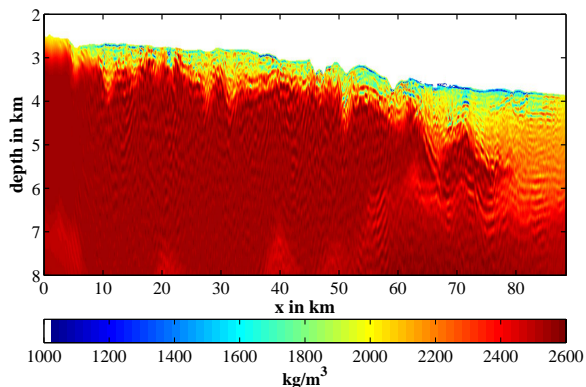
(c) Density inversion result.

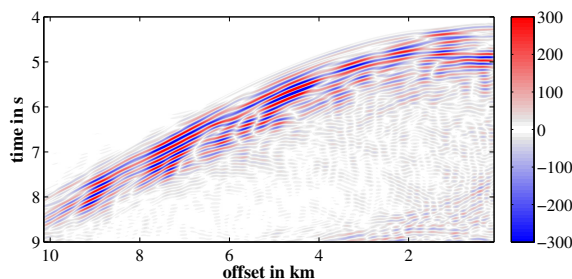(d) Misfit development during inversion.

(e) Data fit of selected traces (shot 61) at 8 Hz maximum frequency.

(f) STF inversion result at last frequency step.

(g) Field data low-pass filtered to 8 Hz.

(h) Inverted low-pass filtered to 8 Hz.

Figure 6.7: Acoustic inversion results after 33 iterations, using the PGS model as starting model.

the true data filtered to the corresponding frequency are plotted, overlain by the inverted traces. The main events could be fitted in phase and amplitude. Also, the STF inversion results show a consistent behaviour for all shots. No phase changes can be observed. Only the 10th shot seems to be shifted down by about 0.05 s. The synthetic data could be fitted very well to the field data (figure 6.8g and 6.8h). All main phases match well in phase as well as in amplitude.

All in all, it can be concluded that the elastic inversion using the PGS model as starting model was successful and the results are reasonable.

6.2.3 Development and comparison of acoustic and elastic FWI

In this section, the development of the acoustic and elastic inversions are displayed for selected iterations. Figure 6.9 (first row) shows the acoustic inversion result of the v_P model after 10 iterations. This belongs to the end of the frequency stage of 2-5 Hz, shown in the bars on the right. The following two rows show the inversion result after 51 iterations (2-9 Hz frequency content) and 98 iterations (2-14 Hz frequency content). In addition, the corresponding shot gathers of the field data and modelled data are plotted with the associated frequency content. During the inversion, the misfit (bar on the left side) is reduced by lifting the velocities above the TOS layer up to more than 3000 $\frac{m}{s}$, interspersed with several artefacts. But already in the lowest frequency stage shown here, layered structures can be seen in the sediments, overlayed by artefacts in the results of later iterations.

In figure 6.10, three substages of the elastic FWI are shown. The first row represent the v_P inversion result after 17 iterations (2-5 Hz frequency content), followed by the inversion result after 49 iterations (2-7 Hz frequency content) and in the last row after 89 iterations (2-10 Hz frequency content). The misfit is reduced to much lower values, as already described in the last sections. Also, in the elastic inversion, the main features are already visible after the first frequency step. But in this case, the velocities are only lifted to about 2700 $\frac{m}{s}$ and no obvious artefacts are introduced by using higher frequencies. The differences of the three inversion stages are very small and are limited to a sharpening of the layers in the sediment and a further lifting of the velocities directly above the salt by $50 - 100$ $\frac{m}{s}$.

In figure 6.11 I show the development of the density model for the acoustic (figure 6.11a) and elastic (figure 6.11b) FWI. For the acoustic inversion a similar behaviour as for the velocity model can be observed: in the first frequency stage, several layers are already visible in the sediments with a very high contrast of almost 1000 $\frac{kg}{m^3}$ within 100 m. Also for higher frequencies, several artefacts are introduced in the model, covering the structures in the sediments.

Also, for the elastic FWI, the density inversion result in the lowest frequency stage already shows several layers. In the subsequent increase of the frequency content, the layers become sharper. The contrast between the layers in the sediment is with about 600 $\frac{kg}{m^3}$ much lower than for the acoustic inversion result.
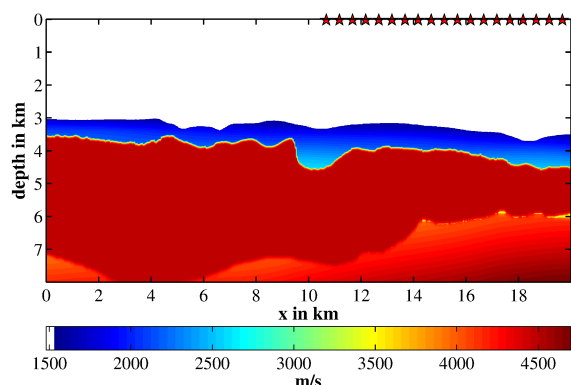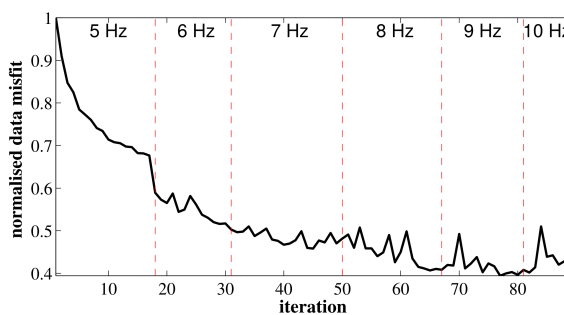
(a) v_P starting model. The red stars indicate the shot positions with the streamer located left of each position.
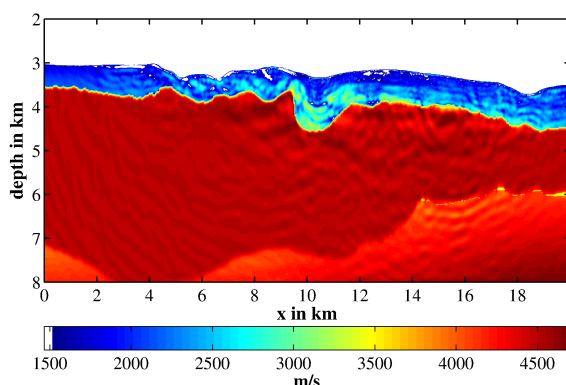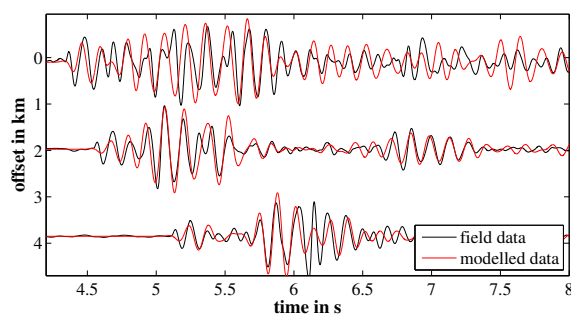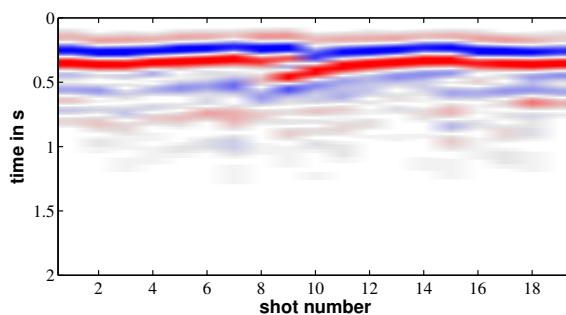
(b) v_P inversion result.
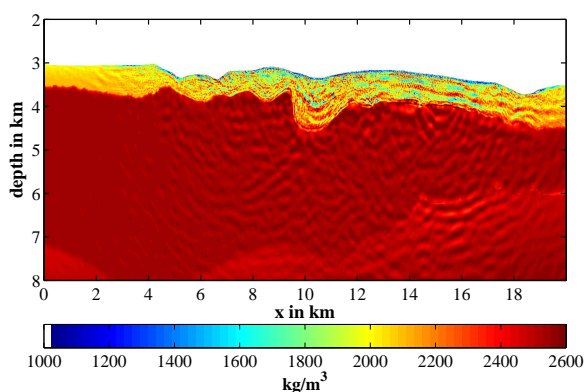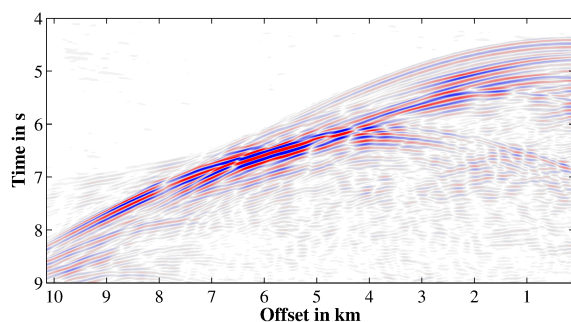
(c) Density inversion result.

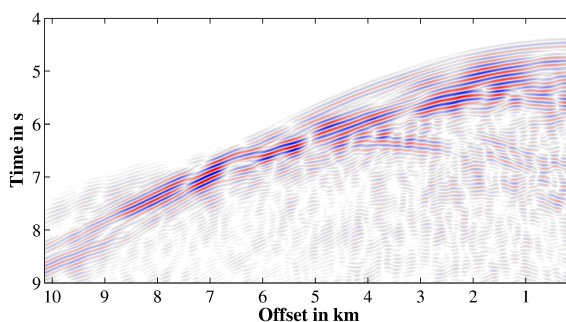**(d)** Misfit development during inversion.

(e) Data fit of selected traces (shot 7) at 10 Hz maximum frequency.

(f) STF inversion result at last frequency step.

(g) Field data low-pass filtered to 10 Hz.

(h) Modelled data low-pass filtered to 10 Hz.

Figure 6.8: Elastic inversion results after 89 iterations, using the PGS model as starting model.

The plots show that already with the low frequency content a good resolution can be achieved. The density update shows several continuous high-density layers. In comparison with the acoustic inversion, the elastic inversion does not introduce artefacts for higher frequencies and shows a considerably lower misfit. Besides the lower parameter contrasts in the sediments of the parameter models of the elastic inversion results, also clearly more details are present in the density update.

6.3 Summary

The inversion results shown in this chapter indicate the clear advantage of elastic FWI for this data set and the great potential of the density model to detect structures in the subsurface. The L_2-norm could be reduced considerably better in the elastic case and the models reveal much more details. In the acoustic inversion, the inverted structures were covered by artefacts when increasing the frequency content. As the elastic inversion results do not show these artefacts, they can be explained by elastic effects, which are not taken into account by the acoustic modelling.

A second finding of this chapter is that the use of the flooded model as starting model produces inversion results with a lower resolution and less interpretable inverted structures in the models. The differences in the shot domain for all four tests are displayed in the following chapter. The best conformity with the field data is given for the elastically inverted data using the PGS model as starting model. Therefore, I do not recommend the presented flooding technique for this deep-water data set including a salt layer. It may work better for other data sets.
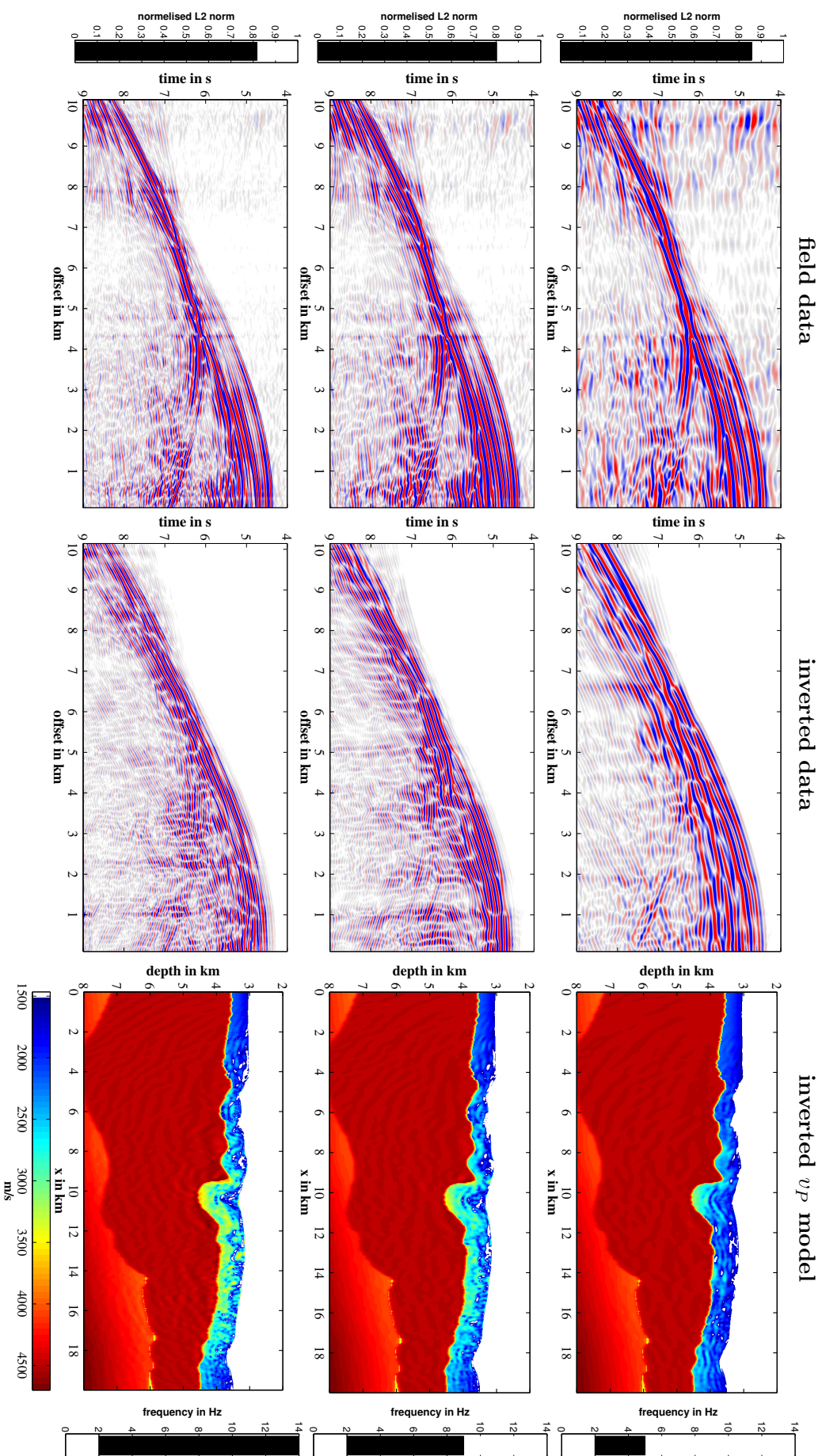
Figure 6.9: Development of acoustic FWI using the 20 km-long PGS model as starting model. The shot gathers are trace-normalised. First row: result after 10 iterations; second row: result after 51 iterations; third row: result after 98 iterations. The L_2-norm misfit and the frequency stage are shown as bars on the left and right.
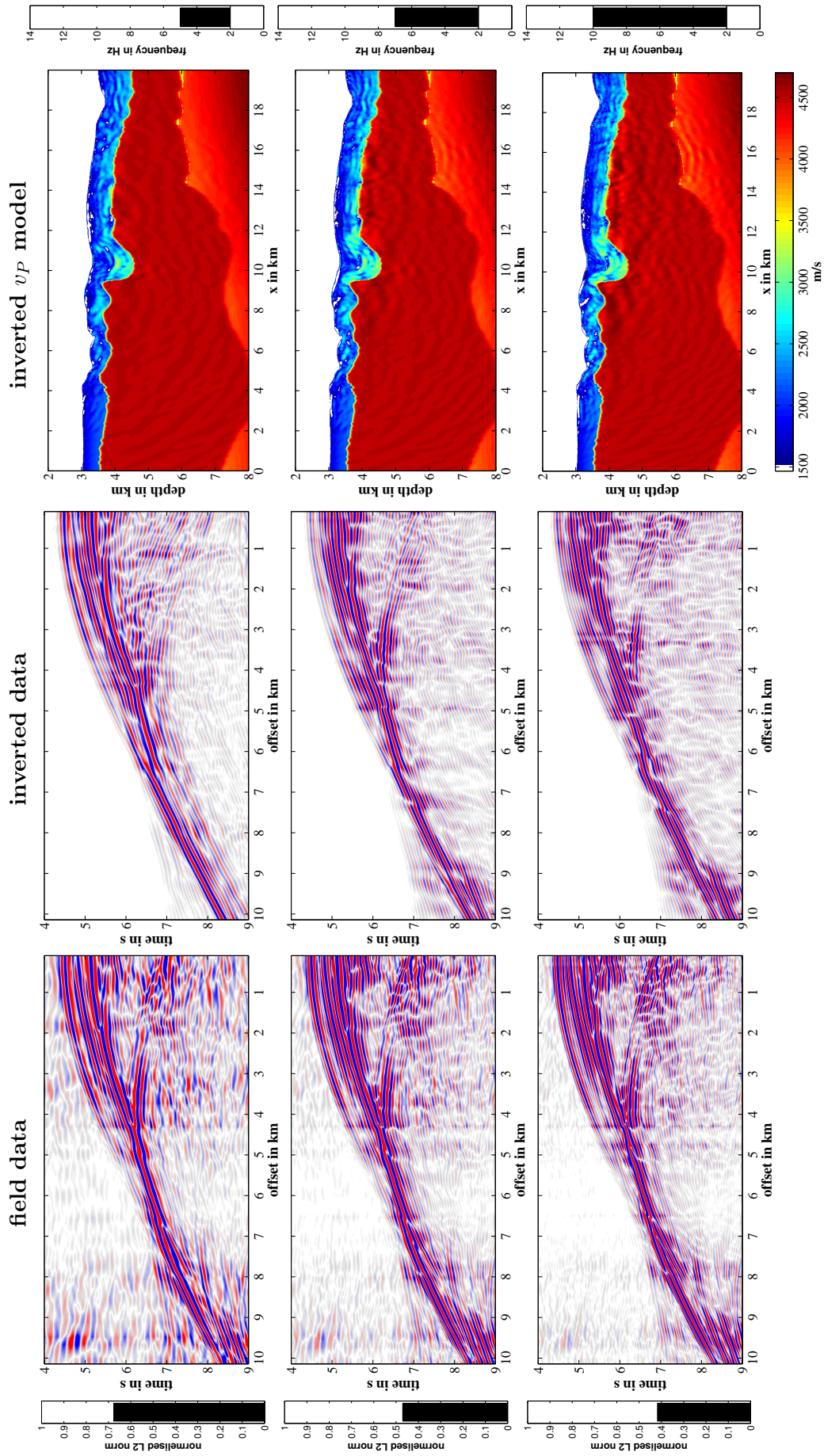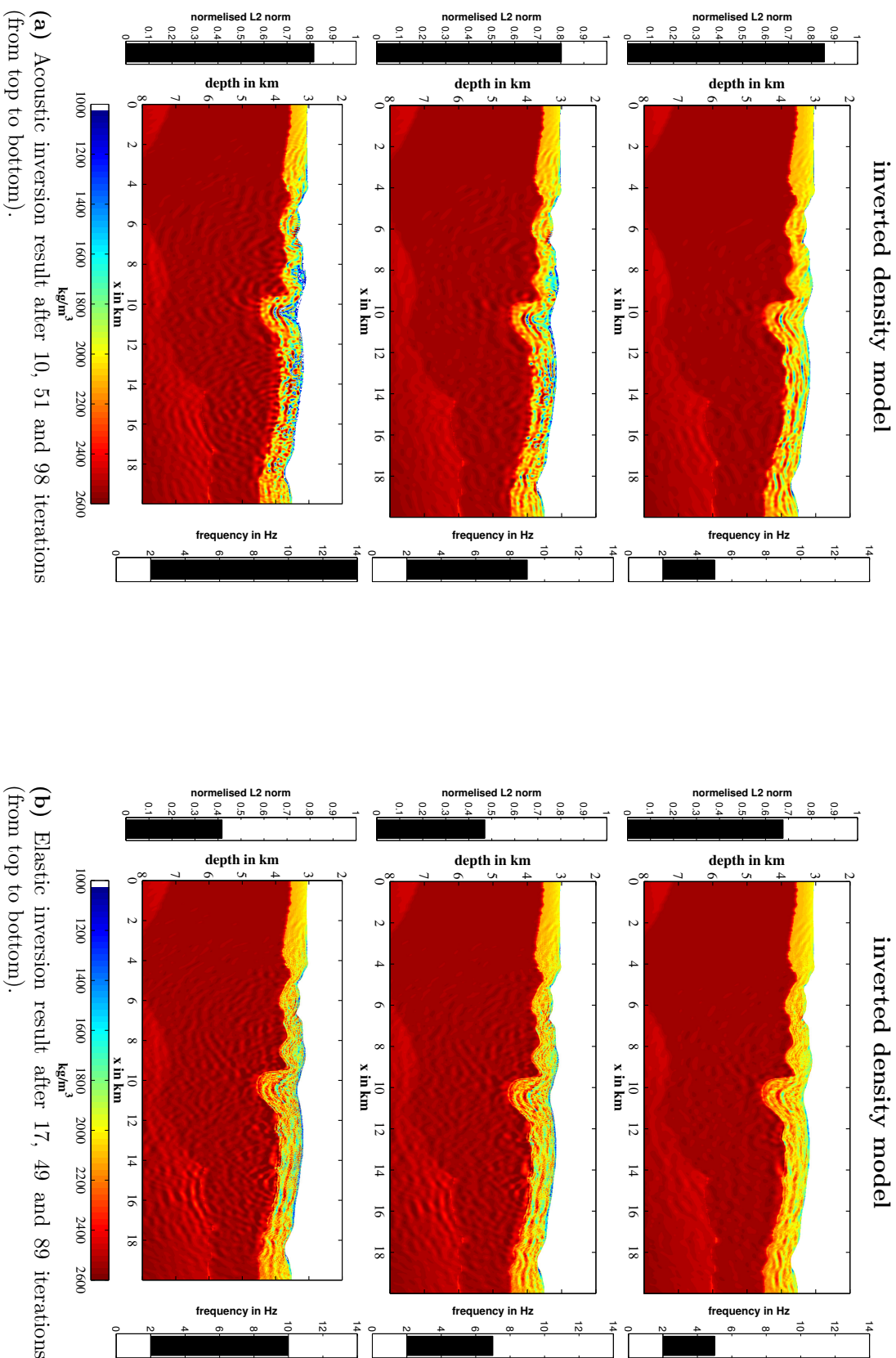
Figure 6.10: Development of elastic FWI using the 20 km-long PGS model as starting model. The shot gathers are trace-normalised. First row: result after 17 iterations; second row: result after 49 iterations; third row: result after 89 iterations. The L_2-norm misfit and the frequency stage are shown as bars on the left and right.

Figure 6.11: Development of acoustic and elastic FWI using the 20 km-long PGS model as starting model (density model). The L_2-norm misfit and the frequency stage are shown as bars on the left and right.

(a) Acoustic inversion result after 10, 51 and 98 iterations (from top to bottom).

(b) Elastic inversion result after 17, 49 and 89 iterations (from top to bottom).

Chapter 7

Evaluation & Interpretation

For field data FWI, the evaluation of the results is not trivial due to the ambiguity of the technique and the lack of knowledge about the true composition of the subsurface. Therefore, the results need to be examined carefully. Several parameters used for evaluating the inversion results were already plotted together with the inversion results themselves. For a further evaluation, I compare the inversion results with the reflectivity image provided by PGS. In addition, I take a closer look at the reliability and plausibility of the density results and give a possible geological interpretation of the inversion results.

7.1   Migration model

The results of the acoustic and elastic field data inversion shown in the last chapter are plotted again enlarged in figure 7.1 for the v_P inversion and in figure 7.2 for the density inversion. For comparison and quality control, a migrated section of the same part of the model is also plotted in both figures. The migrated section represents the reflectivity and was provided by PGS. The migration was performed using a Kirchhoff depth migration algorithm with the velocity model I utilised as starting model for the inversions (figure 3.5c). An overlay plot of the migration result and the FWI result is not shown in this work, as the locations of the horizons in both results may differ. The reason for this is that the migration result was calculated with the PGS model and not with the inverted model including the velocity changes in the sediments. A migration was not calculated on the basis of the new velocity model, since the migration requires a smooth velocity model and was beyond the scope of this project.

The migration result shows one distinct layer with high reflectivity above the salt, indicated by an arrow in figure 7.1b. This layer is not present in the starting model. In the acoustically inverted velocity model (v_P) shown in figure 7.1a, this layer starts to appear with a higher velocity. Especially above the valley in the TOS at about $x = 10$ km, a clear velocity contrast appears. The localised low- and high-velocity structures above the salt as well as the long-wavelength structures inside the salt are not visible in the migration result and, therefore, are categorised as artefacts.

The v_P inversion result of the elastic inversion (figure 7.1c) appears similar to the acoustic inversion result, only without the artefacts above the TOS. All structures in the sediments are layered and can also be seen in the migrated section. The high-reflectivity layer visible in the migration result suggests a high impedance contrast. In the velocity model, this layer is also visible, but only weakly.

The same layered structures can also be observed in the density result using acoustic FWI (figure 7.2a). However, as already indicated in the last chapter and similar to the velocity model, small-scale artefacts of about 200-300 m in size appear in the sediment layers and affect the clarity of the inverted high-density/velocity layer considerably. The density model in figure 7.2c representing the result of the elastic inversion clearly shows a higher resolution with almost no artefacts in the sediments. Only very small (less than 50 m in size) and low amplitude vertical artefacts are visible. The high-density/velocity layer as well as further details are clearly visible. Also, in the shadow zone visible in the migration result, structures are observable in the elastic FWI result of the density. A clearly continuous layer is shown in the results where the shadow zone is located.

For the acoustic case, I was able to perform a final inversion for the 88.5 km long model. The results of the v_P and density inversion are displayed in figure 7.3 together with the full migration result. As already shown for the inversion results of the smaller models, a high-velocity/density layer appears above the TOS. Also the tilted structures visible in the migration result can be imaged and, thus, parameter properties can be assigned to these structures. However, by comparing the migration result with the inversion results, several artefacts can be identified, already shown in the inversion result of the smaller model. Unfortunately, the computational resources available to me were not sufficient for calculating the elastic inversion of the 88.5 km-long model with IFOS2D. Therefore, within the scope of this work, only the acoustic inversion of the 88.5 km-long model is presented. The outcome of the elastic inversion of the smaller, 20 km-long model suggests, though, that a much more detailed velocity and density model with considerably less artefacts could also be obtained for the full profile.

7.2   Density

For the acoustic case, high-parameter layers were inserted by FWI in the sediments above the salt. The inverted density layers have unrealistically high values and are overlain by several artefacts. However, the location matches well with the migration results. The fact that density may be overestimated in the acoustic case is described in the literature (e.g., Métivier et al., 2015). The artefacts can be explained by elastic effects that cannot be described by the acoustic modelling.

For elastic FWI, the density model appears much more detailed, with fewer artefacts and lower, more realistic values than for the acoustic approximation of FWI. The fewer artefacts and lower amplitude can be explained by the more realistic elastic modelling, which is physi-
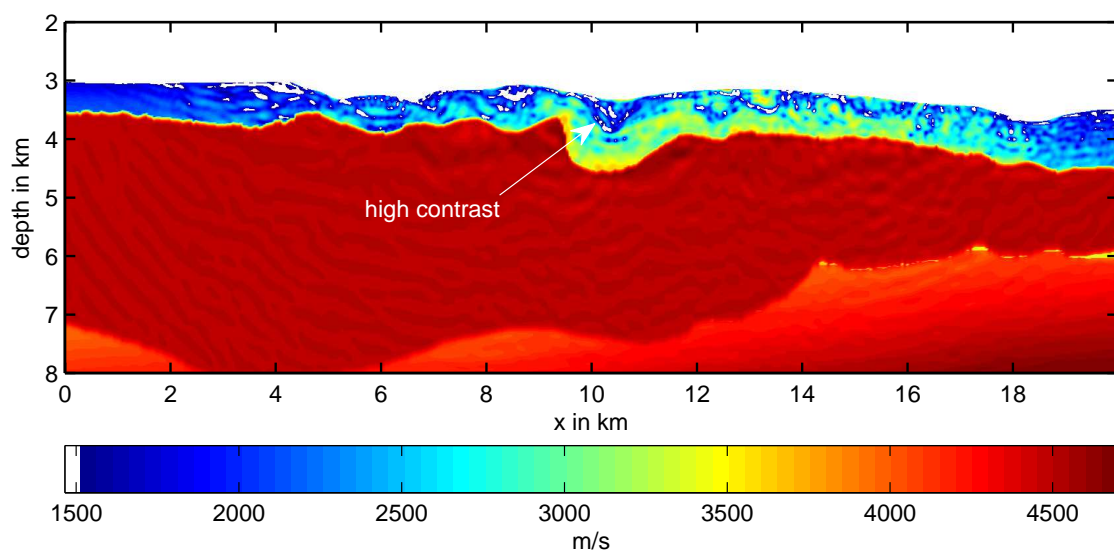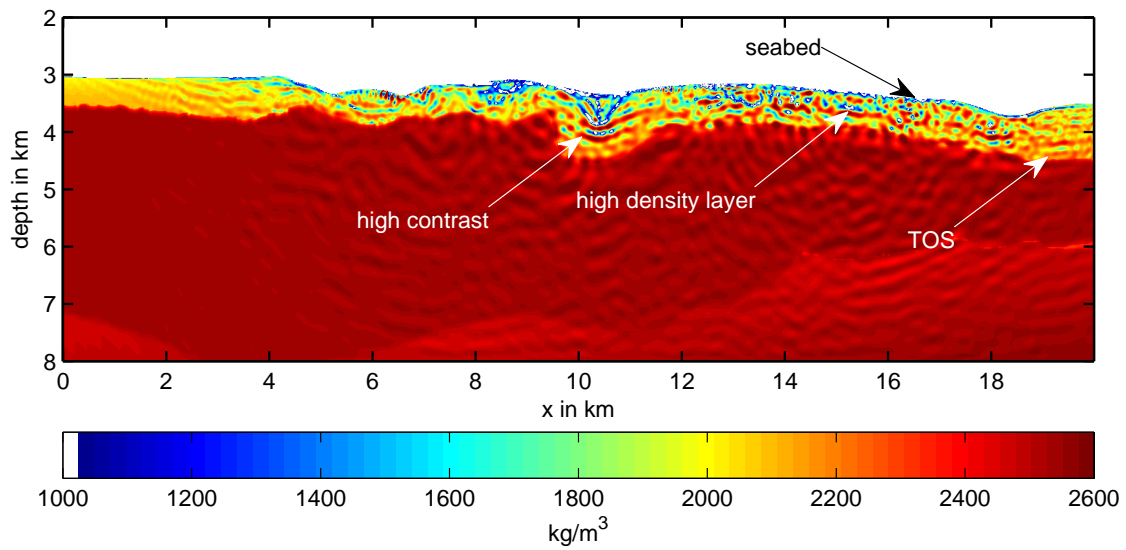
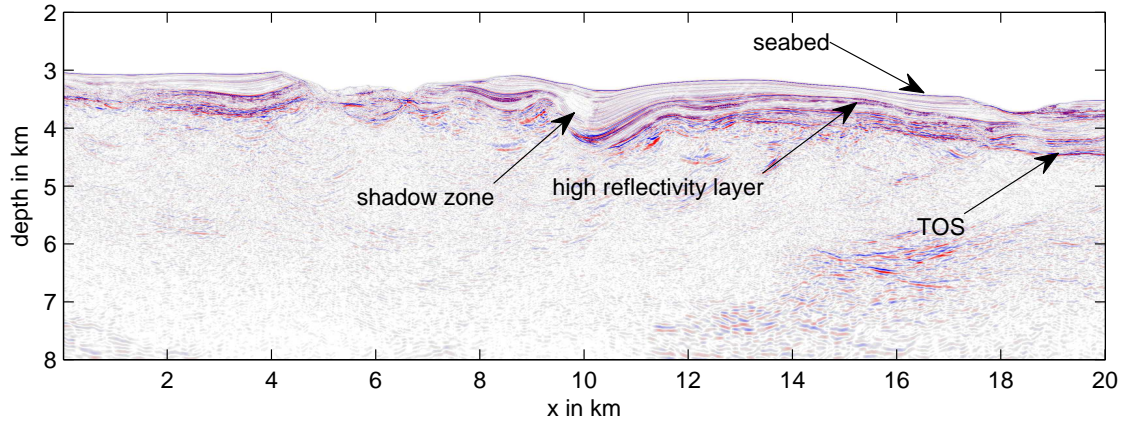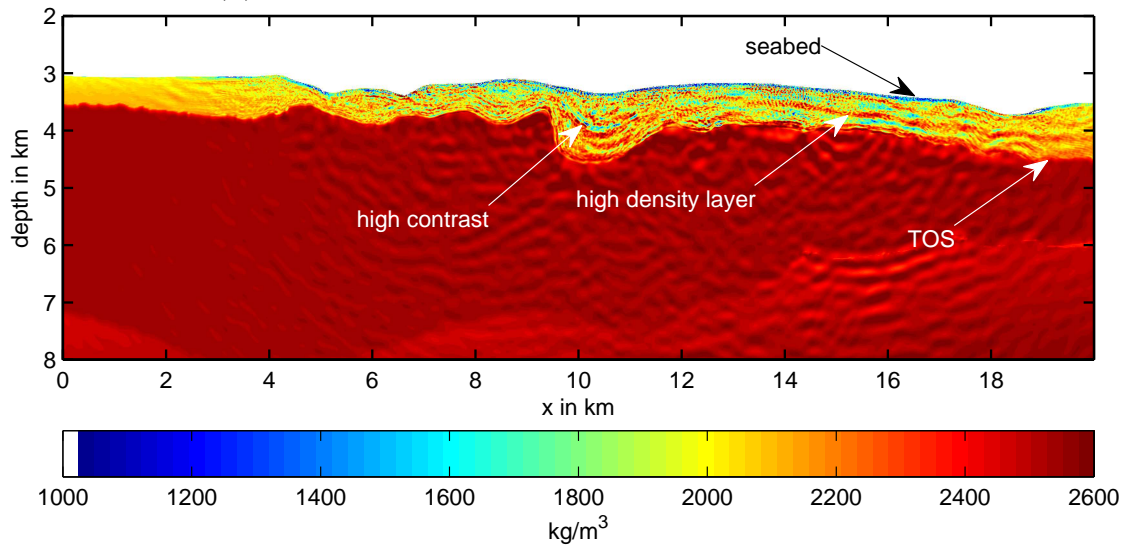(a) Acoustic inversion result after 98 iterations (14 Hz).
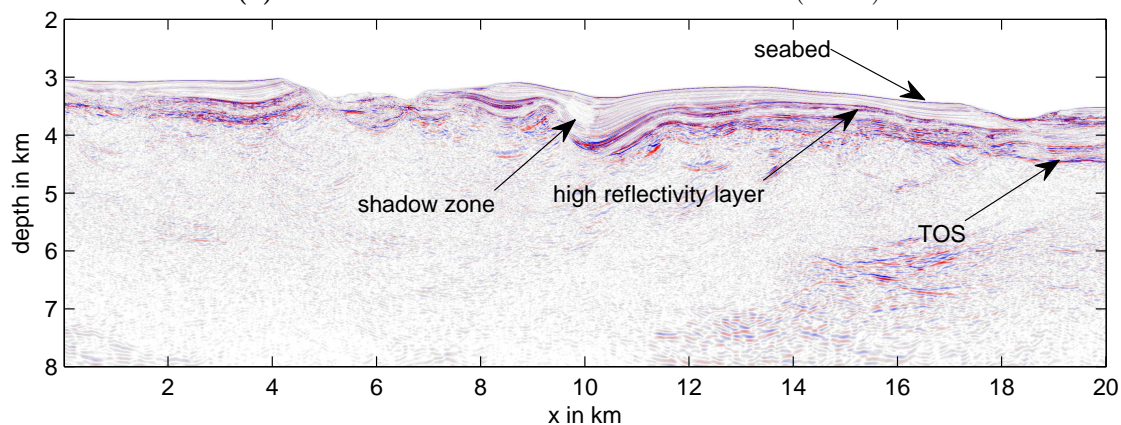
(b) Kirchhoff migration result using the v_P starting model.
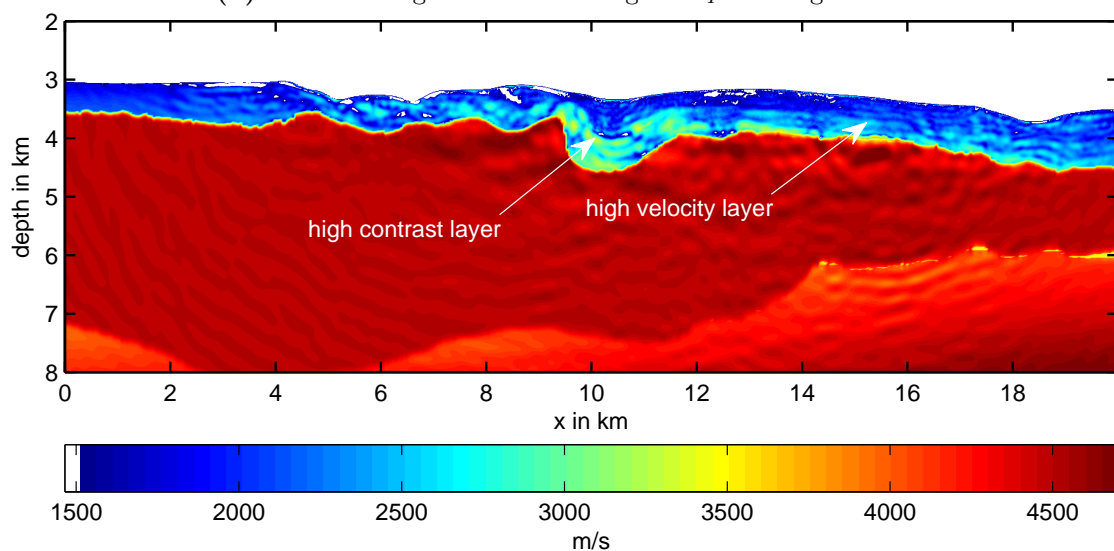
(c) Elastic inversion result after 89 iterations (10 Hz).

Figure 7.1: Comparison of the migration result (b) and the v_P inversion results (a and c) of the 20 km-long model.

(a) Acoustic inversion result after 98 iterations (14 Hz).

(b) Kirchhoff migration result using the v_P starting model.

(c) Elastic inversion result after 89 iterations (10 Hz).

Figure 7.2: Comparison of the migration result (b) and the density inversion results (a and c) of the 20 km-long model.
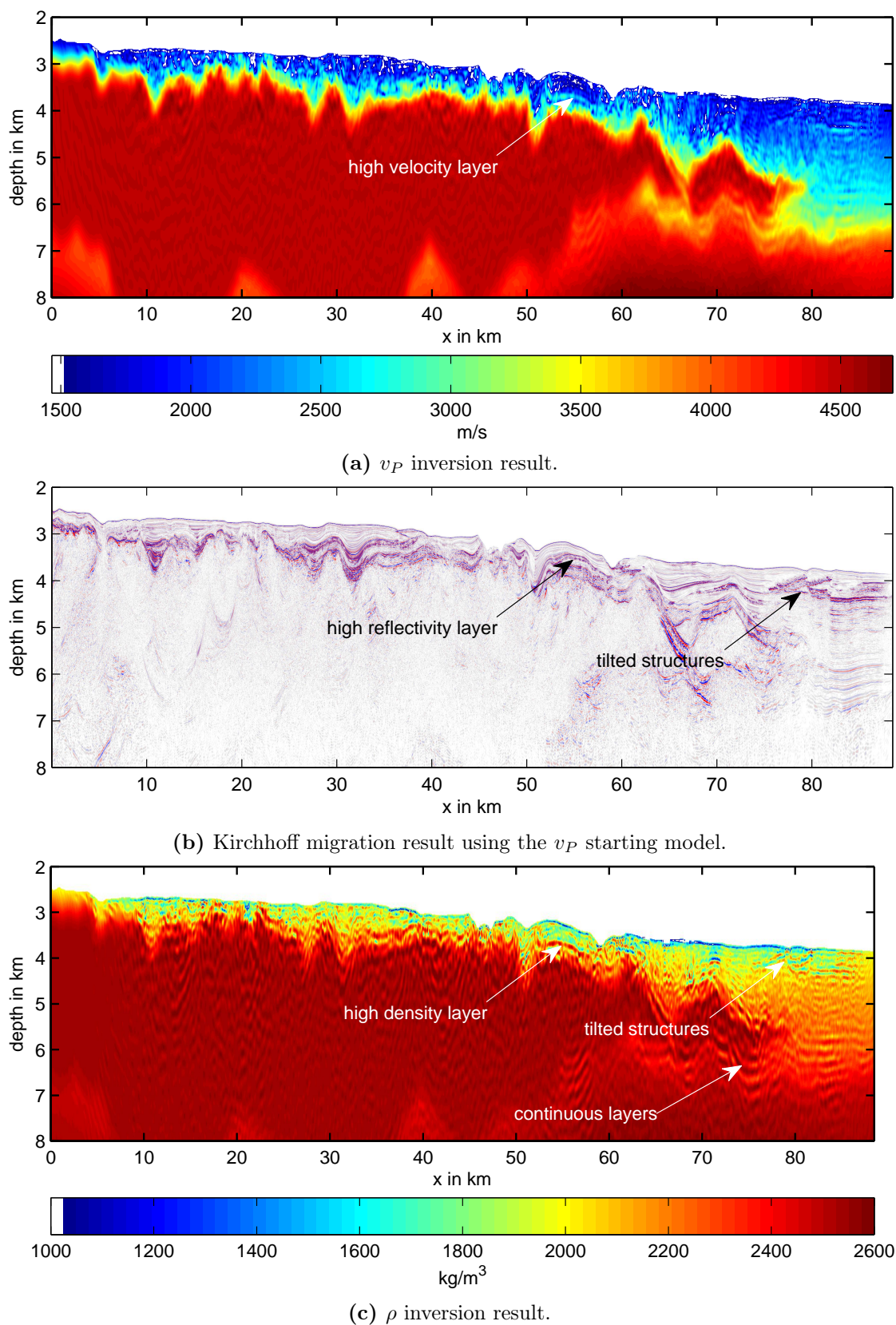
(a) v_P inversion result.

(b) Kirchhoff migration result using the v_P starting model.

(c) ρ inversion result.

Figure 7.3: Comparison of the migration result (b) and the acoustic inversion results (a and c) of the 88.5 km-long model after 33 iterations (8 Hz).

cally more correct. The more detailed inversion results of the density model compared to the velocity models can be explained by the special characteristics of the data set: As the data contains mainly reflected waves due to the deep water, FWI can use no other wave types, such as diving waves. The starting model contains already the most prominent features (sea floor, salt layer). Therefore, the greatest misfit in the low frequency data is generated by the amplitude differences, produced by density errors. Thus, FWI can reduce the misfit considerably by adapting the density model. This effect can produce better updates in the density model, which can also be seen in the synthetic case.

7.3   Geological interpretation

The stratigraphy in figure 3.4 suggests a thin layer of dolomite and limestone directly above the salt, followed by layers of shale and sandstone from the Late Cretaceous and Tertiary. By comparing the density and v_P model with the velocities for the described formations given in table 3.1, the occurring layers in the sediments above the salt can be interpreted. As dolomite and limestone have very similar v_P and density values, they cannot be differentiated by the parameter models obtained by elastic FWI. Both formations have similar v_P values and higher density values compared to salt. Synthetic tests including noise in the data showed that even an 80 m thick limestone layer directly above the salt can be resolved, if existing. As density values directly above the salt do not change towards higher values than in the salt, no dolomite or limestone are expected in this section of the Kwanza Basin.

Apart from the high-velocity/density layers in the sediments above the salt, the background sediments have a v_P value of about 2000 $\frac{m}{s}$ and a density value of about 1900 $\frac{kg}{m^3}$. These values match well with the properties for shale. The high-density layer has a value of about 2400 $\frac{kg}{m^3}$ and shows with about 2600 $\frac{m}{s}$ a higher velocity than the surrounding material. The higher values of the layer fit well to sandstone. Therefore, the inverted structure above the salt are interpreted as shale layers from the Cretaceous and Tertiary intercalated with higher density sandstone layers (Ivy Becker, personal communication, February 2018).

Chapter 8

Summary & Conclusions

The main objective of this thesis was the investigation of the advantages of elastic FWI in comparison to the acoustic approximation for marine streamer data in the presence of salt. For this purpose, a 2D marine streamer data set was used, provided by PGS. The data were acquired in deep water offshore Angola, West Africa, in the Kwanza Basin, which is known for salt layers and salt bodies. I was also provided with the results of a Kirchhoff depth migration: a reflectivity model and a simple P-wave velocity model including the seabed, a sediment gradient and the salt layer, but without further details.

In this work, I focused on the following aims:

- improvement of the velocity model using data from a single streamer acquisition by means of elastic FWI instead of acoustic FWI,

- relevance of the density model for elastic FWI in order to allow a direct geological interpretation of the FWI results,

- application of a modified flooding method in a pure FWI workflow on field data for the generation of a starting model.

For the acoustic and elastic inversion, the 2D time-domain FD code IFOS2D was applied which uses a conjugate gradient method. The theory behind the code is shown in chapter 2. Before starting with the inversion, it was necessary to implement a receiver ghost removal in the inversion code, as the data were acquired using a 10 km-long dual-sensor streamer and the receiver ghost was already eliminated by using wavefield separation (see section 2.4.2). Furthermore, a 3D-2D transformation was performed in order to correct 3D effects in phase and amplitude.

The model and data, as well as the geology of the acquisition area were described in chapter 3. The acquisition profile extended over 265 km with a maximum water depth of more than 3 km. Due to computational reasons, the model was limited to a subpart of 20 km length and 12 km depth. Only the acoustic FWI was performed using the 88.5 km-long model. Also, the data were limited to 12 s. In the model, a continuous salt layer is located in a sediment environment,

producing high parameter contrasts in the density and velocity models at the interfaces. In addition, the top of salt (TOS) shows strong topography. These properties of the subsurface are responsible for a very complex wavefield, making it challenging for conventional ray-based methods to produce high-resolution models. This can also be seen in the reflectivity model. The reflectivity model shows several layers in the sediments above the TOS, partially with high reflectivity, but also shows areas in the sediments where the method was not able to image any structures.

Subsequently, before starting with the field data FWI, several synthetic tests and field data tests were performed. These tests were necessary to adjust and calibrate the parameters of the FWI workflow for the given acquisition geometry and model. Also the provided velocity model was examined and proved to be sufficient as starting model for FWI.

Acoustic vs. elastic FWI

For complex media where ray-based methods proved to be insufficient, acoustic FWI has become more and more established over the last years. Elastic FWI results were only presented for ocean bottom/node data sets (e.g., Sears et al., 2010). This work examined the advantages of elastic FWI applied on a standard 2D single-streamer data set.

To be able to evaluate the elastic FWI results, also the acoustic approximation was applied for all inversions. By using the provided velocity model as starting model, the acoustic inversion produced the parameter models shown in section 6.2.1. The inversion results of the v_P model show an increase of about 500 $\frac{\text{m}}{\text{s}}$ in most parts of the sediments but in contrast to the reflectivity model no layered structures are visible. In the density model, a high-density layer appeared but the entire model is overlain with several artefacts of various scale. Therefore, it is difficult to identify any plausible structures. The reason for the artefacts could be tracked down as elastic effects.

The elastic FWI was able to reduce the misfit to 41 % of the initial misfit, compared to 82 % after the acoustic FWI. The good quality of the inversion is also confirmed by other quality parameters, such as the inverted source time functions and a comparison of the modelled and field data shot gathers. The good convergence can also be observed in the inverted parameter models: the v_P model reveals clear layered structures of about 300 $\frac{\text{m}}{\text{s}}$ increased velocity compared to the background values in the sediments. The inverted high-value structures in the density model are even better visible than in the velocity model, showing increases of about 400 $\frac{\text{kg}}{\text{m}^3}$. All inverted structures of both parameter models can be confirmed by high-contrast structures in the reflectivity model. Even in the area which could not be imaged by the migration, a continuous high-density/velocity layer is visible in the FWI result.

In summary, the acoustic inversion produces results characterised mainly by artefacts. The elastic inversion proved to be essential in order to produce FWI results showing reasonable structures in the sediments. All inverted structures could be confirmed by the provided reflectivity model.

Density and direct geological interpretation

Usually, the density model is only used as passive parameter and often kept constant during FWI, or used as a collector for artefacts caused by insufficient physical modelling or other deficiencies, for example 3D effects. However, in the presented elastic inversion the structures could be imaged even more precisely in the density model than in the v_P model. This can be explained for this deep water data set, as only reflected waves are available for inversion. In addition, the geological formations above the salt have high density contrasts.

The great advantage of an invertable density model is the potential of a direct geological interpretation. The parameter models of the elastic FWI up to 10 Hz have a sufficient resolution to interpret layers of about 100 m thickness. By comparing the obtained velocity and density values of the layers with literature (section 3.1), the sediments above the salt could be interpreted as shale, intersected by layers of sandstone, represented by the high-velocity/density layer. These structures are consistent with stratigraphic models of the region.

Starting model generation

A sufficiently accurate starting model is the most important prerequisite for a successful FWI. Typically, the starting model is generated by using traveltime tomography, which has a very low computational cost compared to FWI. In exploration geophysics, the velocity model is further enhanced by migration velocity analysis for a successful depth migration. The obtained velocity model can be used as starting model for FWI to make further improvements. When salt bodies are known in the acquisition area, the top of salt (TOS) and bottom of salt (BOS) are reconstructed by the flooding method during the migration velocity analysis. As the migration velocity analysis consumes much more time and computational effort than the simple method mentioned previously, I used a modified flooding method directly inside an FWI workflow. Thus, I do not have to use a second method such as migration and can generate a starting model with very low computational cost and time effort compared to a full depth migration. The method was initially developed by Boonyasiriwat et al. (2010) and modified and tested in a synthetic environment by Thiel (2013). The modifications allow the picking of distinct interfaces with high impedance contrast (e.g., sediment-salt interface) after only 1-10 iterations, depending on the depth of the interface. In addition, the flooding with a gradient in the sediment area supports a better convergence of FWI. The modified flooding method was applied on the field data.

The testing of the method for the given acquisition geometry and starting model in a synthetic test showed a successful reconstruction of the salt body with location errors of up to 200 m for the TOS and 400 m for the BOS. The errors are equal to less than half a wavelength for a maximum frequency of 5 Hz. The synthetic test also highlighted the difficulties in tracking the bottom of salt due to low impedance contrasts and the large influence of shallow structures on deeper targets.

In the field data application, the complex sediments above the salt proved to complicate the picking of the salt boundaries. Especially the BOS layer was not possible to pick without the knowledge of the approximated location from the PGS model. However, I was able to generate a starting model including the salt layer by using the modified flooding method in FWI with only little prior knowledge about the salt body. A comparison of the salt location in the provided model to the picked salt contour in the field data inversion and synthetic inversion results revealed about the same location differences.

The utilisation of the generated starting model revealed a similar misfit value for the acoustic inversion result compared to the usage of the provided starting model. However, even fewer structures in the sediments are visible in the inversion result using the flooded model. For the elastic inversion, the data misfit was reduced to 50 % of the initial misfit, compared to a reduction to 41 % for the inversion result using the provided starting model. Layered structures appear in the density and v_P model but are weaker and cannot be connected to structures in the reflectivity model. Therefore, I concluded that the flooded starting model was insufficient for a successful FWI.

Overall, I can say that the application of the flooding technique was only restrictedly successful for this deep water data set. The generated model showed differences of up to 400 m in the location of the salt compared to the provided PGS model. These errors proved to produce several artefacts in the inversion results, also for the elastic inversion. Therefore, I recommend to use a different method to generate the starting model for this data set. The flooding method may be better applicable for shallower data sets.

Concluding, I show in this work that even for marine streamer data an elastic FWI approach was necessary to invert structures in the sediments and the acoustic approximation was not sufficient. Even the often neglected density parameter in FWI can provide well defined structures in the resulting model using elastic FWI, also for parts of the model where the migration method failed. With a well resolved velocity and density model derived from elastic FWI, a direct geological interpretation was possible. Thus, elastic FWI can help to produce much better images of the subsurface for complex media compared to acoustic FWI, supporting a more precise interpretation for the exploration of reservoirs. For this work, only a standard 2D single streamer data set was available. Therefore, this method has also a great potential to enhance older 2D legacy data sets that were only processed by standard ray-based methods to derive more information of the subsurface and possible reservoirs. A further improvement of the results may be obtained by including anisotropy and/or attenuation in the modelling and inversion. Especially the sediments are often affected by anisotropy. However, even assuming an isotropic elastic medium without attenuation, the inversion was able to image all main structures in the density and v_P model.

Bibliography

Alford, R., Kelly, K., and Boore, D. M. (1974). Accuracy of finite-difference modeling of the acoustic wave equation. *Geophysics*, 39(6):834–842.

Amundsen, L. (1993). Wavenumber-based filtering of marine point-source data. *Geophysics*, 58(9):1335–1348.

Auer, L., Nuber, A. M., Greenhalgh, S. A., Maurer, H., and Marelli, S. (2013). A critical appraisal of asymptotic 3d-to-2d data transformation in full-waveform seismic crosshole tomography. *Geophysics*, 78(6):R235–R247.

Bai, J. and Yingst, D. (2014). Simultaneous inversion of velocity and density in time-domain full waveform inversion. In *SEG Technical Program Expanded Abstracts 2014*. Society of Exploration Geophysicists.

Bohlen, T. (1998). *Viskoelastische FD-modellierung seismischer Wellen zur Interpretation gemessener Seismogramme*. PhD thesis, Christian-Albrechts-Universitat zu Kiel.

Bohlen, T. (2002). Parallel 3-D viscoelastic finite difference seismic modelling. *Computers & Geosciences*, 28(8):887–899.

Boonyasiriwat, C., Schuster, G. T., Macy, B., Valasek, P., and Cao, W. (2010). Application of multiscale waveform inversion to marine data using a flooding technique and dynamic early-arrival windows. *Geophysics*, 75(6):R129–R136.

Bourbié, T., Coussy, O., and Zinszner, B. (1987). *Acoustics of porous media*. Institut Français du Pétrole publications. Éd. Technip, Paris.

Brenders, A. and Pratt, R. G. (2007). Waveform tomography of marine seismic data: What can limited offset offer? In *SEG Technical Program Expanded Abstracts 2007*, pages 3024–3028. Society of Exploration Geophysicists.

Brognon, G. P. and Verrier, G. R. (1966). Oil and geology in Cuanza Basin of Angola. *AAPG Bulletin*, 50(1):108–158.

Brossier, R., Operto, S., and Virieux, J. (2009). Seismic imaging of complex onshore structures by 2D elastic frequency-domain full-waveform inversion. *Geophysics*, 74(6):WCC105–WCC118.

Brownfield, M. E. and Charpentier, R. R. (2006). Geology and total petroleum systems of the West-Central Coastal province (7203), West Africa. Technical report.

Bunks, C., Saleck, F. M., Zaleski, S., and Chavent, G. (1995). Multiscale seismic waveform inversion. *Geophysics*, 60(5):1457–1473.

Butzer, S., Kurzmann, A., and Bohlen, T. (2013). 3D elastic full-waveform inversion of small-scale heterogeneities in transmission geometry. *Geophysical Prospecting*, 61(6):1238–1251.

Carlson, D., Long, A., Söllner, W., Tabti, H., Tenghamn, R., and Lunde, N. (2007). Increased resolution and penetration from a towed dual-sensor streamer. *First Break*, 25(12).

Cerjan, C., Kosloff, D., Kosloff, R., and Reshef, M. (1985). A nonreflecting boundary condition for discrete acoustic and elastic wave equations. *Geophysics*, 50(4):705–708.

Chazalnoel, N., Gomes, A., Zhao, W., and Wray, B. (2017). Revealing shallow and deep complex geological features with FWI: Lessons learned.

Choi, Y. and Alkhalifah, T. (2012). Application of multi-source waveform inversion to marine streamer data using the global correlation norm. *Geophysical Prospecting*, 60:748–758.

Choi, Y., Min, D.-J., and Shin, C. (2008). Frequency-domain elastic full waveform inversion using the new pseudo-Hessian matrix: Experience of elastic Marmousi-2 synthetic data. *Bulletin of the Seismological Society of America*, 98(5):2402–2415.

Collino, F. and Tsogka, C. (2001). Application of the perfectly matched absorbing layer model to the linear elastodynamic problem in anisotropic heterogeneous media. *Geophysics*, 66(1):294–307.

Corcoran, C., Perkins, C., Lee, D., Cattermole, P., Cook, R., and Moldoveanu, N. (2007). A wide-azimuth streamer acquisition pilot project in the Gulf of Mexico. *The Leading Edge*, 26(4):460–468.

Courant, R., Friedrichs, K., and Lewy, H. (1928). Über die partiellen Differenzengleichungen der mathematischen Physik. *Mathematische Annalen*, 100(1):32–74.

Courant, R., Friedrichs, K., and Lewy, H. (1967). On the partial difference equations of mathematical physics. *IBM journal*, 11(2):215–234.

Crase, E., Pica, A., Noble, M., McDonald, J., and Tarantola, A. (1990). Robust elastic nonlinear waveform inversion: Application to real data. *Geophysics*, 55(5):527–538.

Dougherty, M. E. and Stephen, R. A. (1988). Seismic energy partitioning and scattering in laterally heterogeneous ocean crust. In *Scattering and Attenuations of Seismic Waves, Part I*, pages 195–229. Springer.

Duval, B., Cramez, C., and Jackson, M. (1992). Raft tectonics in the Kwanza basin, Angola. *Marine and Petroleum Geology*, 9(4):389–404.

Esser, E., Guasch, L., Leeuwen, T. v., Aravkin, A. Y., and Herrmann, F. J. (2015). Automatic salt delineation - wavefield reconstruction inversion with convex constraints. In *SEG Technical Program Expanded Abstracts 2015*, pages 1337–1343. Society of Exploration Geophysicists.

Etgen, J., Gray, S. H., and Zhang, Y. (2009). An overview of depth imaging in exploration geophysics. *Geophysics*, 74(6):WCA5–WCA17.

Faust, L. Y. (1951). Seismic velocity as a function of depth and geologic time. *Geophysics*, 16(2):192–206.

Fichtner, A. (2011). *Full seismic waveform modelling and inversion*. Springer Science & Business Media.

Forbriger, T., Groos, L., and Schäfer, M. (2014). Line-source simulation for shallow-seismic data. part 1: Theoretical background. *Geophysical Journal International*, 198(3):1387–1404.

Gardner, G. H. F., Gardner, L. W., and Gregory, A. R. (1974). Formation Basics for Velocity and Density - The Traps Diagnostic Stratigraphic. *Geophysics*, 39(6):770–780.

Gauthier, O., Virieux, J., and Tarantola, A. (1986). Two-dimensional nonlinear inversion of seismic waveforms: Numerical results. *Geophysics*, 51(7):1387–1403.

Groos, L. (2013). *2D full waveform inversion of shallow seismic Rayleigh waves*. PhD thesis, Karlsruhe Institute of Technology (KIT).

Jeong, W., Lee, H.-Y., and Min, D.-J. (2012). Full waveform inversion strategy for density in the frequency domain. *Geophysical Journal International*, 188(3):1221–1242.

Jiang, Z., Wang, R., and Zheng, W. (2014). Genetic stratigraphy of a part of the Miocene Congo Fan, West Africa. *Journal of African Earth Sciences*, 95:138 – 144.

Klüver, T. (2008). Wavefield separation for dual-sensor data with local handling of aliased energy. In *SEG Technical Program Expanded Abstracts 2008*. Society of Exploration Geophysicists.

Köhn, D. (2011). *Time Domain 2D Elastic Full Waveform Tomography*. PhD thesis, Christian-Albrechts-Universität zu Kiel.

Köhn, D., De Nil, D., Kurzmann, A., Przebindowska, A., and Bohlen, T. (2012). On the influence of model parametrization in elastic full waveform tomography. *Geophysical Journal International*, 191(1):325–345.

Komatitsch, D. and Martin, R. (2007). An unsplit convolutional perfectly matched layer improved at grazing incidence for the seismic wave equation. *Geophysics*, 72(5):SM155–SM167.

Kurzmann, A. (2012). *Applications of 2D and 3D full waveform tomography in acoustic and viscoacoustic complex media.* PhD thesis, Karlsruhe Institute of Technology (KIT).

Lay, T. and Wallace, T. C. (1995). *Modern global seismology*, volume 58. Academic Press.

Leroy, C. C., Robinson, S. P., and Goldsmith, M. J. (2008). A new equation for the accurate calculation of sound speed in all oceans. *The Journal of the Acoustical Society of America*, 124(5):2774–2782.

Levander, A. R. (1988). Fourth-order finite-difference P-SV seismograms. *Geophysics*, 53(11):1425–1436.

Leveille, J. P., Jones, I. F., Zhou, Z.-Z., Wang, B., and Liu, F. (2011). Subsalt imaging for exploration, production, and development: A review. *Geophysics*, 76(5):WB3–WB20.

Lévĕque, J.-J., Rivera, L., and Wittlinger, G. (1993). On the use of the checker-board test to assess the resolution of tomographic inversions. *Geophysical Journal International*, 115(1):313–318.

Lewis, W., Starr, B., and Vigh, D. (2012). A level set approach to salt geometry inversion in full-waveform inversion. In *SEG Technical Program Expanded Abstracts 2012*, pages 1–5. Society of Exploration Geophysicists.

Liang, W.-g., Yang, C.-h., Zhao, Y.-s., Dusseault, M., and Liu, J. (2007). Experimental investigation of mechanical properties of bedded salt rock. *International Journal of Rock Mechanics and Mining Sciences*, 44(3):400–411.

Lu, R., Lazaratos, S., Wang, K., Cha, Y., Chikichev, I., and Prosser, R. (2013). High-resolution elastic FWI for reservoir characterization. In *75th EAGE Conference & Exhibition incorporating SPE EUROPEC 2013*.

Lundin, E. R. (1992). Thin-skinned extensional tectonics on a salt detachment, northern Kwanza Basin, Angola. *Marine and Petroleum Geology*, 9(4):405–411.

Martin, R. and Komatitsch, D. (2009). An unsplit convolutional perfectly matched layer technique improved at grazing incidence for the viscoelastic wave equation. *Geophysical Journal International*, 179(1):333–344.

Métivier, L., Brossier, R., Operto, S., and Virieux, J. (2015). Acoustic multi-parameter FWI for the reconstruction of P-wave velocity, density and attenuation: preconditioned truncated Newton approach. In *SEG Technical Program Expanded Abstracts 2015*. Society of Exploration Geophysicists.

Mora, P. (1987). Nonlinear two-dimensional elastic inversion of multioffset seismic data. *Geophysics*, 52(9):1211–1228.

Morgan, J., Warner, M., Bell, R., Ashley, J., Barnes, D., Little, R., Roele, K., and Jones, C. (2013). Next-generation seismic experiments: wide-angle, multi-azimuth, three-

dimensional, full-waveform inversion. *Geophysical Journal International*, 195(3):1657–1678.

Morse, P. M. and Feshbach, H. (1953). Methods of theoretical physics. *New York: McGraw-Hill*.

Mulder, W. and Plessix, R.-E. (2008). Exploring some issues in acoustic full waveform inversion. *Geophysical Prospecting*, 56(6):827–841.

Nocedal, J. and Wright, S. (1999). Numerical optimization. *Springer Science*, 35:67–68.

Peng, C., Wang, M., Chazalnoel, N., and Gomes, A. (2018). Subsalt imaging improvement possibilities through a combination of FWI and reflection FWI. *The Leading Edge*, 37(1):52–57.

Petroleum Geo-Services (2018). Flyer "ANG Offshore 2D GeoStreamer". https://www.pgs.com/contentassets/15a689f30b7848eb9e1cfdff772bd43c/flyer-ang-offshore-2d-geostreamer-a4.pdf (accessed January 25, 2018).

Pica, A., Diet, J., and Tarantola, A. (1990). Nonlinear inversion of seismic reflection data in a laterally invariant medium. *Geophysics*, 55(3):284–292.

Plessix, R., Milcik, P., Rynja, H., Stopin, A., Matson, K., and Abri, S. (2013). Multiparameter full-waveform inversion: Marine and land examples. *The Leading Edge*, 32(9):1030–1038.

Plessix, R.-E. (2006). A review of the adjoint-state method for computing the gradient of a functional with geophysical applications. *Geophysical Journal International*, 167(2):495–503.

Plessix, R.-E. and Mulder, W. (2004). Frequency-domain finite-difference amplitude-preserving migration. *Geophysical Journal International*, 157(3):975–987.

Pratt, R. G. (1999). Seismic waveform inversion in the frequency domain, part 1: Theory and verification in a physical scale model. *Geophysics*, 64(3):888–901.

Pratt, R. G., Shin, C., and Hick, G. (1998). Gauss–Newton and full Newton methods in frequency–space seismic waveform inversion. *Geophysical Journal International*, 133(2):341–362.

Przebindowska, A. (2013). *Acoustic full waveform inversion of marine reflection seismic data.* PhD thesis, Karlsruhe Institute of Technology (KIT).

Przebindowska, A., Kurzmann, A., Köhn, D., and Bohlen, T. (2012). The role of density in acoustic full waveform inversion of marine reflection seismics. In *74th EAGE Conference and Exhibition incorporating EUROPEC 2012*.

Qin, B. and Lambare, G. (2016). Joint inversion of velocity and density in preserved-amplitude full-waveform inversion. In *SEG Technical Program Expanded Abstracts 2016*. Society of Exploration Geophysicists.

Raknes, E. B. and Arntsen, B. (2014). Strategies for elastic full waveform inversion. In *SEG Technical Program Expanded Abstracts 2014*. Society of Exploration Geophysicists.

Ravaut, C., Alerini, M., Pannetier-Lescoffit, S., and Thomassen, E. (2008). Sub-salt imaging by full-waveform inversion: a parameter analysis. In *SEG Technical Program Expanded Abstracts 2008*. Society of Exploration Geophysicists.

Rekdal, T. and Long, A. (2006). Recent advances in marine seismic acquisition and processing technology. *Recorder*, 31.

Reynolds, J. M. (1997). *An introduction to applied and environmental geophysics*. John Wiley & Sons.

Robertsson, J. O., Levander, A., Symes, W. W., and Holliger, K. (1995). A comparative study of free-surface boundary conditions for finite-difference simulation of elastic/viscoelastic wave propagation. In *SEG Technical Program Expanded Abstracts 1995*, pages 1277–1280. Society of Exploration Geophysicists.

Sears, T. J., Barton, P. J., and Singh, S. C. (2010). Elastic full waveform inversion of multi-component ocean-bottom cable seismic data: Application to Alba Field, UK North Sea. *Geophysics*, 75(6):R109–R119.

Shannon, C. E. (1949). Communication in the presence of noise. *Proceedings of the IRE*, 37(1):10–21.

Shen, X., Ahmed, I., Brenders, A., Dellinger, J., Etgen, J., and Michell, S. (2018). Full-waveform inversion: The next leap forward in subsalt imaging. *The Leading Edge*, 37(1):67b1–67b6.

Shipp, R. M. and Singh, S. C. (2002). Two-dimensional full wavefield inversion of wide-aperture marine seismic streamer data. *Geophysical Journal International*, 151(2):325–344.

Sirgue, L. (2006). The importance of low frequency and large offset in waveform inversion. In *68th EAGE Conference and Exhibition incorporating SPE EUROPEC 2006*.

Sirgue, L., Barkved, O., Dellinger, J., Etgen, J., Albertin, U., and Kommedal, J. (2010). Thematic set: Full waveform inversion: The next leap forward in imaging at Valhall. *First Break*, 28(4):65–70.

Sirgue, L. and Pratt, R. G. (2004). Efficient waveform inversion and imaging: A strategy for selecting temporal frequencies. *Geophysics*, 69(1):231–248.

Spathopoulos, F. (1996). An insight on salt tectonics in the Angola Basin, South Atlantic. *Geological Society, London, Special Publications*, 100(1):153–174.

Sun, D., Jiao, K., Cheng, X., and Vigh, D. (2016). Reflection based waveform inversion. In *SEG Technical Program Expanded Abstracts 2016*, pages 1151–1156. Society of Exploration Geophysicists.

Tarantola, A. (1984). Inversion of seismic reflection data in the acoustic approximation. *Geophysics*, 49(8):1259–1266.

Tarantola, A. (2005). *Inverse problem theory and methods for model parameter estimation*, volume 89. SIAM.

Thiel, N. (2013). Imaging of subsalt structures with acoustic and elastic full waveform inversion (FWI). Master's thesis, Karlsruhe Institute of Technology (KIT).

Tromp, J., Tape, C., and Liu, Q. (2005). Seismic tomography, adjoint methods, time reversal and banana-doughnut kernels. *Geophysical Journal International*, 160(1):195–216.

Valle, P. J., Gjelberg, J. G., and Helland-Hansen, W. (2001). Tectonostratigraphic development in the eastern Lower Congo Basin, offshore Angola, west Africa. *Marine and Petroleum Geology*, 18(8):909–927.

Vigh, D., Jiao, K., Watts, D., and Sun, D. (2014). Elastic full-waveform inversion application using multicomponent measurements of seismic data collection. *Geophysics*, 79(2):R63–R77.

Vigh, D., Kapoor, J., Moldoveanu, N., and Li, H. (2011). Breakthrough acquisition and technologies for subsalt imaging. *Geophysics*, 76(5):WB41–WB51.

Vigh, D., Starr, B., Kapoor, J., and Li, H. (2010). 3D full waveform inversion on a Gulf of Mexico WAZ data set. In *SEG Technical Program Expanded Abstracts 2010*, pages 957–961. Society of Exploration Geophysicists.

Virieux, J. (1986). P-SV wave propagation in heterogeneous media: Velocity-stress finite-difference method. *Geophysics*, 51(4):889–901.

Virieux, J. and Operto, S. (2009). An overview of full-waveform inversion in exploration geophysics. *Geophysics*, 74(6):WCC1–WCC26.

Wang, K., Deng, B., Zhang, Z., Hu, L., and Huang, Y. (2015). Top of salt impact on full waveform inversion sediment velocity update. In *SEG Technical Program Expanded Abstracts 2015*, pages 1064–1069. Society of Exploration Geophysicists.

Warner, M., Morgan, J., Umpleby, A., Stekl, I., and Guasch, L. (2012). Which physics for full-wavefield seismic inversion? In *74th EAGE Conference and Exhibition incorporating EUROPEC 2012*.

Warner, M., Ratcliffe, A., Nangoo, T., Morgan, J., Umpleby, A., Shah, N., Vinje, V., Štekl, I., Guasch, L., Win, C., Conroy, G., and Bertrand, A. (2013). Anisotropic 3D full-waveform inversion. *Geophysics*, 78(2):R59–R80.

Williamson, P., Rivera, C., and Mansoor, K. (2016). Acoustic FWI applied to subsalt imaging: an illuminating case study from offshore Angola. In *SEG Technical Program Expanded Abstracts 2016*, pages 4896–4900. Society of Exploration Geophysicists.

Xiao, B., Kotova, N., Bretherton, S., Ratcliffe, A., Duval, G., Page, C., and Pape, O. (2016). An offshore Gabon full-waveform inversion case study.

Zdraveva, O., Woodward, M., Hydal, S., and Derbala, R. (2012). Improved pre-salt imaging in Kwanza basin by TTI Model building with geological constraints. In *SEG Technical Program Expanded Abstracts 2012*, pages 1–5. Society of Exploration Geophysicists.

Zhou, W., Brossier, R., Operto, S., and Virieux, J. (2015). Full waveform inversion of diving & reflected waves for velocity model building with impedance inversion based on scale separation. *Geophysical Journal International*, 202(3):1535–1554.

List of Figures

List of Tables

Appendix A

Full shot gathers

A.1   Field data tests

(a) Field data.

(b) Benchmark test (acoustic, PGS model).

(c) No 3d-2d conversion was applied to the data.

(d) Only the first half offset was used.

(e) Time window of 2 s after first reflection or refraction applied to the data.

Figure A.1: Full seismograms of field data tests. All plots show seismograms of shot 7. For more detail see chapter 5.

A.2 Inversion results

(a) Modelled data after acoustic FWI at 14 Hz using the PGS model as starting model.

(b) Modelled data after elastic FWI at 10 Hz using the PGS model as starting model.

(c) Field data at 14 Hz.

(d) Field data at 10 Hz.

(e) Modelled data after acoustic FWI (upper corner frequency of the filter at 14 Hz) using flooded model as starting model.

(f) Modelled data after elastic FWI (upper corner frequency of the filter at 10 Hz) using flooded model as starting model.

Figure A.2: Full seismograms of the field data inversions shown in sections 6.1 and 6.2. All plots show seismograms of shot 7 (model 3). For the inversion, a time window starting at the first reflection/refraction and ending at starting point plus 6 s was used.

Appendix B

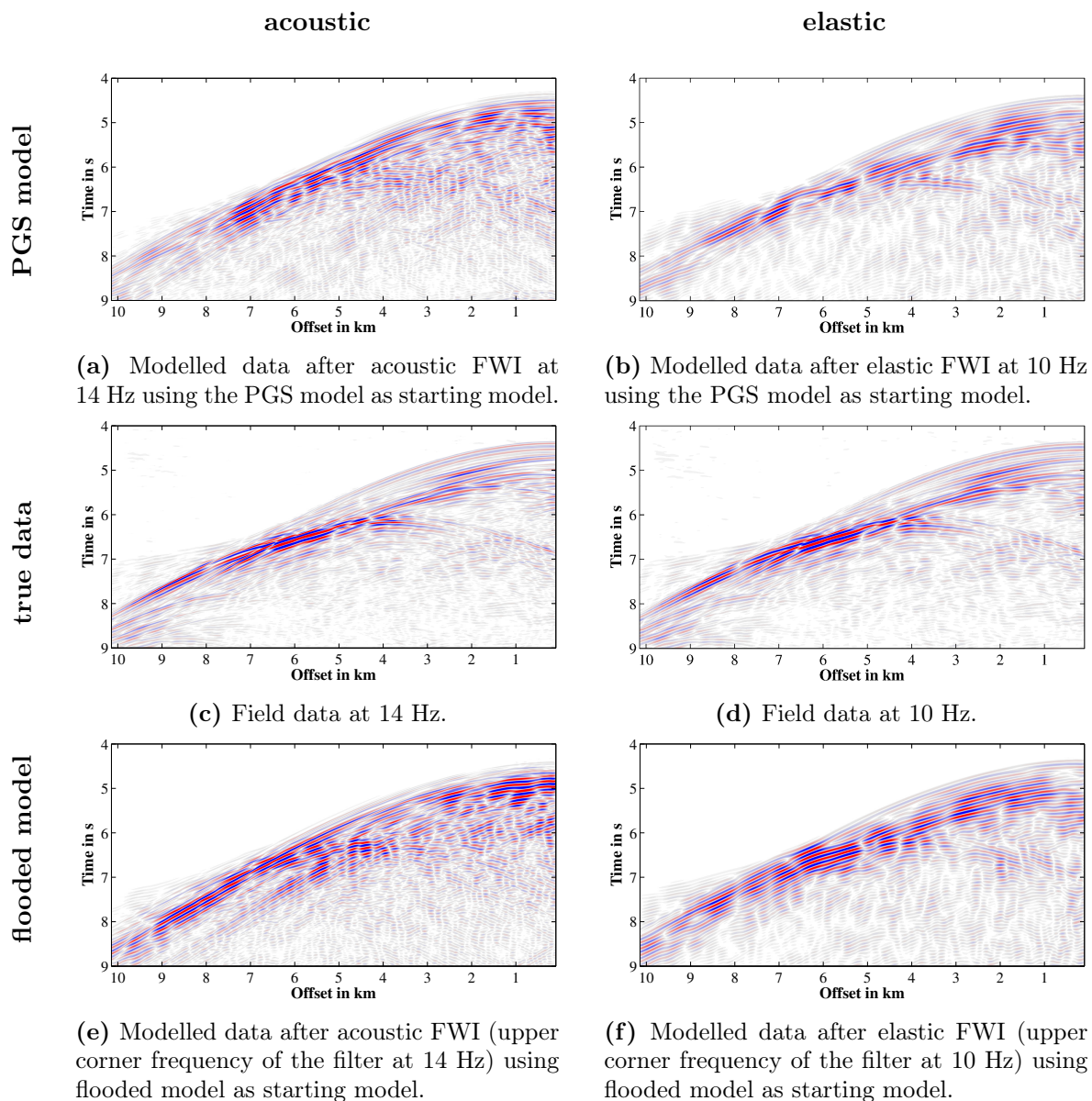# Hardware and Software

B.1 Cluster & computational cost

For most of the modellings and inversions shown in this work I used the research supercomputer ForHLR II, located at the Campus North of the KIT and operated by the Steinbuch Centre for Computing (SCC) at the KIT. The computational cost of an FWI run depends on several parameters, e.g., the grid size, the number of time samples, or the elastic or acoustic FWI. Some of these parameters are listed in table B.1.

The software was compiled using an Intel compiler. For parallelisation on the cluster, Intel MPI (Message Passing Interface) was used. The versions of the compiler and MPI changed on the cluster from time to time. The last software versions were the Intel compiler 17.0 and Intel MPI 2017.

Table B.1: Estimated computational resources for acoustic and elastic FWI on ForHLR II for two different model sizes.

parameter	acoustic		elastic	
	model 2	model 3	model 2	model 3
grid size $(x \times y)$	7080×960	1600×640	14160×1200	3200×1280
size of subdomains of spatial parallelisation	236×60	80×64	60×60	64×64
number of cores	480	300	4720	1000
time per iteration	≈ 85 min	≈ 7.5 min		≈ 22 min
core-h per iteration	≈ 628 h	≈ 37.5 h		≈ 367 h
memory per core	≈ 1.6 GB	≈ 0.7 GB	≈ 3.5 GB	≈ 3 GB
time samples				

B.2   Used software

The software used for this work is listed in table B.2. This thesis was written with LaTeX. Most of the software listed below was installed on a workstation with openSUSE 13.2.

Table B.2: Used software during this work.

software	version	application
IFOS2D	2.0.3, modified	modelling and inversion of synthetic data and field data
lisousi	V1.12d	3D-2D transformation of field data
MATLAB (MathWorks)	R2014a	picking interfaces, plotting, testing
Seismic Unix	R42	plotting, filtering, time windowing, padding
CREWES raytracer	1604	ray tracing

Danksagung

Zu guter Letzt möchte ich noch ein paar dankende Worte an alle richten, die mich während meiner Promotion begleitet und unterstützt haben:

Allen voran danke ich Prof. Dr. Thomas Bohlen für die Übernahme des Hauptreferats und die Unterstützung während der gesamten Promotion. Vielen Dank für die Betreuung, sowie die vielen Freiheiten und Möglichkeiten in dieser Zeit.

Vielen Dank an apl. Prof. Dr. Joachim Ritter für die Übernahme des Korreferats und das konstruktive Feedback zur Arbeit.

Ein besonderer Dank geht an Thomas Hertweck, der immer ein offenes Ohr für mich hatte und ein Großteil des Korrekturlesens übernommen hat, trotz des engen eigenen Zeitplans.

Insbesondere danke ich meiner Zimmer-Kollegin Laura. Vielen Dank für die vielen kleinen Diskussionen, Gespräche und die gute Atmosphäre bei uns im Büro. Ein großes Dankeschön möchte ich auch an die gesamte Arbeitsgruppe der Angewandten Seismik richten, vor allem an André während seiner Zeit hier am Institut, sowie Tilman und Martin für die gute Zusammenarbeit und die hilfreichen Korrekturvorschläge für diese Arbeit. Auch bei Ivy möchte ich mich bedanken für die kompetente geologische Beratung.

Stefan Jetschny gilt ein Dank für die schnelle Beantwortung diverser Fragen, die Unterstützung und die "schnelle Verbindung" zu PGS während der Bearbeitung des Datensatzes, trotz der großen räumlichen Entfernung nach Oslo.

Den Mitarbeitern des Instituts möchte ich ebenfalls danken, insbesondere Petra Knopf für die ganze Unterstützung im IT-Bereich und Claudia Payne, die immer meine Fragen zur Verwaltung geduldig beantwortet hat und immer ein offenes Ohr hatte.

Ein sehr großer Dank geht an Birte. Vielen Dank für deine Geduld und große Unterstützung in den letzten Jahren.

Acknowledgements

This study is based on a field data set from PGS. Thank you, Lesley, for arranging this data set. Without you, this work would not have been possible. I thank PGS for providing this data set and allowing me to use it for my PhD thesis.